RISK ASSESSMENT OF REINFORCED CONCRETE SEWER PIPES UNDER EXTERNAL LOADING AND ADVERSE ENVIRONMENTAL CONDITIONS USING AN ADAPTIVE NEURO-FUZZY SYSTEM

By

KHALED SALEH KHALED ABUHISHMEH

DISSERTATION

Submitted in partial fulfillment of the requirements for the degree of Doctor of Philosophy at

The University of Texas at Arlington

December, 2023

Arlington, Texas

Supervising Committee:

Himan Hojat Jalali, Assistant Professor. (Supervising Professor)

Mohsen Shahndashti, Associate Professor

Suyun Ham, Associate Professor

Jay Rosenberger, Professor

ACKNOWLEDGEMENT

I want to thank the people who helped me with my dissertation. First, my thanks to my supervisor, Dr. Himan Hojat Jalali, for his guidance. I also want to thank my dissertation committee for giving advice and sharing knowledge.

I would like to thank my family and friends for their support, understanding, and encouragement.

Finally, I appreciate the University of Texas at Arlington (UTA) for providing valuable resources and a suitable environment to conduct this research.

ABSTRACT

Risk Assessment of Reinforced Concrete Sewer Pipes Under External Loading and Adverse Environmental Conditions Using Neuro-Fuzzy System

Khaled Saleh Khaled Abuhishmeh, (Doctor of Philosophy in Civil Engineering)

Supervising Professor: Himan Hojat Jalali

Failure of sewer mains poses a significant threat to the society, necessitating a robust risk assessment tool that integrates failure likelihood and associated consequences for effective prioritization of mitigation efforts. This dissertation addresses this need through three key objectives:

1. Failure Likelihood Assessment: The study utilizes Monte-Carlo simulation to evaluate the probability of sewer main failures in common agressive environments, considering factors like sulfide and chloride exposures. It highlights that chloride-induced cracks and bond strength loss are more critical than sulfide-induced wall thickness loss. The degradation of concrete and reinforcement properties under chloride attack significantly reduces ductility, emphasizing the importance of factors like rust expansion coefficient, reinforcement size, and cover thickness in controlling service life.

2. Quantifying Consequences: This study establishes a quantitative framework to predict the monetary consequences of sewer main failures. It accurately predicts direct costs associated with two repair methods—Cured in Place Pipe (CIPP) as lining and open-cut replacement—using

stepwise regression models. Additionally, it addresses indirect costs, including noise cost, pavement reduction value, traffic delay, and vehicle operating cost, by employing Monte-Carlo simulation to account for uncertainties. This approach offers a precise alternative comparison method, superior to qualitative or scaled quantitative techniques.

3. Adaptive Neuro-Fuzzy Integration: To enhance the versatility of fuzzy inference systems (FIS) in risk assessment, this research integrates FIS with an adaptive neural network, resulting in an adaptive neuro-fuzzy system capable of learning FIS parameters and adapting to evolving decision-maker preferences. The model undergoes training using diverse optimization algorithms and learning rates, with the Adam optimizer demonstrating efficiency in reducing training trials.

In conclusion, this dissertation culminates in a comparative analysis of the proposed neuro-fuzzy model with conventional risk assessment approaches, such as the risk matrix and parameter multiplication. Findings reveal that the parameter multiplication method, though sensitive to input uncertainties, does not rely on decision rules, making it suitable when decision rules are absent or precise predictions are available. Conversely, the risk matrix and neuro-fuzzy approaches prioritize actions based on decision rules rather than exact likelihood and consequence values, rendering them more appropriate for informed decision-making. Notably, the adaptive neuro-fuzzy approach enhances interpretability and facilitates smoother transitions between risk classes, promoting superior decision-making and action prioritization, particularly for pipes within the same risk category.

Contents

LIST OF FIGURES

LIST OF TABLES

LIST OF ABBREVIATIONS

A_{rs} = Residual reinforcement area after corrosion (m^2);

A_r = Residual rib area in rebar (m^2);

A_0 = Intact reinforcement area (m^2);

a_1 = Depth of compression zone in flexural member (mm);

b_1 = Section width (m);

C_r = Coefficient depends on rib shape and area;

Cl_{su} = Chloride concentration at the surface (g/cm^3);

D_{cl} = chloride diffusion coefficient;

$d = h - c$ (mm);

d_c = Rust thickness (mm);

EW = equivalent weight of steel 18.62 (g);

F_c = Fact or for effect of curvature on diagonal tension strength in curved Components;

F_d = Factor for crack depth effect resulting in increase in diagonal tension strength with decreasing;

F_{rt} = Factor to consider the effect pipe size effect on the radial tension strength;

F_{vp} = Factor for process and material that affect the shear strength of pipe;

f_{coh} = Adhesion strength between concrete and reinforcement (Mpa);

f_{ct0} = Initial tensile strength of concrete (Mpa);

k_1 = Empirical coefficient ($g/\mu A$);

L_d = Development length (mm);

M_s = Service flexural Moment ($KN\ m/m$);

M_u = Ultimate flexural moment ($KN\ m/m$);

N_u = Ultimate thrust load (KN/m);

n_{bars} = Number of bars;

n_{ribs} = Number of transverse ribs;

R_e = Resistance of concrete (Ω m)

R_s = Radius of curvature of inner reinforcement bar (mm);

r_r = Residual radius of reinforcement bar due to corrosion (mm);

S_r = Ribs spacing in rebar (mm);

S_t = Concrete saturation (%);

V_u = Ultimate shear load (KN/m);

w_0 = Crack width at zero tensile strength (mm);

$^{w}/_{c}$ = Water to cement ratio;

ρ = Density of steel (g/cm^3);

α = Rust to steel volume ratio;

ε_{u0}= Initial ultimate strain of reinforcement bar;

ε_{r,r_s}= Radial strain at steel concrete interface;

$\varepsilon_{t,cr}$= Ultimate tensile strength of concrete;

θ_f= Flexural strength reduction factor;

θ_{vp}= Shear strength reduction factor;

$\emptyset$ = Angle of Friction between steel and concrete(Rad);

δ = Rebars' ribs angle of inclination (Rad);

β = Empirical factor in soft tension model.

Chapter 1. Introduction

1.1. Overview

Sewer mains are responsible for transferring sewage from homes and other resources to the points of sewer collection from homes and other resources. In the United States, there are approximately more than 800,000 miles of public sewer mains in addition to 500,000 miles of lateral private sewer connected to the mains (Infrastructure Technical Report. 2017). These pipes are commonly either ductile iron pipe, reinforced concrete pipe, plastic pipe (i.e., PVC, HDPE, PE, ABS), or vitrified clay pipes. Each of these materials behave differently and have different properties and lifespans (USEPA 2000). Reinforced concrete pipes (RCPs) are well known for their strength and durability and are considered the strongest pipe available compared to flexible pipes, which gain their strength from installation conditions (ACPA 2023).

Due to excessive loading and adverse environmental conditions, these pipes become vulnerable over their lifespans and prone to failure leading to catastrophic health and financial concerns. In Bluffton, South Carolina, a sewer main failure caused more than 45,000 of wastewater dissipation to the surrounding neighborhood resulting in road closure, service interruptions, and potential contamination of groundwater, in addition to extensive cost of pipe replacement and surface reinstatement (Cuglietta 2023). Another failure incident occurred in Los Angeles, California, where a 60-year-old sewer failed and caused the dissipation of millions of gallons of wastewater into the city and to the nearby beach halting social life and raising health concerns (Canon 2022). Nine months later, a 30-inch sewer main failed in Mesquite, Texas causing the dissipation of more than 200,000 gallons of wastewater and reaching south Mesquite Creek, which flows to the Trinity River (City of Mesquite 2022). Generally, the mean age of water and

wastewater pipelines in the United States is 45 years with an expected lifespan of up to 100 years (Tabuchi 2017). According to the Infrastructure Technical Report (2019), the American Society of Civil Engineers (ASCE) gives D+ as an overall grade for the entire wastewater/water infrastructure. More than $3 billion has been spent on the replacement of 4,692 miles of wastewater sewer mains and $48 billion has been allocated for water infrastructure, yet this only met 37% of the national needs.

The reliability of these pipes is monitored through routine inspections conducted in intervals; pitfalls and defects are reported and based on conditions rating, counteracting actions are taken. The extent of these actions depends on the level of deterioration compared to the pipes' inventory condition. These proactive actions include routine cleaning, point repairs over a small section of pipes, pipe rehabilitation, and complete replacement. Different resources related to inspection practices are available. ASTM C1840/C1840M (2022) provides a standard practice for the inspection of sewer main and requirements for both person entry and remote inspection mainly for gravity, non-pressure drainage systems. AASHTO CSDIM (2020) provides inspection and rating guidelines for storm drains and culverts that do not follow the NBI bridge classification.

The scope of this study focuses only on reinforced concrete pipes (RCPs); therefore, the upcoming sections discuss the environmental conditions that affect these pipes, in addition to the design standards and practices.

1.2. Adverse Environmental Conditions

As RCPs are in service, they are subjected to different adverse environmental conditions that impact their serviceability and structural integrity (Amin Soltanianfard et al. 2023). The most common aggressive environmental conditions are sulfide attack, which is responsible for wall

erosion, especially at the unsubmerged region such as the crown of the pipe, and chloride corrosion, which aggressively deteriorates the reinforcement and degrades the structural capacity. These conditions depend on parent factors to reflect their intensity as shown in **Fig. 1**.

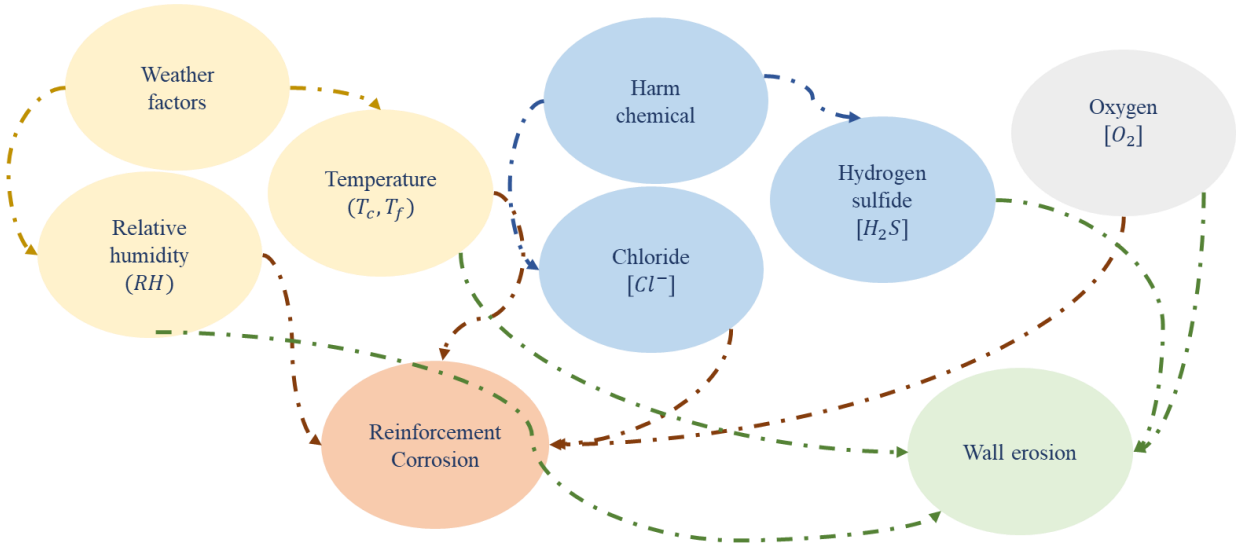

Fig. 1. Factors associated with wall erosion and reinforcement corrosion observed in RCPs

1.2.1. Sulfide-Induced Erosion

The wall erosion process is the degradation or loss of thickness of concrete along the perimeter that is exposed to an aerobic environment and sulfide. Based on Pomeroy & Richard (1974), there are multiple sources for sulfide accumulation; however, the most common source is the inorganic sulfate. The process of sulfide-induced erosion can be summarized into four different stages as presented in **Fig. 2** (Abuhishmeh & Hojat Jalali 2023). The first stage takes place beneath the water level and demands an anaerobic environment to sustain. Inorganic sulfate (SO_4^{-2}) exist along a slim layer on the perimeter of the pipe. Depending on the level of oxygen and with aid from an aerobic microorganism (i.e., sulfate-reducing bacteria), the inorganic sulfate reduces to sulfide in the form of Hydrogen sulfide (H_2S), which is accompanied by a reduction in the

alkalinity of concrete (i.e., pH drops to 9). If a high level of oxygen exists (i.e., greater than 0.1 mg/L), it will oxidize all generated sulfide from the first reduction; otherwise, the oxygen will be consumed by the microorganism. Also, the rate of sulfide development depends on the stream velocity as high turbulence flow will increase the aeration in the flowing stream and reduce the thickness of the slim layer, which hinders the production of sulfide. Further details are provided by Parker (1951), Promery & Richard (1974), and Abuhishmeh (2019).

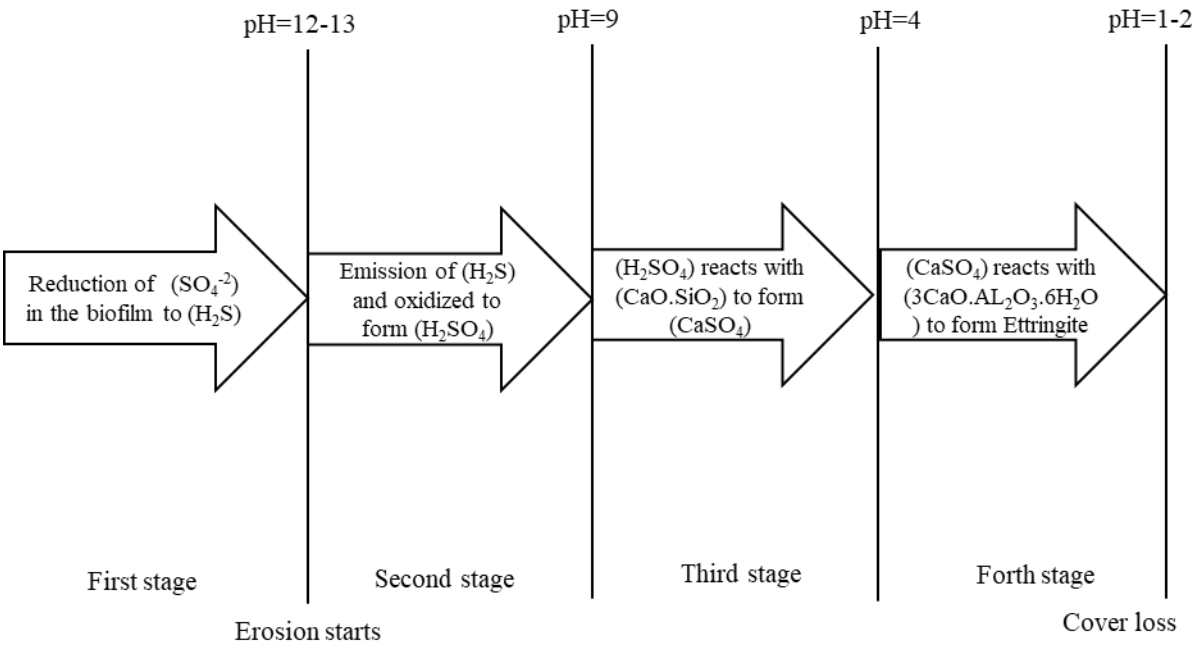

Fig. 2. Four-stage processes for sulfide-induced erosion development (Abuhishmeh & Hojat Jalali 2023).

In the second stage, the hydrogen sulfide escapes to the atmosphere and gets oxidized. Lowering the pH value allows for colonization of other microorganisms such as *thiobacillus* along the perimeter of the pipe above the waterline, which is responsible for oxidation. As the pH keeps dropping, new microorganisms replace the old ones and take responsibility for oxidation. The erosion process starts at the end of the third stage at which the pH level drops significantly to

around four and the hydrogen sulfate reacts with concrete's carbonate and silicate products to form gypsum. The gypsum is visible during inspections, and it weakly adheres to the surface. In the last stage, the gypsum reacts with tricalcium aluminate to form ettringite, which has an expansive nature and induces cracking to the surface.

1.2.2. Chloride-Induced Corrosion

Reinforcement corrosion is an electrochemical reaction, in which both the anode and cathode region must exist along with an electrolyte medium to transfer electrons from the anode to the cathode. Several studies such as Ahmad (2003), Marques et al. (2012), and Song et al. (2019) have investigated the mechanism of corrosion. The corrosion process does not start immediately after exposure to harmful chemicals, moisture, and oxygen; however, it starts when the reinforcements lose their depassivation layer due to oxidation (Ahmed 2003), or when aggressive chemical reaches a threshold value (Sulikowski & Kozubal 2016). The entire reactions that occur in the anodic and cathodic regions are depicted in **Fig. 3**.

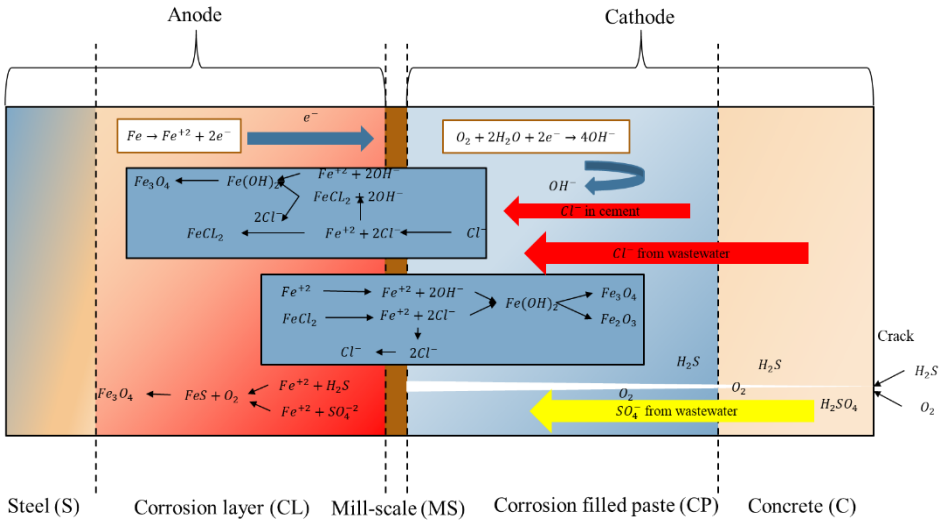

Fig. 3. Electrochemical reactions in the anode and cathode region in reinforced concrete structures (Song et al. 2019).

According to **Fig. 3**, the thickness of the cover can be defined into five different regions. The first two regions: steel (**S**) and corrosion layer (**CL**) are the anodic region where oxidation of iron (Fe) occurs and cause electrons to transfer to the cathodic region (corrosion-filled paste (**CL**) and mill scale (**MS**)) through the electrolyte medium (water filling concrete pores or cracks). In the cathodic regions, reduction of oxygen occurs produces hydroxide (OH^-), which moves back along with active anions such as chloride (Cl^-) to the anodic region through the mill scale and the corrosion layer. Once these anions reach the steel-concrete interface, they react with iron cations (Fe^{+2}) to produce ferrous chloride and ferrous hydroxide. The remaining iron cations will move to the cathodic region and produce consistent reactions, but in lower concentrations, since chloride and hydroxide ions have more potential to move toward the anodic region.

The composition of generated rust depends on the availability of oxygen (Song et al. 2019). At the steel-concrete interface, the rust is composed of Fe_3O_4, Fe, $FeCl_2$, α-$FeOOH$ and γ-$FeOOH$, while at the external layer, it is composed of γ-Fe_2O_3 due to the high presence of oxygen. Zhao et al. (2011a) investigated rust composition in different environmental conditions, and they found that the outcomes of the corrosion process are extremely dependent on environmental factors such as temperature, humidity, oxygen levels, and water-to-cement ratio. Under excessively high temperatures, α-$FeOOH$ and γ-$FeOOH$ are destroyed, while Fe_3O_4 is gradually transferred to γ-Fe_2O_3. Humidity provides a perfect electrolyte for transferring electrons and facilitates the growth of α-$FeOOH$ and γ-$FeOOH$. A high water-to-cement ratio means high permeability, which facilitates the migration of chloride and oxygen to the steel. Moreover, each of these outcomes has different expansion factors, which reflect different impact levels.

1.3. Research Goals and Objectives

Because sewer mains are continuously subjected to adverse environmental conditions that impact their service life and can potentially induce failure, there is a need to develop a time-dependent prediction model that can be used to monitor the reduction in pipes' capacity over time. Also, with most pipes across the country approaching the end of their lifespan, there is a need for risk assessment to proctor decisions related to counteracting actions on these structures. Therefore, the aim of this study is to:

- Develop a framework for failure and serviceability loss predictions of reinforced concrete pipes considering all possible failure modes and their interactions.
- Develop models to predict the anticipated costs or consequences of failure and counteracting actions.
- Finally, develop and enhance the state of risk assessment practice toward more effective decision-making.

In Chapter 2, prior studies related to failure and serviceability predictions, estimation of consequences resulting from failure, and various approaches to risk assessment are examined to identify gaps and potential areas for improvement. Chapter 3 will present the adopted methodologies and frameworks for stochastic reliability analysis, with consequences being interpreted as direct and indirect costs. Additionally, the implementation of previous risk assessment approaches will be discussed, and a novel risk assessment model will be developed. To illustrate the integration of reliability analysis and the prediction of consequences in risk assessment, a case study will be presented in Chapter 4. Furthermore, this chapter will demonstrate the adaptability of the proposed risk assessment model to different scenarios potentially imposed

by decision-makers and will showcase the advantages of employing various optimization algorithms in the training process of the proposed model. In Chapter 5, a detailed discussion of the outcomes of reliability analysis and the consequences of failure, along with a comparison between traditional risk assessment approaches and the proposed model, will be provided. The last chapter will summarize the research outcomes and provide recommendations.

The significance of this work lies first in considering different serviceability aspects of failure and serviceability loss that are anticipated to occur in RCSPs under the effect of the adverse environmental conditions. As shown in the upcoming section the effect of the chloride-induced corrosion and sulfide-induced erosion will be reflected on the geometrical and the mechanical properties of both reinforcement steel and concrete leading failure modes that are unaccounted for previously such as bond strength loss, cracking, and reinforcement ductility loss. Another significance of this research is addressing the uncertainties in the consequences of failure from both regression model and Monte-Carlo stochastic analysis and present it monetary rather than qualitative or scaled representation, which is more appealing and less subjective when it comes to decision-making. Finally, the novelty of the proposed risk assessment model encounters the drawbacks of other qualitative and quantitative models and shows an ability in adopting different decision-makers' opinions.

Chapter 2. Literature Review

2.1. Overview

In this chapter, the focus will be on the detailed revision of previous studies and research on topics that are relevant to the aims of this research. This chapter will be divided into three sections. The first section is about relevant studies related to failure and serviceability loss predictions using analytical and statistical models; the second section is about adopted methods for evaluating the consequences and risk of failure and serviceability loss in previous studies. In the last section, the author defines the gap found in previous studies and potential improvements.

2.2. Failure and Serviceability Loss Predictions

Condition evaluation and failure predictions can be performed using different approaches (Abuhishmeh & Hojat Jalali 2023). The base of these approaches can be either probabilistic or deterministic. In the first case, the analysis models the response to action as a probability density function and accounts for uncertainties in the actions, material properties, and surrounding environment parameters. In the latter approach, all variables are treated as deterministic disregarding uncertainties.

Davis & Marlow (2008) used a probabilistic-based physical analytical model to predict the failure of cast iron water pipes under the effect of external corrosion from the surrounding soil. They used inspection data related to corrosion penetration and remaining wall thickness in addition to the original wall thickness to model the variation in the corrosion rate. They assumed that it follows Weibull distribution. The authors adopted a physical model to evaluate the reliability and estimate the lifetime of this type of pipe. This model is developed based on the Schlick failure criterion considering applied external loads, internal pressure, and pipe geometrical properties in

addition to corrosion rate and its impact on wall thickness. All variables were deterministic except the corrosion rate. The estimated probability density function was obtained using Monte-Carlo simulation and it follows a Weibull distribution, as well. Schoefs et al. (2009) used a probabilistic-based statistical model to evaluate the reliability of reinforced concrete pipes (RCSPs) under the effect of chloride-induced corrosion. The authors defined corrosion initiation time as the time when chloride concentration reaches a threshold value and used an empirical model developed by Peter-Lazar et al. (2000); they also assumed that the corrosion rate is deterministic $55\ \mu m/year$ based on previous feedback. The reliability of the RCSPs was evaluated based on only one limit state function, which is considered structural failure when the steel is completely gone.

Mohamoodian & Alani (2014) used a probabilistic-based statistical model to evaluate the reliability of RCSPs under the effect of sulfide-induced erosion. They assumed that the remaining wall thickness under erosion follows a time-dependent gamma distribution and failure occurs when the cover completely vanishes. Distribution parameters were obtained using both maximum likelihood and moment methods. This model was efficiently used to obtain the optimal intervention time. Alani & Farazani (2015) used probabilistic-based finite element modeling to study the impact of self-induced erosion on the reliability of RCP under traffic loading. The authors choose to rely on 2-dimensional finite element modeling to obtain the residual flexural strength of RCSP rather than using analytical approaches, which included simplified assumptions. Additionally, the authors used a predefined statistical model developed by Pomeroy (1976) to evaluate sulfide-induced erosion penetration and to find the residual thickness. Finally, the authors conducted a sensitivity analysis to investigate the effect of different design parameters on residual reliability.

Anbari et al. (2017) developed a Bayesian network for evaluating the likelihood of failure at both structural and hydraulic levels. At the structural level, they considered different erosion and

corrosion, in addition to cracking and deformation, while at the hydraulic level, they considered blockage and leakage. The process of building the Bayesian network starts by defining the root nodes of each failure node, which includes inventorial properties, age, and traffic loading. The next step is to add the child nodes which include the failure nodes and add higher-level nodes that reflect the combined structural and hydraulic failures. The next step is to build probability tables for each node to use for the inference expectation maximization algorithm. Parent nodes have marginal probability tables as they are independent, while child nodes require conditional probability tables.

Like Mohamoodian & Alani (2014), Phan et al. (2018) fitted a probability density function for predicting the failure of flexible non-pressure metal pipes over time; however, the authors select Weibull distribution instead of gamma distribution. The Weibull distribution has scale and location parameters. The latter one is available to update based on expert opinion or datasets. After defining dependent random variables related to flexural failure and resistance of pipe, Monte-Carlo simulation was applied to samples from the distributions of these variables. Moreover, they analytically evaluated the reliability of these pipes over time to build the cumulative density function of failure over time. The author used least square regression to fit the results of the Monte-Carlo simulation to the Weibull distribution and obtain the scale and location parameters. This model can be updated interactively after inspection, at which experts can provide a certain probability of failure. This probability along with the time of inspection relative to the age of the pipe component can be used to adjust the location parameter. Finally, the authors used fault tree analysis to estimate the probability of failure at the system level.

Robles-Velasco et al (2021) developed a machine-learning logistic regression model for predicting the probability of failure of the water main or sewer main network. Two main failure types were considered: blockage and breakage. The authors relied on a five-year case study

inspection dataset containing inventorial data in addition to the number of reported failures and sulfide attacks for concrete pipes. The model was trained using the genetic algorithm to maximize the likelihood function.

Another application of the gamma process for failure predictions was conducted by Tang et al. (2022). The authors used culvert inspection data and measured sulfide-induced corrosion levels to calibrate the shape and scale parameters of the model using maximum likelihood optimization. Also, they assumed that the corrosion rate follows the exponential relationship explained by Pomeroy (1976) and is reflected in the scale parameter. The impact of exposing reinforcement was considered, as well; the authors assumed that reinforcement corrosion starts once it is exposed (i.e., complete loss of cover) and reinforcement vanishes when the erosion depth exceeds the cover depth and its diameter. The authors used this assumption to analytically evaluate the flexural reliability of culverts.

The utilization of long- and short-term inspection data for building a time-dependent probabilistic model was carried out by Tran et al. (2022). They developed a Markov chain model to predict the transitional probability from one condition rating to another over time for RCPs and concrete box culverts. The model was trained on two types of data. The first dataset is long-term training data and reflects old structures that have missing inspection records and only have one recent in addition to inventory inspection at the time of installation. The second data type is the opposite of the first one; these are collected to reflect newer structures with more frequent inspections. Further sub-datasets were also collected for each data type (i.e., long, and short term); these sub-datasets include other influential factors such as the size, length, demographics location, and Annual Daily Traffic (ADT). The purpose of generating all these sub-datasets was to investigate the sensitivity of each factor on the transitional probability from one condition to

another at a specific time. The major assumption in this model was that the conditions are not reversible. In other words, preventive action impact was disregarded. Based on training results, short-term data type proved to be more reliable, and pipe diameter and demographic location variables had a major influence on the transition.

A series of automated data-driven algorithms have been developed for the condition assessment of RCSPs. Ebrahimi & Hojat Jalali (2021) aimed at residual life and reliability assessment under uncertainty. This work explored finding the best-fit distribution of concrete erosion data through LiDAR inspection. Ebrahimi & Hojat Jalali (2022a) introduced algorithms that calculated the actual diameter and ovality of these sewer pipes employing LiDAR data. Ebrahimi & Hojat Jalali (2022b) addressed the spatial variability effects of wall erosion across the pipe circumference. Finally, Ebrahimi et al (2023) utilized LiDAR inspection data erosion data to develop a probabilistic framework for service life predictions.

2.3. Consequences and Risk Evaluation Approaches

Failure of sewer mains can have slight, moderate, or catastrophic consequences depending on failure modes, the importance of the structure in serving the society in addition to the impact on the surrounding environment and any adjacent structures. Predicting failure, whether probabilistically or deterministically by itself may not be a sufficient benchmark to validate preventive actions, since structures with equivalent conditions can have different failure consequences; therefore, decisions should not be only made based on failure prediction outcomes. Decision-makers prefer to validate their decisions using the risk variable, which is the potential loss induced by failure potential and expected consequences (PHMSA 2020).

There are different approaches to evaluate failure consequences and risk; these approaches can give either qualitative, or quantitative measures, ordinal indices, or probabilistic measures (AWWA J100 2010; PHMSA 2020). In general, there is no specific scheme for risk assessment; hence, the choice of risk assessment method is lifted to be subjective and heuristic (Halfawy et al. 2008). Halfawy et al. (2008) developed an innovative model for selecting suitable year-by-year renewal plans on sewer mains based on risk index. Risk indices for groups of sewer mains share the same conditions and consequences. Risk results were used to prioritize groups of sewers for renewal actions in the yearly renewal plan. A set of renewal plans was suggested at the beginning, and then multi-objective genetic algorithm optimization was conducted to select the most appropriate renewal plan considering budget constraints and risk levels. Zeng & Ma (2009) used a risk matrix for prioritizing preventive actions on pipeline systems. They first constructed different ordinal scales for multiple consequences categories including cost, effect on the entire pipeline system, service interruption, and safety level. The overall effect of all categories was evaluated using the max-average approach to avoid the domination effect of a single high-level category on the prioritization process. Li and Zou (2011) developed a fuzzy-based risk assessment model for mitigating the risk associated with planning, procurement, financing, design, construction, and operations related to private-public partnership projects. The power of fuzzy principles lies in their ability to mitigate the vagueness and uncertainty in human judgments. When such a project is under investigation, there are different threats to consider, and one way to prioritize each threat is to use an analytical hierarchical process (AHP). Li and Zou (2011) constructed two-level AHP models, in which twenty-three different threats or risk factors were identified and grouped into different tasks in the project. The AHP model evaluated the weights for each threat to allow same-level comparison and the weights on higher levels for group

comparison and obtaining the marginal contribution of each group to the marginal risk (i.e., risk factor considering all groups). The process of developing the AHP model is to develop weighting factors based on experts' judgments as further discussed by Ishizaka & Labib (2009). Li and Zou (2011) included the fuzzy principles in these weights and added other variables to mimic the subjectivity in experts' judgments. Another integration of fuzzy principles in the AHP system for risk assessment was done by Tran et al. (2012). This was a three-level AHP model with a fuzzy system that was used to interpret uncertainties related to risk factors. On the bottom level different risk factors related to likelihood and consequences of manhole failure were assigned, while on the upper level, different aspects of failure modes and consequences were added to head risk factors. At this level, each aspect was expected to have a different impact on the likelihood or consequences, and hence on the risk level. Compared to Li and Zou (2011), Tran et al. (2012) considered the fuzziness in the risk factor values rather than in the weights. The outcome of this model was a risk index described as a real number in the universe of associated fuzzy sets, which was later converted to a single value using the center average defuzzification method.

Elsawah et al. (2014) presented a framework for estimating the integrated risk index for three types of integrated infrastructures in a corridor segment within a network, which included sewers, water pipes, and roads. First, on the individual level, the criticality of each structure in addition to related consequences was estimated. The integrated criticality of a corridor segment was estimated additively from the criticality on the individual level, while the consequences were estimated for the entire corridor using the adopted AHP method. The risk index was determined using a predefined risk matrix, which is a set of rules that designate different risk indices based on different combinations of criticality and consequences index. Another risk index evaluation approach for integrated sewer, road, and water pipes was done by Shahata & Zayed (2016). The

authors used the Delphi-AHP model for estimating the consequences of failure for each infrastructure considering economic, social, operational, and environmental factors. Integrating the Delphi approach in the development of the AHP model allowed interactions among experts and contributions to each other's understanding, which lead to a dynamic revision of weights and criteria of factors based on experts' feedback. The integrated likelihood and consequences were estimated using the K-mean clustering algorithm; each of the likelihood and consequences on the infrastructure level was divided into five different groups graded from one to five using the clustering algorithm. The combination of groups of consequences and likelihood on the integrated level would give the risk index, which was obtained using a predefined risk matrix. Inanloo et al. (2016) evaluated the risk on transportation networks due to pipeline network failure. They started by assigning a vulnerability level to each road in the transportation network based on the type of road (i.e., highway, collector, or other) and setting possible scenarios of the interaction impacts caused by an observed failure in either pipeline or transportation network. In the next step, they evaluated the likelihood of failure of each pipe within a network based on failure occurrence given specific material type, age, and diameter. In the third step, a rank map for each network and the overall network was developed using ARGIS and it was used to assess the overall vulnerability of the integrated road and pipeline networks. Using the obtained vulnerability, the affected population and area in addition to traffic flow (i.e., traffic delay) were estimated and mapped on GIS.

Altarabsheh et al. (2017) developed a multi-objective approach for selecting rehabilitation alternatives that impact the behavior throughout the entire life cycle. These objectives include maximizing the condition index and network serviceability and minimizing the risk of failure and life cycle cost. The authors first defined models related to the evaluation of each objective. For the condition index, the author assumed a semi-Markov model that gives the transition probability

matrix from one state or index to another; this probability was based on the time that the sewer will maintain a specific state and follows the Weibull distribution. For the risk model, the author used the simple multiplication of the likelihood and consequences, which was estimated using the weighted average or AHP method. For life cycle cost, they considered both the cost of replacement and rehabilitation. Finally, they defined serviceability as the number of blockages estimated from the Markov chain stochastic process. Because of the large number of possible alternatives and discontinuity of the objective functions, optimization of the objective functions was done using genetic algorithms. After each evaluation period, one solution was selected out of a set of solutions based on a function to ensure a tradeoff between objective functions. Tabesh et al. (2018) developed a risk assessment framework related to non-revenue water loss caused by apparent losses, real losses, and non-revenue authorized losses. The first step was to build a Bayesian network model to assess the likelihood of non-revenue water loss caused by each of the three main components. The next step is to evaluate both economic and social consequences associated with each NRW component. Finally, the author defined fuzzy sets for likelihood, financial, and social consequences and used them to infer risk using the FIS system. Similar to the previous application, the center area method is used for defuzzification. Zhou et al. (2020) developed a Bayesian-based risk assessment model for sewer mains located in utility tunnels, in which sewer mains are placed adjacent to other structures such as water mains, gas pipes, and electric and heating systems. Similar to other Bayesian network models, the authors started with the structural learning phase to define the parent nodes and child node configuration. Next, the conditional probability table for each node is inherited from previous related incidents and experts' opinions. The expected outcome of this model is a probability of occurrence of economic loss, casualty, and pollution (i.e., consequences) being slight, moderate, or high, which implicitly reflects risk. Finally. The authors

tested the proposed model on multiple scenarios constructed by varying the states in the parent nodes (i.e., potential threats) and investigated the impact of threats using sensitivity analysis. Benbachir et al. (2022) developed a fuzzy-based failure mode effect and criticality analysis model for decision-making prioritization of urban sewage systems (FMECA). In the conventional FMECA model, the first step is to assess the score of failure observed in the structure, which is based on a set of criteria designated for three parameters: risk, severity, and detectability. The last two parameters represent the consequences and how fast a failure mode is detected. Using inspection data and previous reports, experts' judgments can be turned into individual scores for each criterion. The next step is to combine the scores of criteria in each parameter and present one entity that describes the criticality of the structure. Benbachir et al. (2022) assume that the criticality index is defined as the product of the indices on parameters (i.e., risk severity, detectability. The estimated criticality index reflects the structural condition of the structure. The domain of this index is divided into four main groups and mapped to a performance measure, which is used in decision-making. The integration of the FIS comes after the first step; risk, severity, and detectability indices are considered the antecedent part of the FIS rule base, while the performance parameter (i.e., desired outcome) is considered the consequent part. A set of rules are assigned by experts and fuzzy sets are defined for each parameter in the antecedent and consequent part. Finally, typical operations of the FIS system are performed to obtain the performance measure.

Zhang et al. (2022) extended the application of the AHP model in risk assessment of water networks and pipeline systems in general to a new method called analytic network process (ANP). As discussed in previous studies, the AHP method is built based on different factors (i.e., risk factors) that contribute to the decision-making process, with impacts inherited from experts'

opinions. However, the estimated impacts can only give information about the sensitivity of each factor relative to others located at the same level. The ANP method allows comparison among factors at all levels. The method starts by dividing the factors into primary and secondary factors as in the AHP method, then weights are calculated at both levels considering coupling or interaction effects. More details about this method are provided by Zhang et al. (2022). The outcome is a vector that represents the coupling proportions of factors on the risk. In the next stage of this study, the authors include fuzzy principles in the model, in which each factor was presented as a membership function. Using fuzzy principles have allowed explaining the outcomes of the model in terms of probability; for example, the probability of a pipeline to be in a safe state based on a specific factor or based on all factors.

2.4. Gaps and Research Contributions

After a comprehensive evaluation of related studies, it is observed that the common approaches in defining the deterioration of a pipeline system are either deterministic or probabilistic, which are applied to either analytical physical-based simple models, complicated numerical models, or statistical models such as Davis & Marlow (2008), Alani & Farazani (2015), and Phan et al. (2018), respectively. Despite the variety of models and approaches adopted, there is a lack of evaluation based on multiple failure modes. For example, Mahmoodian and Alani (2014) considered only wall thickness loss when evaluating the reliability of RCSPs. Similarly, Alani & Farazani (2015) and Tang et al. (2022) considered wall thickness loss in addition to flexural strength. Moreover, most of these studies showed significant limitations in the integration of environmental conditions. Numerous studies have predominantly focused on sulfide erosion as the primary environmental factor, which leads to a reduction in wall thickness and potential

exposure of reinforcement while overlooking other detrimental factors. These factors, including chloride corrosion, can significantly affect the mechanical properties of both concrete and reinforcements, potentially impacting the structural integrity of RCSPs. Considerations of chloride-induced corrosion impacts on the reliability of RCSPs are very limited, for example, Schoefs & Aduriz (2009) & Phan et al (2018) and many more studies considered uniform chloride-induced corrosion acting on the rebar with limited assumptions; however, chloride corrosion is much more detrimental rather than being uniform and impact the area of the rebar. As explained later, it is found that chloride-induced corrosion, with its nonuniform pitting nature, leads to variations in the mechanical properties of the rebar along its length. Consequently, this corrosion is responsible for generating different failure modes, including ductility failure and a reduction in yield strength. The first goal of this research is to build a comprehensive probabilistic framework for evaluating the reliability of RCSPs by considering multiple failure modes at both service and ultimate levels, as well as to integrate chloride-induced corrosion in its pitting nature and its impact on the mechanical properties of concrete and steel such as compressive strength, yield strength, and the ultimate strain, in addition to sulfide-induced erosion.

It is also observed in the research field of consequences of failure evaluation that the majority of studies use qualitative methods for evaluating the consequences such as the AHP method, since it is hard to quantify monetarily or quantitatively due to high level of uncertainty and hard measurements; therefore, the second goal of this research is to develop a probabilistic-based models for direct and indirect consequences with monetary interpretations considering all possible aspects of uncertainty. The suggested model will be developed for two reversed actions on RCSPs experiencing serviceability loss or complete failure using data collected from

construction bidding tabs of related actions. The outcome of this stage of the study will be combined with the prior stage for risk assessment at service and ultimate levels.

Both failure mode likelihood and its corresponding consequences are combined to give the potential loss known as risk. It has been observed that there are different approaches to risk assessment. For example, some studies choose to use the simplest risk definition, which is the multiplication of both likelihood and consequences, while, others choose to use a risk matrix, which gives a qualitative or an ordinal risk scale based on a set of rules set up by experts. Also, probabilistic risk assessment has been considered through the application of the Bayesian network, which is trained based on experts' beliefs. Finally, the FIS proved to be a very efficient tool in the practice of risk assessment and decision-making since it mimics human thinking and addresses uncertainties in decision rules and variables through the fuzzification and implication process. Despite the popularity of the FIS method, it has some drawbacks. The main parameters of the FIS method are usually defined heuristically by experts, which makes the risk model inefficient in applications by other organizations in which experts might have different opinions since different opinions imply different parameters. The third goal of this research is to construct a flexible FIS system by integrating it with a deep learning neural network model that can learn the new parameters based on new adjusted rules. Also, the author aims to modify the state of practice of this model by modifying the objective function used to optimize the model to satisfy the fuzzy logic principle, in addition to testing different optimization algorithms for faster convergence.

Chapter 3. Methodology

3.1. Overview

To address the goals mentioned in **Section 2.4,** the following chapter is divided into three main sections. Each section is oriented to one of the goals. In the first section, a detailed discussion will be provided about the probabilistic framework for addressing the likelihood of failure or loss of serviceability. Whether at the ultimate or service level, illustrations about the adopted limit state functions and main assumptions will be provided in subsections. The second section is divided into two main parts. The first part is concerned with developing a direct cost model related to two counteracting actions: pipe replacement and cured-in-place pipe (CIPP). The second part is concerned with the evaluation of a set of social or indirect cost categories that are imposed on the neighborhood and road users when either of the counteracting actions takes place. The third section will go over a brief discussion about risk assessment methodologies and present a novel method for risk assessment. Finally, the integration of all three sections will be demonstrated to have different types of risk estimation.

3.2. Likelihood of Failure and Loss of Serviceability

To assess the reliability and likelihood of failure, it is essential to define the threats that cause the failure, define, or adopt all potential failure modes induced by these threats, and finally, define suitable limit state functions, which combine the actions of threats with the strength of the structure. A typical limit state function should be like the one shown in Eq. 1, where $\boldsymbol{X}$ is a set of independent factors related to loads, threats, and structural properties.

$$LS(X_1, \dots\dots, X_n) = Action(X_1, \dots\dots, X_n) - Resistance\ (X_1, \dots\dots, X_n) \quad (1)$$

In RCSPs, the applied loads include traffic load, the weight of soil fill, and the weight of carried wastewater. Typically, these pipes are designed to sustain these loading based on either ASTM C76 (2022), or the direct design method provided in the ASCE 15 (1998). Because the first method is based on a 3-edge bearing loading test and does not provide a clear formulation of the resistance of RCSPs under sustained loading, the second approach will be adopted in this study. In addition, to sustain loading, sulfide-induced wall erosion and chloride-induced reinforcement corrosion affect the reliability of RCSPs continuously over their service life. Therefore, their effects will be inherited in the formulation of limit state functions. **Fig. 4** gives a summary of independent factors and limit state functions at both service and ultimate levels.

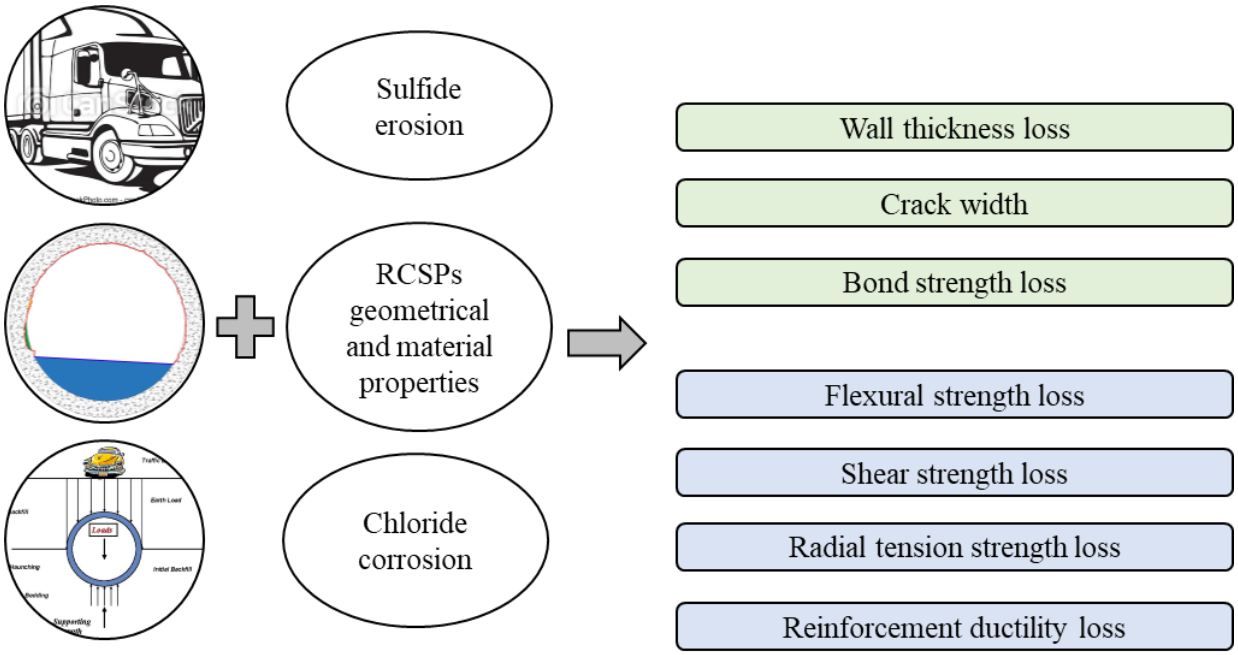

Fig. 4. Independent factors and limit state functions at ultimate and service level.

The limit state functions in green and blue boxes are designated for serviceability and ultimate levels, respectively. Detailed discussion will be provided individually in the subsequent subsections.

3.2.1. Serviceability limit states Functions

3.2.1.1. Wall Thickness Loss

In this study, wall thickness loss is considered as a serviceability issue. As explained in **Section 1.2.1** and **Fig. 2,** the presence of sulfide in wastewater is the main threat behind the erosion of wall material along the perimeter of the RCSP. As the erosion continues from its initiation point, wall material degrades and starts to reduce, which eventually leads to reinforcement exposure. Therefore, a suitable limit state function to measure the reliability is provided in Eq. 2. This function implicitly defines serviceability loss when the remaining wall thickness $h_r(t)$ reaches the wall thickness in inventory condition h less than the cover C, which is the wall thickness to the reinforcement surface.

$$WTLLS(t) = h_r(t) - (h - c) \tag{2}$$

Different approaches can be used to assess the amount of wall erosion at a specific time. Li et al (2019) conducted a regression analysis on a set of experimental data related to sulfide erosion on concrete. They successfully developed models for estimating the initiation time of sulfide erosion, $t_{in_{H_2S}}$, and the amount of erosion, Er, and are shown in Eqs. 3 & 4, where RH %, H_2S, and T_c are the relative humidity (%), sulfide concentration (PPM), and temperature (Celsius), respectively.

$$t_{in\ _{H_2S}} = 147.7 - 0.160\ H_2S - 1.01\ RH - 1.08\ T_c \tag{3}$$

$$Er = -1.96 + 0.0119\,H_2S + 0.0293\,RH + 0.0016\,T_c \quad (4)$$

Another approach was developed by Abuhishmeh (2019), in which laser inspection datasets for sewer main were processed and fitted into Weibull distribution. This distribution considers the variability of sulfide erosion level along the perimeter of the pipe. In this study, the second approach will be adopted since it considers the variability in erosion level. Simultaneously, Eq. 3 from the first approach will used to assess the initiation time. A summary of the adopted approach is provided in **Fig. 5.**

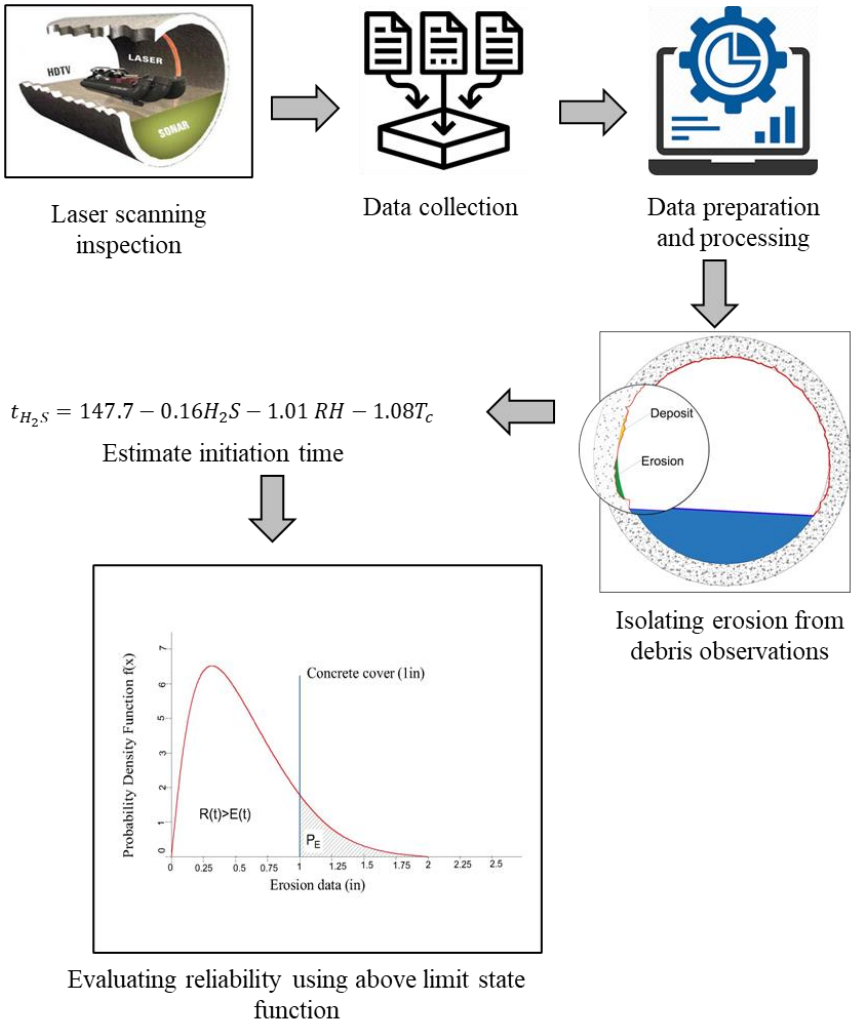

Fig. 5. Framework to assess the reliability of RCSPs against wall erosion.

3.2.1.2. Crack Width

RCSPs are continuously subjected to chloride coming from wastewater in addition to moisture and air. Therefore, based on the review in **Section 1.2.2,** RCSP reinforcements are subjected to corrosion. Naturally, corrosion product has higher volume per unit weight compared to steel; therefore, when corrosion products develop, they will induce hoop and radial stress along the perimeter of the rebar, which causes concrete cracking starting at the interface when the hoop stresses exceed the tensile strength of the concrete and propagates through the entire cover. This process is accompanied by a reduction in radial compression stresses responsible for restraining the expansion of the concrete due to cracking. As discussed in **Section 1.2.2,** reinforcement corrosion does not start immediately, and initiation time must be considered for accurate investigation. Therefore, in this study, the empirical model, shown in Eq. 5, and (Tuutti 1982) will be used, which defines initiation time as the time when chloride level at the steel-concrete interface reaching a predefined value. Cl_{su} is the chloride concentration at the surface (g/cm^3); D_{cl} is the chloride diffusion coefficient, and Cl_{th} is the threshold value (g/cm^3).

$$CLS(t) = Cl_{su}\left[1 - erf\left(\frac{\mathrm{C}}{2\sqrt{D_{cl}t}}\right)\right] - Cl_{th} \quad (5)$$

The amount of chloride, air, and moisture varies significantly during cracking stages, which indicates that the corrosion rate varies as well and as a result, the level of corrosion. Yuan et al. (2010), Jiang & Yuan (2012), Jiang & Yuan (2013), Xi & Yuan (2017) investigated the variability of corrosion rate i_{corr} expressed in $\mu A/cm^2$ and the outcome of their investigation is summarized in **Fig. 6.** As shown in **Fig. 6,** there are 5 main stages; the first stage is the initiation period at which no corrosion level occurs. In the second stage, no cracks occur although rust is developed since it fills the capillary pore at the steel-concrete interface. The i_{corr} reduces until reaches a

steady state (at time t_1) due to the accumulation of rust that prevents enough moisture, chloride, and oxygen from reaching the interface. The amount of corrosion required to reach this stage can be estimated according to Eq. 6, which can be used to estimate the slope of i_{corr} at the second stage. $^{w}/_{c}$ and A_0 are water-cement ratio and reinforcement's nominal area. In the third stage, i_{corr} stays in the steady state until cracks propagate through the entire cover and reach a width approximately close to 0.1 mm. Beyond this point, the rust starts to dissipate through the cracks and leach outside allowing more ingress of chloride, oxygen, and moisture; therefore, i_{corr} increases immensely. Based on the authors observations, the reinforcements are considered fully exposed when the crack level reaches 0.5 mm; therefore, at the fifth stage, i_{corr} behaves as a steady state since constant ingress of chloride, moisture, and oxygen is achieved assuming constant environmental conditions.

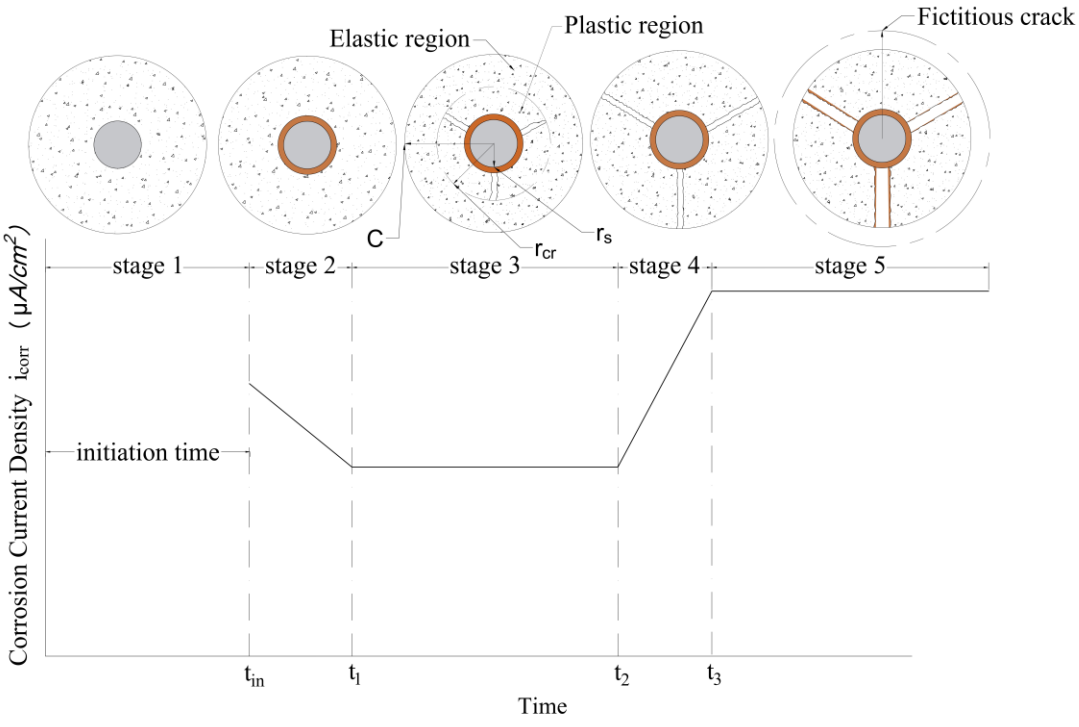

Fig. 6. Corrosion current density development based on cracks level.

$$P_{steady} = P_{avg}(t_1) = (0.0302\ {}^{w}/_{c} - 0.0111)\ A_0 \tag{6}$$

In previous studies, investigations were only limited up to the end of the third stage; i_{corr} variation in the fourth stage is assumed to change linearly with crack width. Eq. 7 gives the relevant formula for estimating i_{corr} at any stage. $i_{o,a}$, $i_{o,c}$, β,& ΔE_e are anodic and cathodic exchange current densities, anodic and cathodic Tafel slopes summation, and equilibrium potentials difference between anodic and cathodic regions, respectively. Detailed calculations of these are provided in Appendix I.

$$i_{corr}(t) = \begin{cases} 0 & t \le t_{in} \\ \frac{1}{4}\ {i_{o,a}}^{0.5}\ i_{o,c}^{0.5}\ e^{\left(\frac{\Delta E_e}{\beta}\right)} & t_{in} < t \le t_1 \\ i_{corr}(t_1) & t_1 < t \le t_2 \\ i_{corr}(t_2) + \frac{w(t-1)-w(t-2)}{w(t-2)}\ i_{corr}(t_2) & t_2 < t < t_3 \\ i_{corr}(t_3) & t \ge t_3 \end{cases} \tag{7}$$

To estimate the average amount of corrosion, P_{avg}, Eq. 8 is used, which is based on Faraday's law discussed in ASTM G102 (2015). k_1 is an empirical coefficient ($g/\mu A$), ρ is the steel density (g/cm^3), and EW is the equivalent weight (g).

$$p_{avg}(t) = k_1 \frac{i_{corr}(t-1)}{\rho}\ EW\ + p_{avg}(t-1) \tag{8}$$

To estimate crack width, a thick wall cylinder approach is adopted. This model was used previously by other authors such as Bhargava et al. (2007), Coccai et al. (2016), and Lau et al. (2018). Because cracks propagate gradually, the analysis included in this approach can be divided into three main phases; uncracked (elastic), partially cracked (elastoplastic), and fully cracked

(plastic), which are equivalent to stages 2, 3, and 4 in **Fig. 6.** Main assumptions in this approach are that the generated rust, V_{rust}, can occupy the space in the capillary pores V_{pores}, the space provided by the radial displacement $V_{U_{rs}}$, and cracks V_{cracks}, as shown in Eqs. 9 & 10, respectively. In the second stage, rust occupies the capillary pores V_{pores}, and the volume induced by the elastic radial displacement $V_{U_{rs}}$, while hoop stress σ_{t,r_s}, at the interface r_s, is less than the tensile strength of concrete. In the third stage, rust additionally occupies the cracks V_{cracks}; σ_{t,r_s}, exceeds the tensile strength of concrete; and the radial compression stress σ_{r,r_s}, is developed by concrete in the elastic and plastic regions considering the softening effect of concrete due to cracking according to Roelfstra & Wittmann (1986) and Coccai et al. (2016). In the fourth stage, the concrete is completely cracked; this means that the σ_{r,r_s}, is completely developed by the cracked concrete. Also, it is assumed that the deformation at a distance r from the center of the cylinder equals the concrete deformation plus the total crack width as shown in Eqs. 11 & 12. $\varepsilon_{t,cr}$ is the ultimate tensile strain of concrete; r_{cr} is the radius of the cracked cylinder; n is the number of cracks in the concrete cylinder; w is the mean width of cracks per unit length of l_{cr}. procedure for calculating all stages σ_{t,r_s}, $\sigma_{r,r}$, U_{rs}, w, and l_{cr} are provided in **Appendix AI**.

$$V_{rust} = V_{pores} + V_{U_{rs}} + V_{cracks} \tag{9}$$

$$\pi\alpha(2r_s P_{avg}(t) - P_{avg}(\mathrm{t})^2) = \pi(2r_s(P_{avg}(\mathrm{t}) + P_{steady}) - (P_{avg}(\mathrm{t}) + P_{steady})) + \pi(2r_s U_{rs}(\mathrm{t}) + U_{rs}(\mathrm{t})^2) + nwl_{cr} \tag{10}$$

$$\Delta_{tot} = \Delta_{con} + \Delta_{cracks} \tag{11}$$

$$\Delta_{tot}(r) = 2\pi\varepsilon_{t,cr} r_{cr} = 2\pi\varepsilon_{t,cr} r + nwl_{cr} \tag{12}$$

It is important to note that the thick wall cylinder model is only valid until cracks reach the surface (i.e., $w = 0$ at the surface). Therefore, to overcome this issue, a fictitious cylinder with a

large radius (i.e., $r \gg {}^{c}/_{2}$) is assumed and the crack width is calculated at the true surface (i.e., $r = {}^{c}/_{2}$). A summary of the calculation procedure is provided in **Fig.7.** The suggested procedure is divided into two main phases. This first phase is applied once during the analysis. First, a series of the radii r_{cr} of the cracked part of the cylinder is generated from the interface r_s up to the fictitious radius, which is assumed to be ten times the cover thickness. Furthermore, the corresponding radial displacements U_{rs} and length of cracks l_{cr}, and crack width w are calculated according to Eqs. 13,14, &15, respectively. Finally, the level of corrosion penetration corresponding to each level of cracking P_{cr} is calculated according to Eq. 16. This parameter, along with the rest will be utilized to obtain the real crack width that corresponds to time-dependent average corrosion penetration as illustrated in the second phase in **Fig. 7.** The second phase will be repeatedly applied over the analysis period to generate the pattern of crack propagation throughout the service life.

$$U_{rs} = \varepsilon_{t,cr} r_{cr} \left[1 + \left(\frac{c^2 - {r_{cr}}^2}{c^2 + {r_{cr}}^2} \right) + \ln\left(\frac{r_{cr}}{r_s} \right) + b \left(ln\left(\frac{r_{cr}}{r_s} \right) - 1 + \left(\frac{r_{cr}}{r_s} \right) \right) + \frac{\pi\, r_{cr}}{n\, w_0} \frac{a\, \varepsilon_{t,cr}}{2} \left(2\, ln\left(\frac{r_{cr}}{r_s} \right) - 3 + 4 \left(\frac{r_{cr}}{r_s} \right)^2 \right) \right] \quad (13)$$

$$\mathrm{l}_{cr} = r_{cr} - (r_s + \mathrm{U}_{cr}) \quad (14)$$

$$w = \frac{2\pi \varepsilon_{t,cr} (r_{cr} - r)}{n\, l_{cr}} \quad (15)$$

$$P_{cr} = r_s - \sqrt{r_s^2 - \frac{U_{rs}^2 + 2\, r_s U_{rs}^2 + n \frac{w\, l_{cr}}{\pi}}{\alpha - 1}} \quad (16)$$

Finally, the estimated crack width at any time $w(t)$ can be compared with the allowable limit w_{limit} as shown in Eq. 17, which is $0.1 inch$ ($0.254\ mm$) according to ASTM C76 (2022).

$$CWLS(t) = w(t) - w_{limit} \quad (17)$$

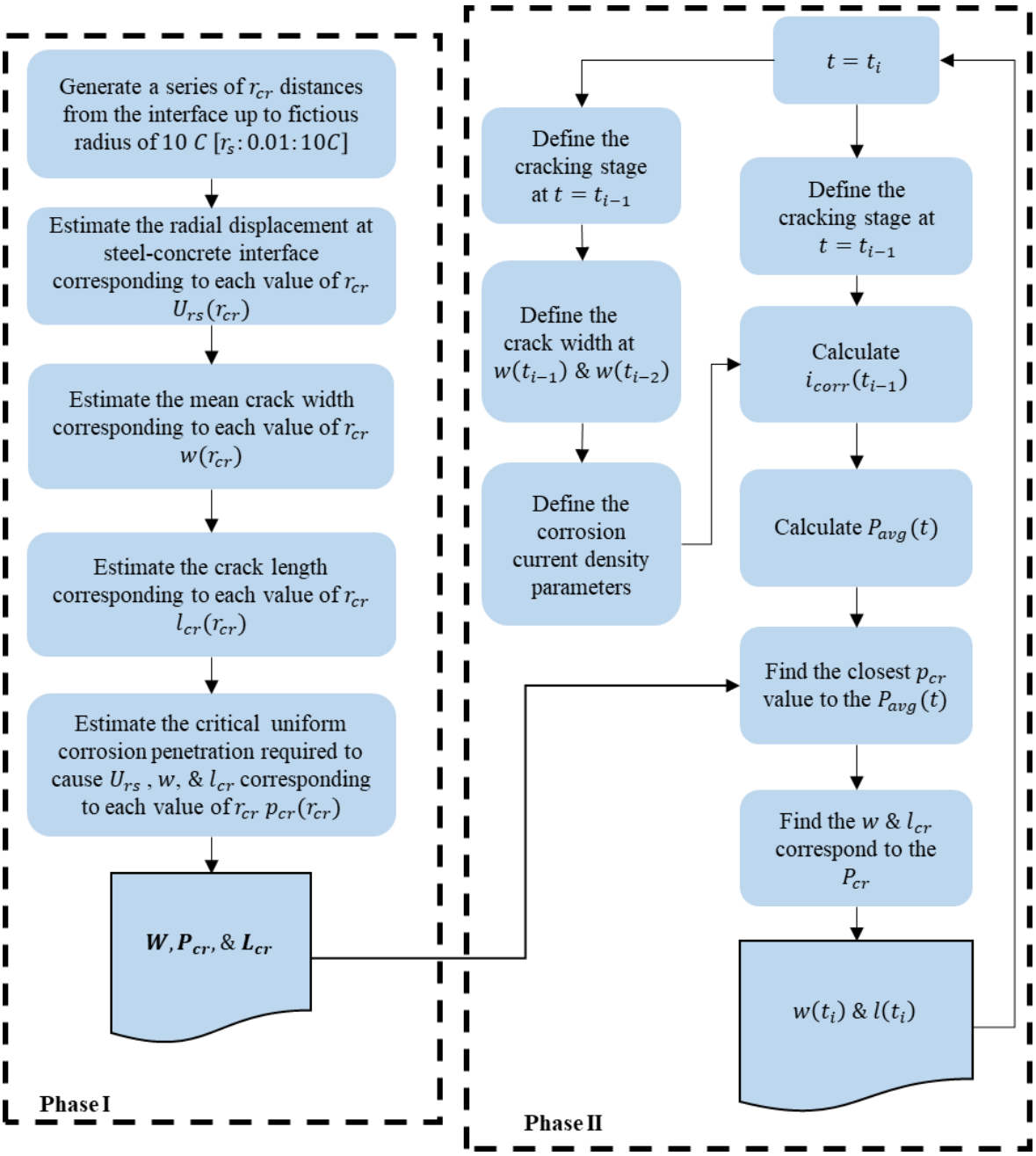

Fig. 7. Suggested procedure for crack width estimation.

3.2.1.3.Bond strength limit state

Generally, the bond strength is attributed to different factors such as chemical adhesion, friction forces, and the bearing force against the ribs of the reinforcement (Zhou et al. 2016). Also, according to Coronelli (2002) and Coccai et al. (2016), the bond strength is attained by other factors such as the confinement provided by surrounding concrete τ_{conc}, and stirrups τ_{stir}, in addition to corrosion product τ_{cr} as shown in Eq. 18. During initial corrosion stages corrosion stages and prior to cracking initiation (stage 2 and 3 in **Fig. 6**), rust occupies the capillary zone and the elastic radial displacement U_{rs}, at the interface, which as a result cause increase the radial compression stress σ_{r,r_s},and leads to the development of the confinement pressure. and the bond strength τ_{cr}. At later stages of corrosion, when cracks start to propagate the confinements provided by the concrete and rust decrease due to tension tension-softening effect of cracked concrete and the dissipation of rust through cracks, respectively.

$$\tau(t)= \tau_{cr}(t)+ \tau_{conc}(t)+ \tau_{stir}(t)+ \tau_{Ad\&Fr}(\mathrm{t}) \tag{18}$$

In this research, the model in Eq. 19 will be adopted for estimating τ_{cr}. This model is developed by Coccai et al. (2016), which depends on $\sigma_{r,r_s}$and coefficient of friction μ. The effect of p_{avg} on the friction will be considered using an empirical model modified by Bhargava et al. (2007) (Eq.20), in which, p_{crack} is the corrosion penetration required to induce cracks throughout the cover ($r_{cr} = {}^{c}/_{2}$). The radial compression stress σ_{r,r_s}, which depends on the level of corrosion and cracking can be calculated as guided in **Appendix AI.**

$$\tau_{cr}\left(p_{avg}(t)\right) = \mu\left(p_{avg}(t)\right)\sigma_{r,rs}\left(p_{avg}(t)\right) \tag{19}$$

$$\mu\left(p_{avg}(t)\right) = 0.37 - 0.26\left(p_{avg}(t) - p_{crack}\right) \tag{20}$$

As cracking propagates through the cover, the tensile strength of the concrete f_{ct} deteriorates significantly under the effect of soft tension estimated according to the bilinear tension softening model presented by Roelfstra & Wittmann (1986), shown in **Fig 8**, and described in Eq. 21. Parameters a and b used in Eqs. 13&21 and for assessing the σ_{r,r_s} in partial cracked and fully cracked stages can be estimated from this model as guided in **Appendix AI.** As a result of f_{ct} reduction, the confinement pressure from concrete $P_{max,c}$ reduces, too according to Eq. 22; furthermore, corrosion effects not only the f_{ct}, but also the friction $\emptyset$, and the ribs angle δ as shown in Eq. 23. Both cause reduction in the τ_{conc} reduces as shown in Eq .24.

$$\tau_{conc}\left(p_{avg}(t)\right) = \frac{n_{ribs} C_r tan(\delta+\emptyset)(p_{avg}(t))}{\pi} P_{max,c}\left(p_{avg}(t)\right) \tag{21}$$

$$P_{max,c}\left(p_{avg}(t)\right) = \left[\frac{b_1}{n_{bar}\left(2r_s\, p_{avg}(t)+2d_c p_{avg}(t)\right)} - 1\right] f_{ct}\left(p_{avg}(t)\right) \tag{22}$$

$$tan(\delta + \emptyset)\left(p_{avg}(t)\right) = 1.857 - 0.9285\, p_{avg}(t) \tag{23}$$

$$f_{ct}\left(p_{avg}(t)\right) = \left[a\frac{w(t)}{w_0} + b\right] f_{ct0} \tag{24}$$

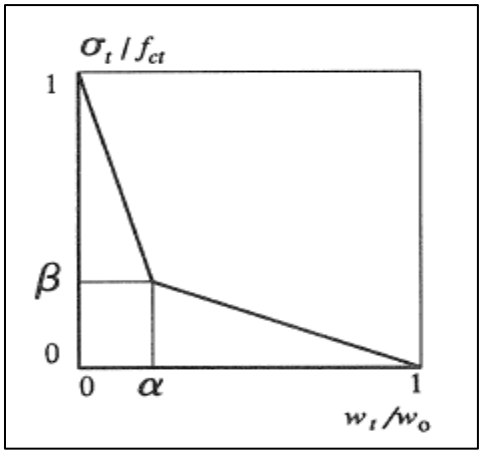

Fig. 8. Bilinear soft tensioning model (Roelfstra & Wittmann 1986).

At the early stages of the corrosion process, the presence of ribs in reinforcement provides additional bonding strength in addition to the friction as concrete bears against them. However, corrosion induces geometrical changes in the reinforcement (such as the disintegrating of ribs) and therefore, eliminating the bearing contribution gradually. Coronelli (2002) has modified the adhesion and friction contribution $\tau_{Ad\&Fr}(t)$ to include corrosion impacts as shown in Eqs. 25 through 28.

$$\tau_{Ad\&Fr}\left(p_{avg}(t)\right) = \frac{n_{rib}A_r(p_{avg}(t))f_{coh}(p_{avg}(t))[\cot\delta(p_{avg}(t))+\tan(\delta+\emptyset)\,(p_{avg}(t))]}{2\pi r_r(p_{avg}(t))\,S_r} \quad (25)$$

$$\cot\delta\left(p_{avg}(t)\right) = 1.687 - 0.825(p_{avg}(t) - 0.6P_{crack}) \quad (26)$$

$$\cot\delta\left(p_{avg}(t)\right) = 1.687 - 0.825(p_{avg}(t) - 0.6P_{crack}) \quad (27)$$

$$f_{coh}\left(p_{avg}(t)\right) = 3.41 - 21.21\left(p_{avg}(t) - P_{crack}\right) \quad (28)$$

Finally, the total bond strength $\tau(t)$ at any time can be compared to the pull-out stress estimated according to clause 12.2 in ACI 318R (2019), while the reliability of the pipes against pull-out failure under the effect of corrosion can be estimated according to Eqs. 29 & 30.

$$BSLLS(t)=\tau(t) - pullout\ stress \quad (29)$$

$$pullout\ stress = \frac{M_s}{2A_{rs}f_y\left(d-\frac{a_1}{2}\right)\pi r_r\,L_d} \quad (30)$$

3.2.2. Ultimate Level Limit States Functions

3.2.2.1. Reinforcement Ductility Loss Limit State

As discussed in **Section 1.2.2** and in **Section 3.2.1.2**, chloride-induced corrosion has multiple deterioration aspects such as cracking w and reduction in reinforcement area A_{rs}. Yet,

another important aspect that is more detrimental than the first two is the reduction of mechanical properties of concrete and reinforcements. This aspect has not been considered in previous studies, despite its importance. The main characteristic of chloride corrosion is its pitting nature, in which rust development is neither uniform along the perimeter, nor along the reinforcements. Song et al. (2019) found that during the initial stages, rust accumulates at the location closer to the concrete surface, and then it starts to dissipate along the perimeter at high cracking stages due to oxygen and moisture surplus. This means that the distribution of rust is not uniform during the service life. Hingorani et al. (2013) conducted spatial variability analysis to investigate the distribution of rust. They found that the ratio of rust at the max penetration to rust at other locations, R, follows extreme value distribution. This factor can be used effectively to estimate the maximum corrosion penetration $P_{max}(t)$ from $p_{avg}(t)$ as shown in Eq. 31.

$$P_{max}(t) = R\, P_{avg}(t) \tag{31}$$

Because of the pitting nature, it is important to note that the residual area of the reinforcement is not the same as in uniform corrosion A_{rs}. Stewart & Harthy (2008) suggested the calculations shown in the **Appendix AI** of the residual area considering the pitting effect A_{pit}.

On the other hand, the effect of pitting corrosion on the mechanical properties of concrete and reinforcements was investigated in several studies (Du et al. 2005; Stewart & Harthy 2008; Stewart & Suo 2009; Hanjari et al. 2011; Imperatore et al. 2017; Fernandez & Berrocal 2019; Vanama & Ramakrishnan 2020). They found that pitting corrosion adversely affects the yield strength f_y, the ultimate strain ε_u, and the ultimate strength f_u. After significant experiments and regression analysis, they found that the reduction behavior of ε_u follows a linear or exponential trend, while it is completely linear for f_y and f_u.

In RCSPs, wire reinforcement is commonly used, which has high yield strength and low ultimate strain; therefore, it is important to consider the reduction of the ε_u and as a result, the ductility over the lifetime of the pipe. In this study, both exponential and linear trends will be considered in evaluating ε_u as shown in Eq. 32. The residual $\varepsilon_u(t)$ will be compared to ε_y as shown in Eq. 33 to report ductility loss or reinforcement brittle failure. it is assumed that brittle failure occurs when $\varepsilon_u(t)$ reaches ε_y.

$$\varepsilon_u(t) = max\left\{\begin{matrix} \varepsilon_{u0}^{-\alpha_1 \frac{A_{pit}(t)}{A_0}} \\ \left(1 - \alpha_1 \frac{A_{pit}(t)}{A_0}\right)\varepsilon_{u0} \end{matrix}\right\} \tag{32}$$

$$DLLS(t) = \varepsilon_u(t) - \varepsilon_y \tag{33}$$

The reduction in yield strength f_y will also be considered in the upcoming limit state function as shown in Eq. 34. In addition, the impact of pitting corrosion $P_{max}(t)$ on the concrete compressive strength was investigated by Vecchio & Collins (1986) and provided in Eqs. 35 & 36.

$$f_y(t) = \left(1 - \alpha_y \frac{A_{pit}(t)}{A_0}\right) f_{y0} \tag{34}$$

$$f'_c\left(P_{max}(t)\right) = \frac{f'_{c0}}{1+0.1\frac{\varepsilon_1(P_{max}(t))}{\varepsilon_{cr}}} \tag{35}$$

$$\varepsilon_1\left(P_{max}(t)\right) = \frac{2\pi\, n_{bars}(\alpha-1)P_{max}(t)}{b_1} \tag{36}$$

3.2.2.2. Flexural, Shear, And Radial Tension Limit States

Originally, RCSPs were designed using a 3-edge D-Load test (indirect design method); however, another option based on the standard installation direct design method (SIDD) (ASCE

15. 1998) is available. This method is used in situations where the indirect design method is not practical; for example, when pipes have high fill depth or large diameter; therefore, it is impractical to conduct the test. Another reason for using the SIDD method is the need for shear design; the indirect design method assumes that shear capacity is attained by the wall thickness and no shear reinforcements are required (Beakley et al. 2020). The SIDD method allows analytical calculations of applied moment M_u, shear V_u, and thrust N_u, loads on the pipe using Heger's soil distribution factors (Heger 1962), which depends on the type of installation whether it is embankment or trench installation as shown in **Appendix AI**. In addition, these factors depend on the type of soil and compaction requirements and are available in ASCE 15 (1998). Calculations of M_u, V_u, and N_u are based on thin ring theory with elastic material properties. These calculated forces are higher than the true forces for small-diameter pipes or for large thickness-to-radius ratio pipes, which results in over conservatism. Typical loads on pipes including earth load W_e, own weight W_p, fluid load W_f , and longitudinal and lateral live loads W_{LL1} & W_{LL2} can be obtained according to (AASHTO) LRFD Ch 12 (2019). In this study, three ultimate limit state functions are adopted from this method. The first one is the flexural strength limit state function $FLLS(t)$, shown in Eq. 37, which assumes complete yield in reinforcement and considers the contribution of thrust load N_u, in the strength. The second limit state is the shear strength limit state function $SLLS(t)$, shown in Eq. 39. This function includes the basic shear formula, which reflects the lowest shear strength that a pipe can sustain at its critical section ($M/Vd = 3$) without shear reinforcement. The basic shear strength equals the general shear strength of concrete at the section $M/Vd \geq 3$ where the moment is no longer affecting shear (Heger & McGrath 1982). The effect of N_u is also considered; compressive N_u increases the shear strength; however tensile N_u adversely affects the shear strength and could eliminate the shear strength if it exceeds the tensile strength of concrete as shear

is only resisted by concrete. The last limit state function is the radial tension strength limit state function $RTLLS(t)$, shown in Eq. 40. Radial tension stress can be produced due to ring bending or other stresses from internal or external pressure. The last one is negligible at the region where maximum ring bending occurs. The equation used in the SIDD method considers only radial tension due to ring bending. According to Heger & McGrath (1982), in curved flexural members, flexural strength is controlled or limited by the radial tension capacity of concrete since concrete is obliged to counteract the radial tension component in flexural reinforcement. In addition, the SIDD method considers the effect of pipe size explained through factor F_{rt}, which entails that as the pipe size decrease, the relative proportion of cover thickness to wall thickness is larger, and flexural forces are lower; therefore, radial tension capacity increase. Calculation guide for factors such as F_d, F_c, & F_{rt} are provided in the **Appendix AI**.

$$FLLS(t) = M_u - \left[\theta_f \left[A_{rs}\left(P_{max}(t)\right) f_y\left(P_{max}(t)\right)\left(d - \frac{a_1}{2}\right)\right] + 0.5\, N_u (h_r(t) - a_1)\right] \tag{37}$$

$$a_1 = \frac{A_{rs}\left(P_{max}(t)\right) f_y\left(P_{max}(t)\right) + N_u}{0.85\, f_c\left(P_{max}(t)\right) b_1} \tag{38}$$

$$SLLS(t) = V_u - 0.083 b_1\, \theta_{vp}\, d\, F_{vp} \sqrt{f_c\left(P_{max}(t)\right)}\left(1.1 + 63\frac{A_{rs}\left(P_{max}(t)\right)}{b_1 d}\right)\left[\frac{F_d}{F_c}\right]\left[1 + \frac{N_u}{14 h_r(t) b_1}\right] \tag{39}$$

$$RTLLS(t) = \frac{M_u - 0.45\, N_u\, d}{b_1 R_s\, d} - 0.01\, F_{vp}\, F_{rt} \sqrt{f_c\left(P_{max}(t)\right)} \tag{40}$$

3.2.3. Ultimate and Service Reliability

In the previous section, failure mechanisms in RCSPs were discussed and integrated into limit state functions for reliability evaluation. Each of these functions is responsible for the reliability against a specific failure mode; however, to have a complete visionary and logical representation of the combined effect, a reliability block diagram (RBD) is used as previously

explored by Mohamoodian & Alani (2014) and Alani & Faramarzi (2015). In this study, the arrangement of limit state functions in RBD at both levels is shown in **Fig. 9a & 9b**. In **Fig. 9a**, the serviceability limit state functions are set in parallel configuration to reflect redundancy, which means that all limit states at this level must be exceeded to reflect serviceability loss. Therefore, the likelihood of serviceability loss can be obtained using Eq. 41, which is similar to the "OR" logic operation. In **Fig. 9b**, the ultimate limit state functions are set in a series configuration, which means at least one limit state at this level must be exceeded to reflect ultimate failure. Therefore, the likelihood of failure can be obtained using Eq. 42, which is similar to the "AND" logic operation.

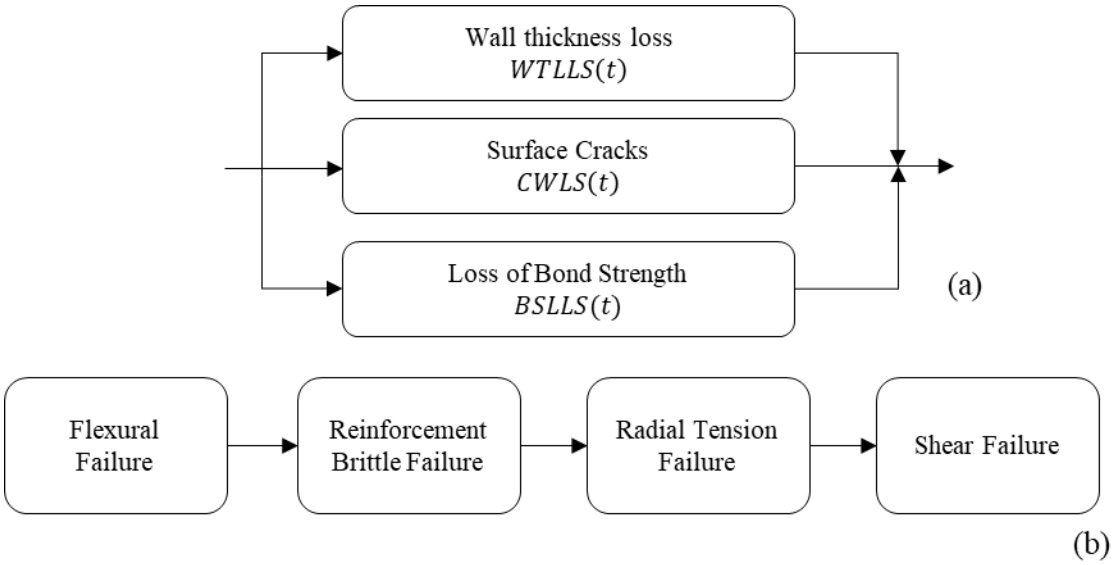

Fig. 9. (a) RBD at the serviceability level; **(b)** RBD at the ultimate level.

$$P_{service}(t) = \prod_{n=1}^{3} P_n(t) \tag{41}$$

$$P_{failure}(t) = 1 - \prod_{n=1}^{4}\big(1 - P_n(t)\big) \tag{42}$$

The service life and failure time can be obtained by comparing $P_{service}(t)$ and $P_{failure}(t)$ with their permissible values P_{limit}.

3.2.4. Monte-Carlo Simulation

To investigate the likelihood of failure at both ultimate and service levels at any time, reliability analysis should be conducted, and limit state functions should be evaluated at each time step. This process demands evaluation of input parameters every time step. However, because most of the input parameters are hard to measure or carry significant uncertainties, it is important to evaluate the limit states at all possible values to avoid biased estimation assuming input parameters as random variables rather than deterministic values. To estimate the mean response of the limit state function, Eq. 43 should be applied; however, this is computationally expensive as it requires n times integrations, where n is the number of random input variables, $f(\boldsymbol{x})$ is the joint probability density function of random variables and $h(\boldsymbol{x})$ is the limit state function of random variables.

$$E[h(\boldsymbol{x})] = \iiint f(\boldsymbol{x})h(\boldsymbol{x}) \tag{43}$$

For this reason, Monte-Carlo simulation is adopted, which estimates the mean response by sampling from random variables N samples, evaluates $h(\boldsymbol{x})$ at each sample, and takes the arithmetic average as shown in Eq.44. As the number of samples increases, the variance of the expected outcome decreases as shown in Eq. 45.

$$E[h(\boldsymbol{x})] = \frac{h(\boldsymbol{x})}{N} \tag{44}$$

$$\sigma^2 = \frac{\sum_{i=1}^{N} h(\boldsymbol{x}_i) - E[h(\boldsymbol{x})]}{N-1} \tag{45}$$

In this research, Monte-Carlo simulation with an effective Latin hypercube sampling technique is used. This technique will generate an equivalent number of samples across different

input domains, which will effectively reduce the number of required simulations runs (Olsson et al 2003), hence the variance. The Monte-Carlo simulation will be applied in two consecutive stages. in the first stage, the goal of the simulation is to estimate the initiation time of chloride-induced corrosion and sulfide-induced erosion. The outcomes of this stage will be integrated into the next stage to evaluate the rest of the limit state functions. A summary of the two stages is provided in **Fig. 10**. As shown there, the Monte-Carlo simulation is conducted at both stages; sampling is done initially followed by evaluation of limit state functions at each time step considering the time effect on specific input variables and on the limit state functions. To estimate the likelihood of failure or exceedance at each time step for each limit state function, Eq. 46 is used, which is the number of samples at which the strength is exceeded, or the limit state function is below zero divided by the total number of simulations.

$$P = \frac{count(LS<0)}{N} \tag{46}$$

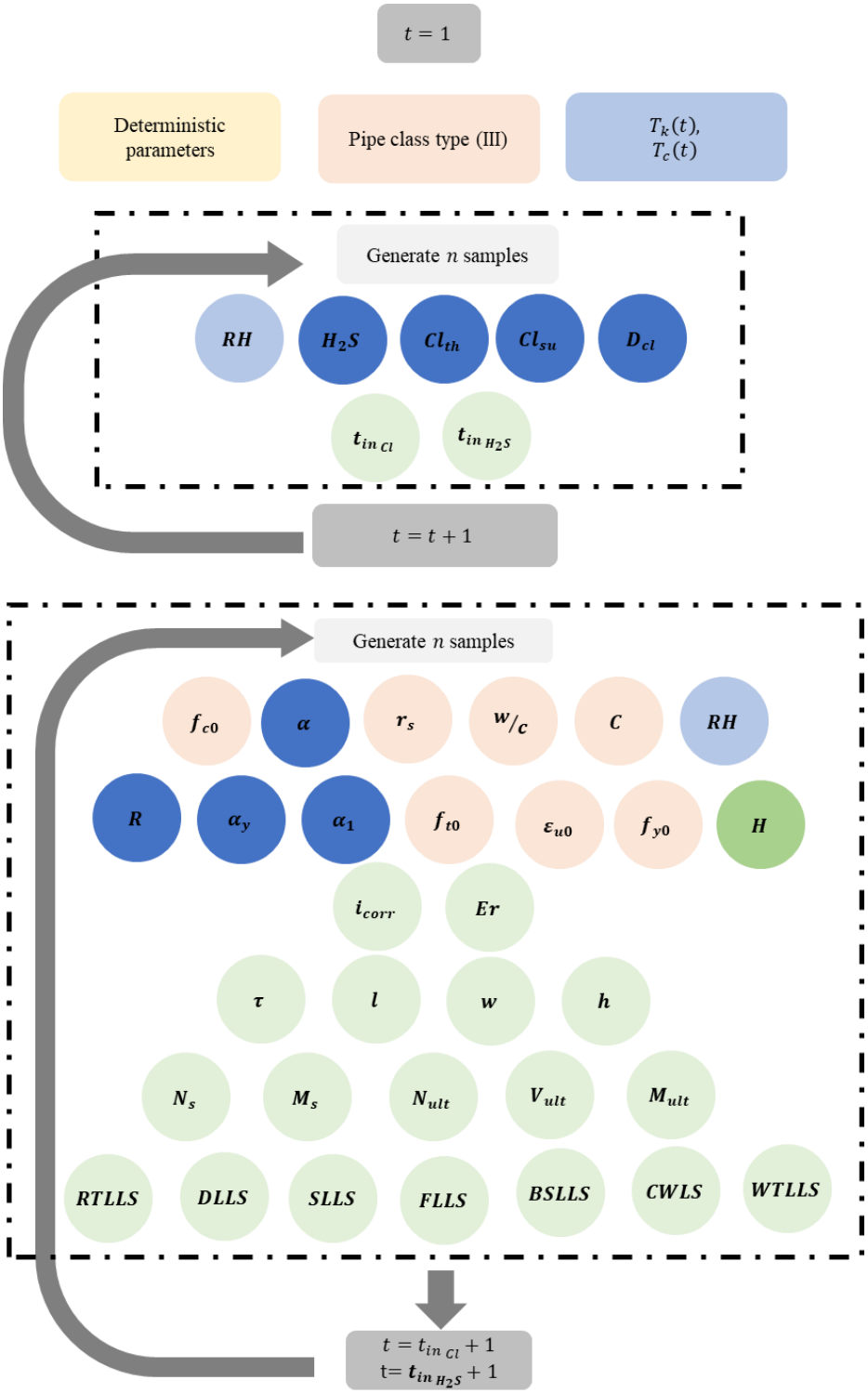

Fig. 10. Two-stage Monte-Carlo simulation for determining initiation time and limit states evaluations.

3.3. Consequences of Failure

When RCSPs reach their anticipated service life or failure time, there will be adverse consequences. These consequences can be slight, moderate, or catastrophic depending on different impact factors. These factors are mostly related to pipe geometrical properties to reflect the cost of replacement or rehabilitation, proximity to adjacent critical structures, road type to reflect the traffic volume, user cost, the community at which the pipe is located, the type of building that the pipe serve, etc… Based on the literature review provided in **Section 2.3,** The state-of-practice of consequences evaluation is based on qualitative approaches, which depends on a set of criteria related to impact factors defined by agencies or decision-makers. The reasons for choosing qualitative approaches rather than quantitative approaches are the limitations, difficulties, and uncertainties in quantifying datasets and information related to the impact factors, hence the consequences. The goal of this study is to provide a probabilistic framework for quantitative monetary evaluation of consequences, which manifests clarity and interpretability while considering impact factors uncertainties. The consequences considered in the proposed approach can be classified into two different classes, as shown in **Fig.11**. The first class is designated as the direct cost, which includes all factors entitled to or paid by the agencies responsible for maintaining the service of these structures, while the second class is designated as the indirect cost and resembles all impact factors entitled or paid by surrounding communities other than agencies (Elmasry et al. 2017). Details about these classes are discussed in the subsequent section.

The consequences of structural failure or serviceability loss stay effective from the time at which the lifetime or the service life is anticipated to end with a certain likelihood until the completion of rehabilitation or replacement actions required to retain the integrity of the structure.

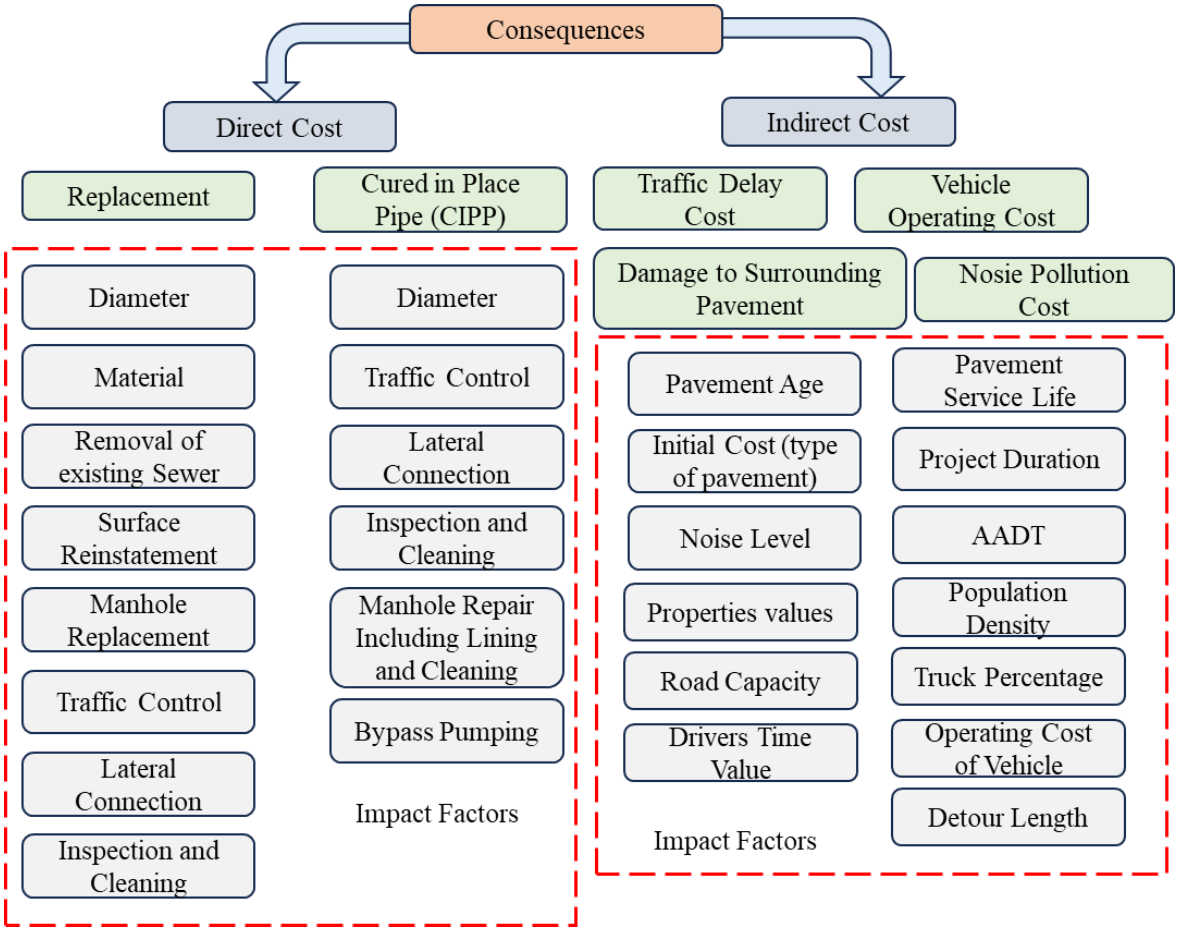

Fig. 11. List of Impact factors belonging to each class of consequences.

3.3.1. Direct Cost

This is the cost, or the consequences associated with the implementation of rehabilitation or construction (Matthew & Allouche 2010; Elmasry et al. 2017). This cost is paid by agencies who own the structures and depends on the intended methodology and the number of activities required to retain the structural integrity or to extend the service life of these structures. For example, the cost of pipe replacement includes the cost of the material per linear foot (which depends on the geometrical properties, i.e., diameter and thickness), the cost of excavation, installation, surface restoration, and additional site-related costs. There are a significant number of

technologies that can be used effectively to reinstate the pipes in general and are classified as rehabilitation or replacement technologies. The rehabilitation technologies include repair, and renovation techniques, which are applied locally or along the entire length of the pipe, respectively, to improve the current performance or the structural integrities. An example of repair methods is repaired by injections, sealers with mechanical devices, and cured-in-place patches. Renovation techniques are mostly related to lining practices such as cured-in-place pipe (CIPP). The replacement technologies include traditional open-cut or more advanced methods such as hammer drilling and pipe bursting, which are expected to reinstate the structural integrity to its inventory level. A more detailed discussion about these technologies including their advantages and disadvantages, and their applicability are demonstrated by Almeida et al. (2015).

In this study, it is assumed that a rehabilitation or replacement technique should be conducted whenever the likelihood of serviceability loss, $P_{service}(t)$, or the likelihood of failure, $P_{failure}(t)$, exceeds a threshold value. At the serviceability level, a CIPP pipe will be considered as a rehabilitation technique. Installation of CIPP requires first cleaning and CCTV inspection of the pipe, followed by installing a thin plastic tube through direct inversion or pullout, which is later attached to the pipe perimeter through air pressure or water. This tube includes resins, which are cured using hot steam/UV-light to gain strength. The last process includes reinstating any laterals connected to the pipe and performing a post-completion inspection for quality control. Details about installation methodology and different classes of CIPP are provided in AWWA M28 (2014) and ASTM F1216 (2016). The replacement technique adopted in this study is the traditional open-cut (dig-replace) method, which includes excavation to reach the defective pipe, abandoning the old pipe, and replacing it with a new one. After installing the new pipe, additional activities

might be accomplished including manhole replacement or repair, pavement, and surrounding surface restorations.

The impact factors that control either technique is exemplified in **Fig.11**, which are selected after reviewing a set of bidding tabs of projects in which either technique is adopted. Some of these impact factors are common in both techniques; for example, the diameter of the rehabilitated or the new pipe, traffic control (adding signals or signs at the working zone), lateral connection, inspection, and cleaning.; however, others are technique specific.

In this study, the goal is to build a probabilistic prediction regression model for estimating the direct cost of both techniques, which allows consideration of uncertainties in the data. **Fig. 12** gives a summary of the suggested work.

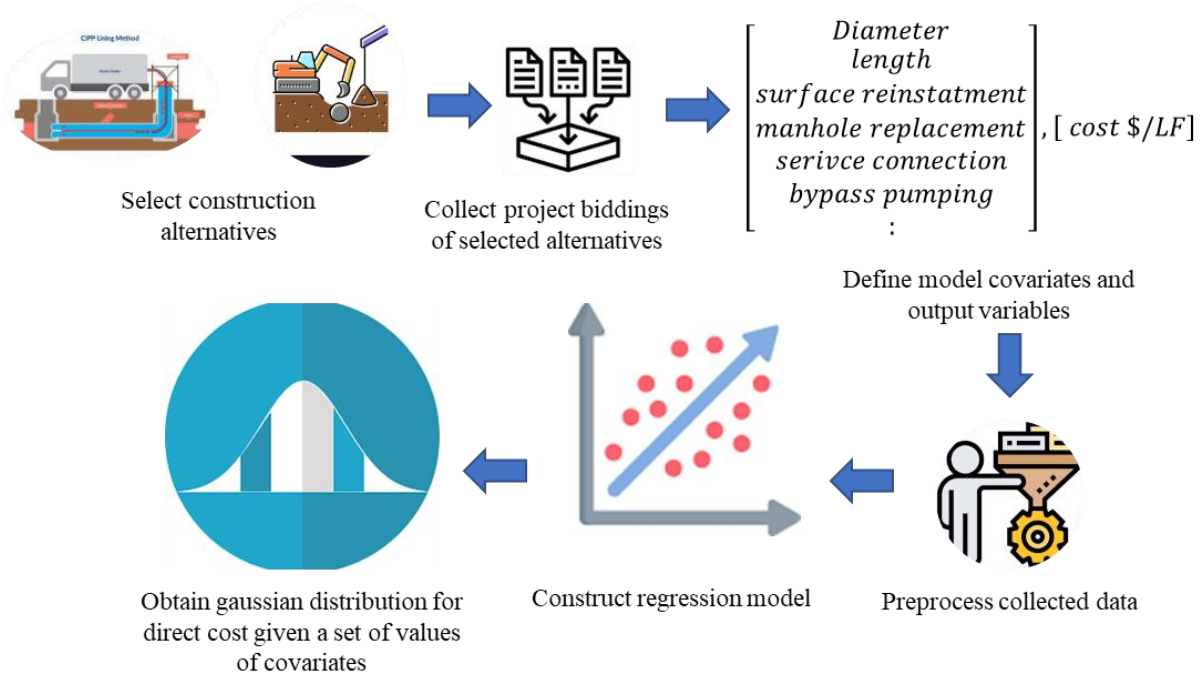

Fig. 12. Suggested methodology to obtain a predictive distribution of the direct cost.

The framework starts by collecting bidding tabs related to both techniques, then extracting the cost of the features or the impact factors shown in **Fig. 11.** In the bidding tabs it is common to find the cost of impact factors are given in different units such as numbers, lump sum, or squared foot; however, the response (i.e., direct cost) is desired to be expressed in $\$/LF$. Therefore, the costs of these factors are divided by the length of the pipe under investigation. Once the costs of impact factors are extracted and converted to $\$/LF$, they are all summed up to constitute the total cost. To conduct the regression analysis, predictors and responses should be given. The response should be obtained as discussed earlier, while the predictors are expressed in a one-hot encoding format for all impact factors other than the diameter. A sample of the processed dataset to be used for training and validating the regression model is shown in **Table 1**.

Table 1. Sample of dataset for either technique used to train and validate the regression model.

Dir_Cost $(\$/LF)$	$Diameter$ $(inch)$	IF_1	IF_2	IF_3	IF_4	IF_5	IF_6
120	18	1	0	1	0	0	0
:	:	:	:	:	:	:	:
:	:	:	:	:	:	:	:
135	24	1	1	1	0	0	1

In total, 62 and 72 observations for replacement and CIPP techniques, respectively, are going to be used to train and validate a multi-linear regression model. The suggested multi-linear regression will be constructed using stepwise regression to allow the most significant predictors interactions to be in the model. In the first step, stepwise regression will be conducted on the entire dataset to get the most significant parameters including second-degree interactions among predictors. The significance of predictors will be determined based on P-value criteria assuming a 95% confidence level. After obtaining significant predictors, a 10-fold cross-validation approach

is used to train and validate the models considering the new predictors, which results in ten different models for each technique. The model that provides the least mean absolute error on the validation set is selected and the rest is discarded. The results of the stepwise regression model and 10-fold cross-validation for both replacement and CIPP alternatives are displayed in **Table 2** and **Table 3.**

Table 2. Coefficients and statistics of multi-linear regression model for replacement.

predictors	Coeff	P_values	Statistics
Dia	6.3	$1.9e-15$	$R^2 = 0.989$
PVC	-116.17	$1.26e-7$	$F\_stat = 398.5$
$Surf\ Reinst$	57.56	$6.2e-3$	$Log\_Lik = -234$
$Man\ Rep$	160.76	$4.75e-8$	$MAE = 22.18$
$Traff$	45.6	$3.82e-4$	$\sigma = 35.75$
$Insp\ \&\ Cl$	122.00	$1.45e-8$	
$Surf\ Reinst\ \_\ Man\ Rep$	-80.69	$1.45e-4$	
$Surf\ Reinst\ \_\ Insp\ \&\ Cl$	-45.72	$1.81e-4$	
$Surf\ Reinst\ \_\ Traff$	45.6	$3.82e-4$	
$Man\ Rep\ \_\ Traff$	69.01	$1.89e-5$	
$Man\ Rep\ \_\ Lat\ Conc$	-92.65	$5.95e-5$	
$Insp\ \&\ Cl\ \_\ Traff$	-45.72	$1.81e-4$	

Table 3. Coefficients and statistics of multi-linear regression model for CIPP alternatives.

predictors	Coeff	P_values	Statistics
$Insp\ \&\ Cl$	-13.73	2.87e-02	$R^2 = 0.977$
$Lat\ Conc$	47.55	8.20e-09	$F\_stat = 355.7$
$Man\ Reh$	106.92	2.98e-09	$Log\_Lik = -291.43$
$Bypass$	77.63	3.73e-06	$MAE = 15.21$
$Insp\ \&\ Cl\_Bypass$	-85.07	1.54e-06	$\sigma = 26.81$
$Lat\ Conc\_Traff$	47.53	8.20e-09	
$Lat\ Conc\_Bypass$	18.20	3.41e-01	
$Man\ Reh\_Traff$	-182.98	7.47e-10	
$Man\ Reh\_Bypass$	77.57	4.22e-07	

Dia	6.41	2.23e-30

Finally, to have a probabilistic prediction for a given set of values of predictors, Eq. 47 is used, which includes the estimates from the linear regression model above plus the added noise, which is assumed to follow a normal distribution with mean 0 and standard deviation of σ.

$$Dir\_Cost\left(\frac{\$}{LF}\right) = \textbf{predictors Coeff} + \mathrm{N}(0, \sigma) \quad (47)$$

3.3.2. Indirect Cost

This consequences category includes all other costs that impact road users, adjacent structures, and communities. As shown in **Fig. 11**, these costs include traffic delay costs, vehicle operating costs, damage to adjacent pavements due to excavation, and noise costs. All these costs depend on different impact factors that have different values relevant to the direct cost alternatives, the level of urbanization, and road classifications. Details about these costs are provided in the following sections.

3.3.2.1. Pavement Service Life Reduction Due to Excavation & Restoration Cost

Replacement or rehabilitation operations where excavations are demanded to execute operations will significantly impact the reliability and reduce the service life of top adjacent pavement structures due to the reduction of lateral support of remaining pavements and hence, causing a reduction in value and an increase in future maintenance cost (Matthews et al 2014). According to Tighe et al (2002), the expected reduction value of surrounding pavement is expected to reach up to 30%. Ormsby et al (2009) developed an empirical model to estimate the reduction value in pavement based on current age and the expected service life as shown in Eq. 48. This

model reflects the difference between the present value at the original service life and the present value at the reduced service life due to trench excavations, which is assumed to be 70%. Also, the increase in maintenance value can be obtained based on Eq. 49, where $C_{maintenance}$ is the cost of routine maintenance per square ft and A_R is the pavement area under maintenance.

$$C_{Reduction} = intial\ cost\left[1 - \frac{pavement\ age}{service\ life}\right] - initial\ cost\left[1 - \frac{pavement\ age}{(0.3\ pavement\ age + 0.7\ service\ life)}\right] \quad (48)$$

$$C_{in\_maintenace} = C_{maintenance}\ A_R \quad (49)$$

According to the Texas Department of Transportation (TXDOT. 2023)[1] the design life of rigid and flexible pavements is 30 and 20 years, respectively. However, for analysis purposes, 40 years should be used for both. The service life of pavement is defined as the time between two consecutive rehabilitation alternatives. The average service life for both rigid and flexible pavements in the state of Texas is 12 years. Within the service life of pavement, routine maintenance is conducted every 10 years with an average cost of $2,189 and $1,225 per lane per mile for rigid and flexible pavements, respectively. According to the Federal Highway Agency (FHWA 2015), the construction cost of pavement including traffic control is $8 per yard[2] for a 1.5-inch thickness and between $11 and $12 for a 2.5-inch thickness. Based on the life cycle cost analysis conducted by (Andrew et al 2009), the cost of flexible pavement ranges from $449,310 to $527,550 per lane per mile, while it is about $468,620 per lane per mile for rigid ones.

3.3.2.2. Noise Pollution Cost

Excessive construction activities and machine noise can disrupt the surrounding neighbors and therefore temporarily reduces the adjacent properties values due to induced noise. Noise level

defined in decibels (dB) for a typical project varies depending on the equipment used during construction including trucks, pumps, excavators, etc…. This unit of measurement is relative, and it is equal to the logarithmic ratio of the noise pressure to the ambient or reference pressure. Also, it is measured on a logarithmic scale, which means that every 10dB increment results in doubling the sound effect. Noise sources can be classified into either point source, which is caused by activities at a specific location such as in construction projects. It is represented by the maximum decibel level and spreads spherically in three dimensions. The second category of noise source is the line source, which is caused by moving objects along a track such as traffic on a highway (Knauer et al. 2006). Noise level depreciates over twice the distance from the noise source starting from a 50 ft radius and under topographic, atmospheric, and vegetation effects. According to Knauer et al. (2006) and Washington State Department of Transportation (WSDOT) (2012), there are four main steps to assess the noise level induced by a given project. This first step is to estimate the construction equipment noise level. This equipment can be classified as heavy non-impact equipment (such as earth-moving equipment), stationary equipment (such as pumps, and power generators), and heavy impact equipment (such as pile drivers and jackhammers). The ranges of noise levels for this equipment are 73 to 101dB, 68 to 88dB, and 79 to 110dB, respectively. When a project demands multiple equipment running simultaneously, noise levels for all operating equipment should be combined; however, because the noise level is on a logarithmic scale, they cannot be simply summed. A general state of practice for combining noise levels is shown in **Table 4**.

Table 4. Method for combining multiple noise levels running simultaneously (USDOT. 1995).

Difference between the two levels	The amount added to the highest
0 or 1 dB	3dB
2 or 3 dB	2dB
4 to 9 dB	1dB
10dB or more	0dB

The next step is to define the extent of project noise before depreciation to the reference level. Knauer et al. (2006) suggested that the extent of a project's noise depends on the extent of surrounding traffic. A general guideline is that if the distance required by project noise to reach the reference level is greater than the one required by the traffic, then the reference level is the traffic noise level; however, if the opposite is observed, then the reference level is the background level, which depends on the level of development and population intensity. The noise level at a specific distance and the required distance to reach the background level can be calculated according to Eq. 50 & 51. A list of background noise levels measured at 50 ft away from the noise point source is shown in **Table 5**. The traffic noise depends on the volume of traffic, the average speed, and the type of truck running on the road and ranges between 70 to 80dB (Corbisier 2003), which are typical values for traffic noise level provided by WSDOT (2012). Detailed calculation approaches for traffic-induced noise levels are explained by Miller et al. (2014).

$$NL(D) = NL(50ft) - 25\log\left(\frac{D}{50}\right) \tag{50}$$

$$D = 50\ 10^{(NL-NL_{background})/20} \tag{51}$$

In this study, the estimated value reduction in surrounding properties will be estimated according to Eq. 52 (Matthews & Allouche 2010). First the number of populations will be used to select the ambient level of noise and the second step is to estimate the traffic noise. The background

noise will be the largest noise level among traffic and ambient. In the following step, the range of noise level related to construction equipment will be defined and the required distance to reach the background level will be estimated according to Eq. 51. Finally, the average number of properties N_p (assuming a specific number) located with a diameter of this distance and their corresponding values PVs will be implied in Eq. 52 to estimate the reduced values, which is considered one of the indirect cost categories. A correction factor, CN, is added since surrounding properties are not permanently affected and only during project duration. The calculation of the correction factor is shown in **Table 6.**

$$C_{RV} = CN\left(NL - NL_{background}\right) PVs\, N_p \tag{52}$$

Table 5. Background noise level according to population density (Knauer et al. 2006).

Population Density (people per square mile)	Noise level excluding traffic
1-100	35dB
100-300	40dB
300-1000	45dB
1000-3000	50dB
3000-10000	55dB
10000-30000	60dB
>30000	65dB

Table 6. Reduction factor of noise level based on project duration CN (Matthews & Allouche 2010).

Project Duration (Days)	CN
<120	0.05
60	0.1
90	0.2
120	0.3
150	0.4
180	0.5
210	0.6
240	0.7
270	0.8
300	0.9
330	0.95
≥360	1

3.3.2.3. Traffic Delay Cost

When construction activities take place on a road, there will be a complete or partial road closure within the working zone during the project duration. This will cause a loss of time value for drivers and passengers since they must take the detour in case of complete closure or drive at significantly low speed, which eventually will increase the travel time. Also, partially closed roads will divert allocated traffic to adjacent lanes which causes an increase in travel time due to queuing and low-speed traveling (Tighe et al. 1999). The expected delay can be attributed to either speed change delay, stopping delay, reduced speed delay, queue delay, detour delay, or a combination of them. The first two components are related to delays caused by reducing the speed or complete stop when approaching the working zone, respectively, depending on whether there is a queue in the working zone (i.e., demand volume is larger than the capacity) or not. The other components are related to the reduction in traveling speed due to restrictions, the development of queues due

to an increase in demand, deacceleration, or traffic control, and finally, due to traveling for a longer time while taking the detour. According to FHWA (2011), the first two components are neglected by state agencies as they are insignificant concerning others.

Tighe et al. (1999) suggested three possible scenarios of actions taken in the working zone during trenching construction. These scenarios depend on the strategies adopted by decision-makers to deal with approaching traffic.

Scenario I: The road is completely open with traffic controlled by a flag person or signal. In this situation, the expected delay is caused by road capacity reduction due to traffic control, which induces queuing (i.e., the difference between arriving traffic volume and the capacity of the road). The expected delay can be obtained according to Eq. 53 (Tighe et al. 1999), where c, g, HV, C_r are the cycle length, green time, hourly volume per lane, and the reduced capacity, respectively. For this case, the reduced capacity can be calculated according to Eq. 54. Appropriate values for c & g can be found in Tighe et al. (1999), which depends on the average annual daily traffic $AADT$.

$$D_{e\ case\ I} = \frac{0.38\ c\left(1-\frac{g}{c}\right)^2}{3600} + \frac{173\left(\frac{HV}{C_r}\right)^2\left[\left(\frac{HV}{C_r}-1\right)+\left(\left(\frac{HV}{C_r}-1\right)^2+16\frac{HV}{C_r^2}\right)^{0.5}\right]}{3600} \quad (53)$$

$$C_r = C\ g/c \quad (54)$$

Scenario II: the road is partially closed with associated traffic diverted to the shoulder. This case assumes that the shoulder can carry traffic with a capacity similar to the closed lane, which means that the road will maintain its capacity without queuing. Therefore, the expected delay is caused by speed restrictions in the construction zone. In this situation, the expected delay is the difference in the elapsed time under normal speed and restricted speed as shown in Eq. 55. The normal speed can be estimated according to Eq. 56, while the restricted speed is assumed to be $20\ miles/hr$. Finally, the expected delay is estimated according to Eq. 56 in km/hr.

$$D_{e\ case\ II} = \frac{work\ zone\ length}{V_r} - \frac{work\ zone\ length}{V_n} \quad (55)$$

$$V_n = 99.322 - 71.047\left(\frac{HV}{C}\right) + 100.14\left(\frac{HV}{C}\right)^2 - 61.622\ \left(\frac{HV}{C}\right)^3 \quad (56)$$

Scenario III: when the road is completely closed, the capacity reduces to zero and the entire arriving hourly volume C, is diverted to a detour road. The delay time in this situation can be estimated according to Eq. 57, where L is the detour length and the V_n is the design speed in the detour.

$$D_{e\ case\ III} = \frac{L\ HV}{V_n} \quad (57)$$

The normal capacity of a road can be estimated according to Eq. 58, where 1700 is the design traffic volume in $vehicle/hr/ln$, F_{HV} is the adjustment factor for the presence of heavy vehicles. The approaching hourly volume can be estimated based on the $AADT$ and other factors such as the hourly factor *K,* directional split *D,* number of lanes N, and peak hour factor PHF as shown in Eq. 59. More details about the calculation of hourly volume *HV* can be found in the highway capacity manual TRB (2000).

$$C = 1700\ vehicle/hr/ln\ F_{HV} \quad (58)$$

$$HV = \frac{AADT\ D\ K}{F_{HV}\ N\ PHF} \quad (59)$$

Finally, the estimated traffic delay cost is calculated according to Eq. 60, where D is the delay in time per vehicle, and T is the project duration, respectively. V_{user} is the users' time value, which is assumed to be the additional cost paid by the motorist because of work zone activities.

$$C_{delay} = D\ T\ (HV\ Truck\%\ V_{user_{Truck}}\ AOV_{Truck} + HV\ (100 - Truck\%)\ V_{user_{Cars\ \&\ Buses}} AOV_{Cars\ \&Buses}) \quad (60)$$

For simplicity of application, the users' time value is assumed to be their minimum wage at the state where the road is located.

3.3.2.4. Vehicle Operating Cost

This cost represents the additional expenses paid by the driver as a result of operating his/her vehicle for additional time and distance. According to FHWA (2011) and Matthews et al. (2015), the additional operating cost of a vehicle approaching a working zone is attributed to either an increase in the traveling time due to speed reduction in the working zone, complete stop, stop and go driving in the queue, or increasing in the traveling distance when taking a detour. The operating cost of a vehicle depends on five main components including fuel and oil consumption, tire wear, maintenance and repair, and depreciated values (FHWA 2000). The cost of each component is calculated with relevant adjustment and are summed for each vehicle type. In this research, a detailed cost calculation is out of scope and unnecessary since the operating costs of designated vehicles are already available. Therefore, the operating cost calculated for the year 2004 for middle-size vehicles and trucks OCA_{Car} & OCA_{Truck} are adopted and converted to the present values by multiplying it with the ratio of consumer price index (CPI) at the current year when the costs are estimated as shown in **Table 7**. Respective values of CPIs can be found in USDOT & BTS (2022), which are equal to 133.3 and 205.9, respectively. It is important to note that the adopted operating cost values are estimated considering speed variabilities, which are suitable for all potential scenarios in the working zone. Eq. 61 represents the additional operating cost imposed on the traffic volume due to delays associated with working zone activities, which technically depends on the scenarios discussed previously. S_n and S_r are the normal speed and the reduced speed caused by queue or speed restriction in the working zone, respectively. In case of detour

(i.e., scenario III), the $D\ (S_n - S_r)$ is replaced with $(detour\ length - work\ zone\ length)$ assuming same speed.

$$C_{operat} = D\ (S_n - S_r)\ (HV\ Truck\%\ OCA_{Truck} + HV\ (100 - Truck\%)\ OCA_{Car})T \quad (61)$$

To have a probabilistic estimation of indirect cost, Monte-Carlo simulation can be applied to all costs and summed up to obtain the total indirect cost. It is expected that the mean of generated samples (i.e., total indirect cost) will follow a normal distribution with mean μ_{Ind} and standard deviation of σ_{Ind}. Finally, the probabilistic prediction of the total cost can be obtained using Eq. 62 assuming mutual independence between the two consequences categories. The independence assumption has been taken for simplicity and because the indirect cost models impact factors are not related to the impact factors of the direct cost models as shown in **Fig. 11**.

$$f(consequnces/\boldsymbol{IF}) = \frac{1}{2\pi\ (\sigma_{Ind}+\sigma_{Dir})} e^{-\frac{1}{2}\left(\frac{Cost(\boldsymbol{IF})-(\mu_{Dir}+\mu_{Ind})}{(\sigma_{Ind}+\sigma_{Dir})}\right)} \quad (62)$$

Table 7.Vehicle operating cost at different speed levels in 2022-dollar value.

Speed (mph)	Passenger Car ($\$/veh\ mile$)	Truck ($\$/veh\ mile$)
5	\$0.099	\$0.64
10	\$0.221	\$1.23
15	\$0.370	\$2.00
20	\$0.541	\$2.89
25	\$0.763	\$3.92
30	\$1.032	\$5.12
40	\$1.616	\$7.91
50	\$2.341	\$11.22
60	\$2.71	\$15.03
70	\$3.43	\$19.34

3.4. Risk Assessment

After estimating both the likelihood and consequences of failure, the next step is to develop quantitative and qualitative measures that integrate these parameters to aid in the decision-making process. This integration should give a risk measure that reflects the potential losses induced on surrounding properties and communities. Quantitative or qualitative measures reflect the expected outcomes of any risk model and depend on the nature of the input, the output, and the algorithm used to infer risk. As observed in **Section 2.3**, There are three main approaches to evaluate risk: parameter multiplication, risk matrix, and the FIS with different outcome natures (i.e., qualitative, or quantitative). The goals of this study in the field of risk assessment are first to develop a new risk assessment framework called neuro-fuzzy system, which gives qualitative and quantitative risk measures, and it is based on the third approach. The second goal is to discuss the difference between the first two approaches and the new model through a case study. The following subsections will elaborate on the application of the first two approaches and the development of the new model, its training stages, and its application in risk assessment.

3.4.1. Parameters Multiplications

In this approach, risk is defined as the multiplication of likelihood and consequences as shown in Eq. 63. This approach is considered as the basic definition of risk and has quantitative output expressed as expected loss.

$$Risk\ (t) = P(t)\ Consequnces \tag{63}$$

In this model, the expected loss (i.e., Risk) is directly proportional to the likelihood; it approaches its maximum value when the likelihood becomes closer to one. However, in structural reliability practice, a structure is considered completely out of service or failed when the likelihood value approaches a threshold level P_{limit}, which designates different reliability thresholds for service and ultimate levels. Therefore, in this study, the likelihood $P(t)$, is investigated up to P_{limit} and scaled by its corresponding P_{limit} to redefine serviceability loss or failure based on reliability thresholds.

This model is sufficient to prioritize rehabilitation or replacement of sewer pipes by comparing risk values at the time of investigation, t, and assigning higher priority to the pipe having higher expected loss or risk compared to others. However, the expected loss or risk can be converted to a risk index by dividing the consequences by an external parameter as shown in Eq. 64, for example, the total budget. Each agency has different resources or funds that are directly allocated to these structures; therefore, scaling the risk dollar value by the allowable funds or resources will give a much clearer vision of the criticality of the structures. The range of risk index is restrained between zero and one as shown in Eq. 64, which means that at the failure time or the end of the service life, the consequences will be equal to the budget.

$$Risk_{index}\ (t) = \frac{P(t)}{P_{limit}}\ \frac{Consequnces}{Budget}\ \{Risk_{index}\ \in \mathbb{R} | 0 \leq Risk_{index}\ < 1\} \tag{64}$$

3.4.2. Risk Matrix

Compared to the previous model, this model is qualitative. It starts by categorizing both likelihood, consequence, and risk into different classes. However, instead of inferring risk value directly through multiplications as shown in Eqs. 63 & 64 (which in this case is impossible since parameters are expressed verbally), both parameters are mapped into the risk domain through a set of rules in the form "If antecedent Then consequent". The antecedent part of this rule represents the logical interaction "AND" between likelihood and consequences parameters, while the consequent part represents the risk value. In this study, a risk matrix used previously in assessing the risk of sewer pipe failure by Salman and Salem (2012) will be adopted shown in **Fig. 13**.

Likelihood \ Consequences	Low (0-0.2)	Low-moderate (0.2-0.4)	Moderate (0.4-0.6)	High (0.6-0.8)	Very High (>0.8)
Low (0-0.2)	Low	Low-Moderate	Low-Moderate	Moderate	Moderate
Low-Moderate (0.2-0.4)	Low	Low-Moderate	Moderate	Moderate	High
Moderate (0.4-0.6)	Low-Moderate	Low-Moderate	Moderate	High	High
High (0.6-0.8)	Low-Moderate	Moderate	Moderate	High	Very High
Very-high (0.8-1)	Moderate	Moderate	High	High	Very High

Fig. 13. Risk matrix used in qualitative assessment of sewer pipes (Salman and Salem 2012).

This matrix contains five different categories for each likelihood, consequence, and risk, which each reflects different levels of severity. To put this matrix in practice, the likelihood $P(t)$, scaled by P_{limit} at any time t, is assigned to the proper class based on its value. The consequences are defined as a random variable. The first step is to scale its distribution by the allocated budget

as in Eq. 64, then divide the distribution domain as shown in **Fig. 14**, where CR is the ratio of the consequences (Total cost) to the budget. Finally, the consequences class to be used in the risk matrix is the one that gives the highest probability over its range as shown in Eqs. 65 & 66, where F is the cumulative distribution function of the CR, lb_i and ub_i are the lower and upper bounds of the i^{th} consequences class, respectively, while $consequences_{\ class}$ is the consequences class that corresponds to the highest probability P_{CR_i}.

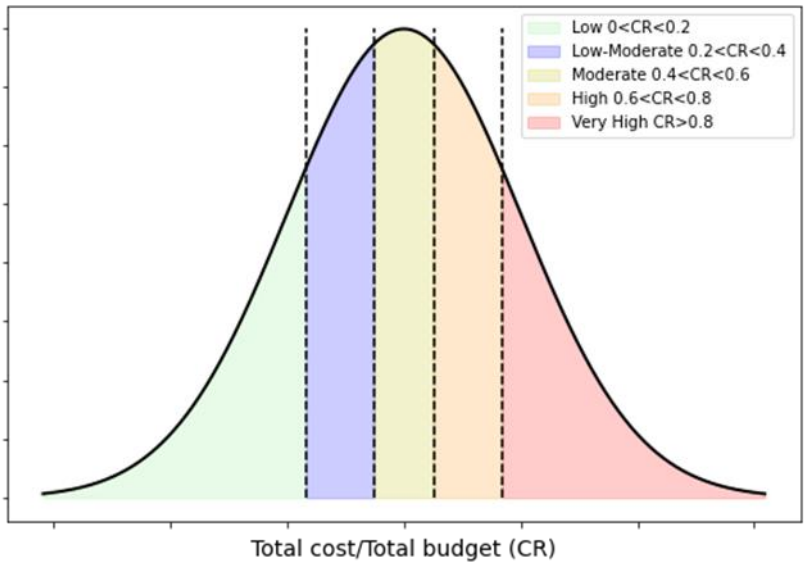

Fig. 14. Risk matrix used in qualitative assessment of sewer pipes.

$$P_{CR_i} = F(lb_i < CR < ub_i) \tag{65}$$

$$consequences_{\ class} = argmax(P_{CR_i}) \tag{66}$$

3.4.3. Neuro-fuzzy system

According to the reviewed literature in **Section 2.3**, fuzzy inference system (FIS) or fuzzy principles has been successfully used in many risk assessment practices. This system was originally developed by Mamdani & Assilan (1975), which allows transitions from the absolute

truth found in classical logic to the partial truth characterized by subjectivity (Siddique 2013). In classical logic, a structure can be considered based on analysis as either failed or not failed, which can be interpreted binarily (1 for failed and 0 for not failed) as well; however, if the same structure lost 70% of its capacity, the absolute truth is not a good representation because the structure is about to fail (1), but it is still being classified as not failed (0). Hence, it is more convenient to interpret the condition of the structure using the partial truth, which in this situation can take a value in the [0,1] range for example, 0.7 to allow for the approximate conclusion. A typical FIS system application is shown in **Fig. 15**. The FIS consists of three different operations as shown starting from mapping the inputs from their crisp value into fuzzy sets represented by membership functions (i.e., fuzzification) and ending up with mapping the outputs fuzzy sets back to crisp value (i.e., defuzzification) after being subjected to the inference mechanism.

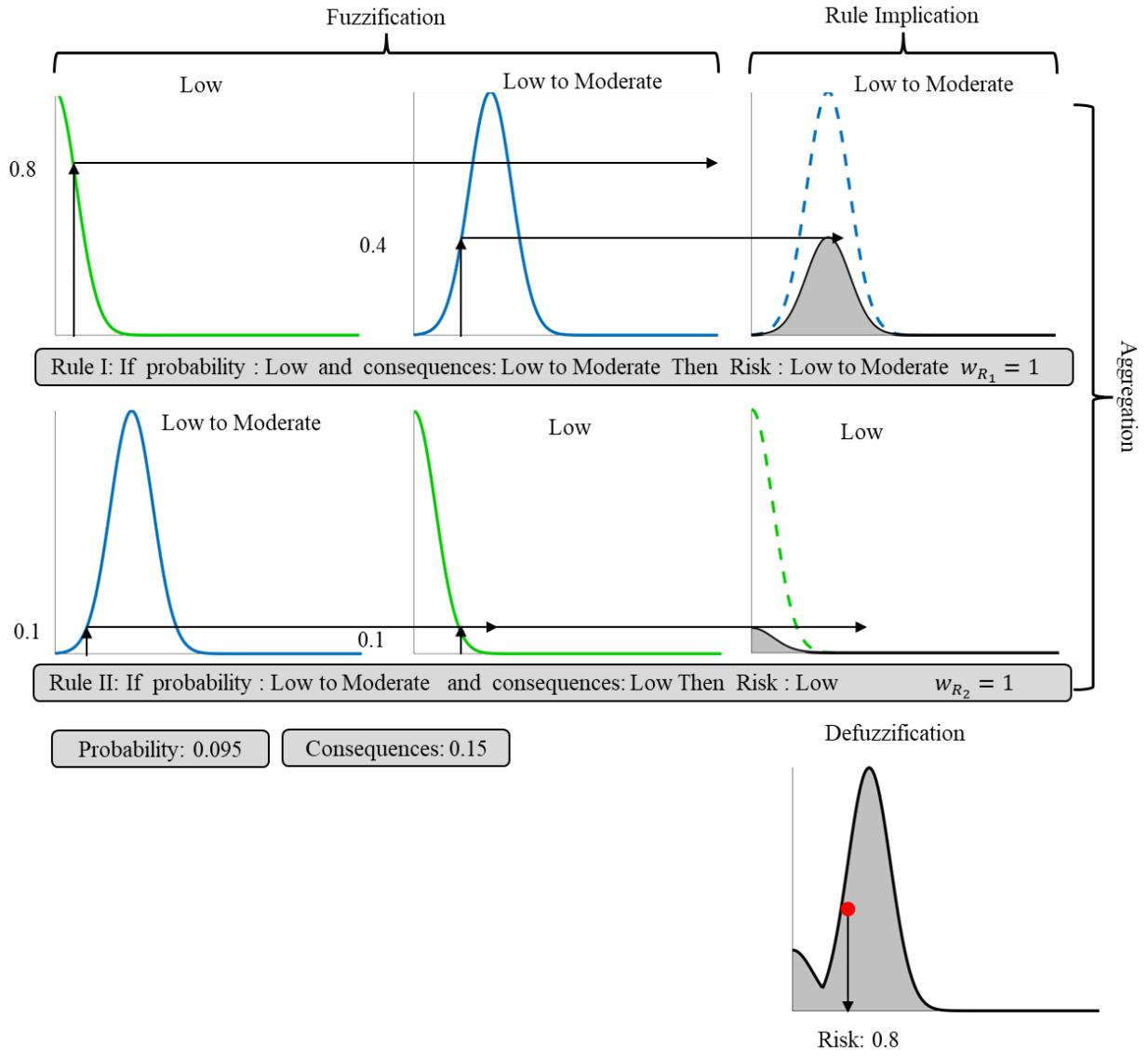

Fig. 15. Mamdani fuzzy inference engine with three rules used to evaluate the risk of failure.

The inference mechanism is the process, in which the input fuzzy sets are nonlinearly mapped from the input space to the output space using logical operators, the knowledge base in the form of a set of if-then rules (Zadeh 1968), and two consecutive processes; rules implication and aggregations. The knowledge base can be acquired from a decision matrix similar to the one shown in **Fig.14.** Finally, the result of rules aggregation is converted back to a crisp value using a defuzzification operation. In practice, there are three different inference mechanisms: Mamdani,

Sugano, and Tsukamoto (Mamdani & Assilan 1975; Sugeno 1985). Despite the computational burdens in the Mamdani inference mechanism, it is preferred in decision-making applications since it provides a better interpretation of the knowledge base and expresses the outputs in terms of membership functions, which is not available in both Sugano and Tsukamoto mechanisms (Kaur & Kaur 2012).

A major disadvantage of the FIS application is that it is not flexible or trainable. When applied in a certain field, the knowledge base, and other parameters such as membership functions are defined heuristically by decision-makers, which reflects their desired thresholds and prospectives. However, the knowledge base and parameters may change over time based on some constraints, changes in decision-makers opinions, or changes in prioritization policies such as the addition of extra fuzzy sets to the input fuzzy space, removing specific rules from the knowledge base, or adjusting weights (i.e., confidence level) of specific rules. All these potential changes make the original FIS inefficient as parts of its essential components are altered. Integrating a supervised machine learning algorithm will compensate for the drawback of the FIS and provide more flexibility to it. In this study, a neuro-fuzzy system will be configured to enhance the state of practice of FIS in risk assessment. Generally, there are three main configurations of combining neural networks with FIS: cooperative, concurrent, integrated, or non-cooperative (Abraham 2005). In this study, the integrated configuration will be used since it allows updating and performing the FIS within the same model making the application more practical. In this configuration, the FIS is presented in the form of a neural network that has a predefined structure. Similar to a conventional neural network, the neuro-fuzzy system consists of a set of layers, in which each node and layer carries different parameters and operations in the FIS system. In this study, a suggested structure of a neuro-fuzzy system is shown in **Fig. 16**. To train this system two

training phases are required; the first one is the structural learning phase, which aims to define the number of nodes in each layer and their activation function, while the second one is supervised learning phase, which aims to obtain the optimal FIS parameters using optimization algorithms.

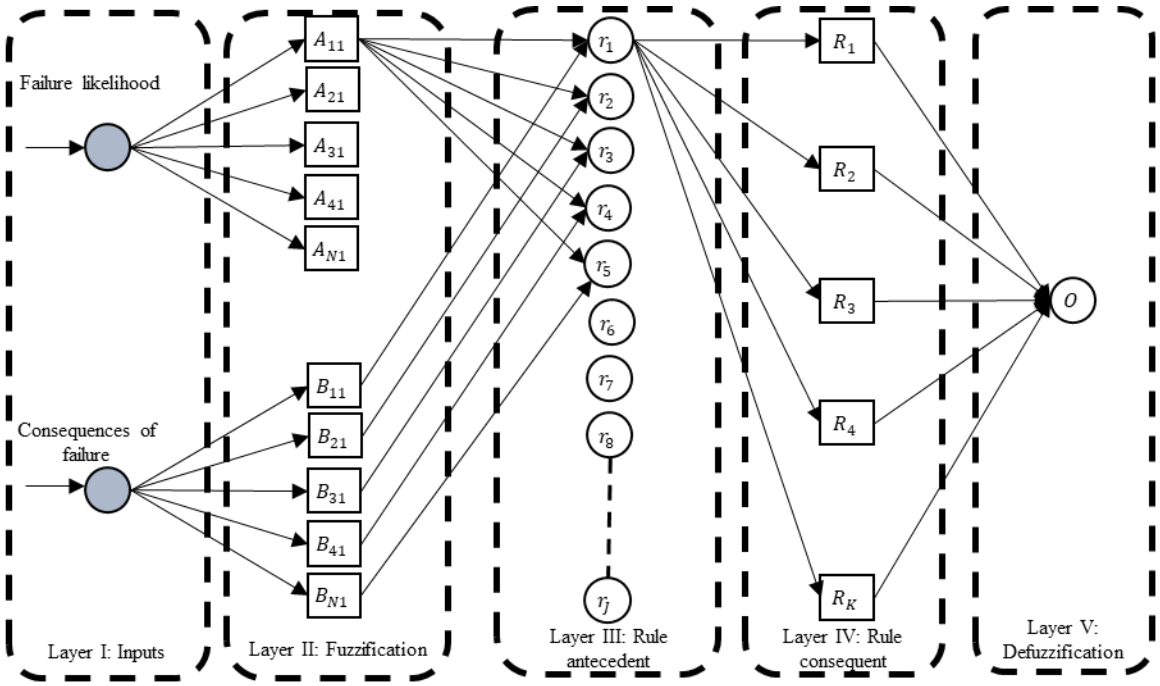

Fig. 16. Example of integrated neuro-fuzzy model for risk assessment.

3.4.3.1. Structural Learning Phase

Before discussing the optimization algorithm and its alternatives to be used in learning the optimal parameters of any FIS system, the goal of this phase is to define or construct essential parameters in any FIS system including input and their fuzzy sets and corresponding activation functions in addition to the outputs as reflected in the neuro-fuzzy system. This section will discuss in detail the role of each layer and corresponding nodes in the proposed system.

Layer I: this layer is the input layer with several neurons P equal to the number of inputs, which are in this case the likelihood and the consequences.

Layer II: this layer represents an essential operation in the FIS system, which is fuzzification. The total number of neurons is PN, where N is the number of neurons connected to either input, which represents its corresponding fuzzy sets. As observed in **Fig.16**, this is a partially connected layer since each input in the preceding layer is connected to its corresponding fuzzy sets only. The weights matrix in this layer $\boldsymbol{w_{21}}$ and has a size of $(P \times N)$ with a unit value where connections exist and zero elsewhere. This layer is responsible for mapping the discrete inputs ${y_p}^1$ to their fuzzy set through a distinct membership function designated for each neuron. The typical shape of these functions is a Gaussian as shown in Eq. 67, where ${y_{pn}}^2$ is the output of the n^{th} fuzzy set corresponding to the P^{th} feature, and a and b are the mean and standard deviation, respectively. Other shapes can be assumed such as trapezoidal and triangular; however, this shape simplifies the optimization process since it is continuously differentiable.

$$ {y_{pn}}^2 = e^{-\left(\frac{\left(a-{y_p}^1\right)^2}{2b^2}\right)} \tag{67} $$

Layer III: the total number of nodes in this layer J equals the anticipated number of rules in the knowledge base. By default, the anticipated number of rules is equal to the number of fuzzy set combinations from the previous layer N^P. This layer is also partially connected as shown in **Fig. 16**, where each node is connected only to two fuzzy sets: one from each feature P. $\boldsymbol{w_{32}}$ have a size of $(N^2 \times NP)$. Each row resembles a rule, where the weight values are set to one at indices correspondence to the fuzzy sets located in the antecedent part of the j^{th} node (i.e., two fuzzy sets for each rule) and zeros elsewhere. This layer is responsible for performing the logical operation of the antecedent part of each rule (i.e., node). Therefore, the activation function for all nodes in this layer is the logical operation "AND", which can be interpreted as shown in Eq. 68. ${y_j}^3$ is the

j^{th} node output from the third layer and $\boldsymbol{l_j}$ is the set of nodes (i.e., fuzzy sets) in the second layers that are connected to the j^{th}node (i.e., rule) in the third layer.

$$y_j{}^3 = min(y_{1n}{}^2, y_{2n}{}^2) \ \forall\, n \in \boldsymbol{l_j} \tag{68}$$

Layer IV: this layer represents the fuzzy sets of the output, which is a risk. The number of neurons K equals the number of fuzzy sets designated to the output. This layer implicates the outcomes of *Layer III* on the default consequent parts and then aggregates the results across the entire rules set. Initially, it is assumed that this layer is fully connected with the weight matrix $\boldsymbol{w_{43}}$ of the size of $(K \times N^2)$, which means that there will be conflicting rules; however, once the knowledge base is learned in the supervised learning phase, conflicting rules will be eliminated (i.e., assigned zero values to their weights) and only left with informative rules with weights values ranging from 0 to 1. The learned values represent the firing strength or the confidence level of these rules. The knowledge base learning process depends on other FIS parameters learned during the supervised learning phase; therefore, the knowledge base or the rules weights are updated after each supervised learning step. It is also possible to allow these weights to be fixed by decision-makers according to their preferences. The implication and aggregation of rules can be obtained by applying Eq. 69, where $y_k{}^4$ is the output of the k^{th} node, w_{kj}^2 is the square of weight of the j^{th}rule connected to the k^{th} output fuzzy set, and l_k is the set of nodes (i.e., rules) in the third layer that are connected to the k^{th}node in this layer.

$$y_k{}^4 = max_{j \in l_k}(w_{kj}^2 y_j{}^3) \tag{69}$$

Layer V: Similar to conventional neural network, the last layer is the output layer. This output of this layer represents the outcome of defuzzification process discussed in previously in the application of FIS. Since the target output is risk, the number of neurons in this layer is only one with activation function set as centre of area method. The weights connected to this layer are all set to one. Because of the complexity of the final shape generated from prior actions, an approximation suggested by Kim and Kasabov (1999) will be used, as shown in Eq. 70, where d_k & c_k are the mean and the standard deviation of the output's Gaussian membership functions.

$$y_l{}^5 = \frac{\sum_{k=1}^{K} y_k{}^4 d_k\, c_k}{\sum_{k=1}^{K} y_k{}^4 d_k} \tag{70}$$

3.4.3.2. Supervised Learning Phase

The power of machine learning and supervised learning techniques in adopting and learning patterns found in a dataset will be utilized to learn the optimal parameters of the FIS system. These parameters include membership functions parameters for both inputs and outputs, in addition to the knowledge base or rules defined by their weights $\boldsymbol{w_{43}}$. A list of trainable parameters is summarized in **Table. 8**.

Generally, the learning stages in the proposed model are divided into two main parts. The first one is related to the parameter learning stage, in which backpropagation optimization is used to track the error path and find the optimal membership function within the parameters space that gives the least possible error. The second one is the knowledge acquisition stage and depends on the first stage, and it is used to learn the weights of the default rule set $\boldsymbol{w_{43}}$.

Table 8. List of trainable and nontrainable parameters in each layer.

Parameters	Description	Trainable or Not Trainable
$\boldsymbol{w_{21}}$	Weights connecting the first layer to the second layer	Not Trainable
$\boldsymbol{a_{pn}}$ & $\boldsymbol{b_{pn}}$	Inputs memberships function parameters	Trainable
$\boldsymbol{w_{32}}$	Weights connecting the second layer to the third layer	Not Trainable
$\boldsymbol{w_{43}}$	Weights connecting the third layer to the fourth layer, are rules' firing strength	Trainable
$\boldsymbol{c_{kl}}$ & $\boldsymbol{d_{kl}}$	outputs memberships function parameters	Trainable

3.4.3.2.1. Parameters Learning Stage

Using available datasets, this model can be trained using a backpropagation algorithm. The goal of the backpropagation algorithm is to obtain the optimal parameters that minimize the objective functions. A typical objective function is the mean square error shown in Eq. 71, where n is the size of the dataset used to train the model and ${y_i}^5$ and y_i are the expected and true responses. Different optimization alternatives can be adopted to conduct this stage and will be discussed later. These alternatives vary in their efficiency; however, the trend or the frequency of updating the parameters according to Eq. 72 is the same for all of them. The frequency or the trend depends mainly on the size of the dataset used to train the model and generally, there are three main trends. The first one is the full batch, which allows the utilization of the entire dataset to update the parameters per training iteration or epoch. The second one is mini batch, in which parameters get updated n times per training epoch using the n^{th} subset of datasets. The final approach is the online batch. It is the same as the mini batch but with the n equal to the length of

the dataset. This means that the parameters are updated after each data point per epoch. In this study, the mini-batch approach will be used as it provides a balance between the bias and the variance in the training process.

$$E_{batch} = 1/n \sum_{i=1}^{n} ({y_i}^5 - y_i)^2 \tag{71}$$

$$\boldsymbol{w_t = w_{t-1} - stepsize} \tag{72}$$

This objective function was adopted in many applications of the neuro-fuzzy system (Kothamasu & Huang 2007; Shoaib et al. 2016; Navarro-Almanza et al. 2022); however, this function does not guarantee satisfaction one of the main properties found in the neuro-fuzzy system. The fuzzy system demands that at any point within the fuzzy domain of either inputs or outputs, the summation of membership functions of fuzzy sets should converge to one. To integrate this constraint within the objective function, equality constraints are added to the objective function according to Lagrange theory (Duc et al. 2006) as shown in Eq. 73. For risk application, there are three constraints are added: one for each input (i.e., likelihood and consequences) and one for the output (i.e., risk).

$$E_{batch} = 1/n \sum_{i=1}^{n} \left[({y_i}^5 - y_i)^2 + \sum_{j=1}^{3} \lambda_j \left(1 - \sum_{k=1}^{s} {\mu_k}_i\right)^2 \right] \tag{73}$$

The mean square error in Eq. 73 is only valid for continuous output, which may not always be the case in risk applications. As discussed in **Section 3.4.1 and 3.4.2**, risk can be interpreted numerically as a continuous random variable or qualitatively to reflect the expected loss. However, the first approach does not depend on decision rules to infer risk. Since the goal of the FIS is to mimic human behavior, which is based on a set of rules, while avoiding overstatement or understatement in the qualitative interpretation of risk, the neuro-fuzzy will be trained on data that follow certain rule patterns and with risk-interpreted in ordinal scale that reflects the qualitative classes of risk. Accordingly, the objective function in Eq. 73 is modified as shown in Eq. 74.

$$E_{batch} = 1/n\, sum_{i\in n}\left[\left\{\begin{matrix} 0 & {y^5}_i \in R_j \wedge\ y_i \in R_k, j = k \\ \left(upper\ bound_{R_j} - {y^5}_i\right)^2 & {y^5}_i \in R_j \wedge\ y_i \in R_k, j > k \\ \left(lower\ bound_{R_k} - {y^5}_i\right)^2 & {y^5}_i \in R_j \wedge\ y_i \in R_k, j < k \end{matrix}\right\} + \sum_{j=1}^{3} \lambda_j \left(1 - \sum_{k=1}^{s} \mu_{k\,i}\right)^2\right] \quad (74)$$

The first part of the objective function in Eq. 74 is a piecewise function. This part should give zero when the model prediction ${y^5}_i$, belong to the same risk class as the true value y_i ,(i.e., the ordinal value representing the designated class). If ${y^5}_i$ belongs to a higher risk level (i.e., $R_j > R_k$) than the true value or the opposite (i.e., $R_j < R_k$), then ${y^5}_i$ is subtracted from the $upper\ bound_{R_j}$ of R_j or the lower bound of R_k, respectively. Finally, the function is averaged out across the entire dataset within a batch including the added equality constrained. The error on the epoch level is simply the average error on a batch level as shown in Eq. 75.

$$E_{epoch} = 1/\#batch\ \sum_{i}^{\#batch} E_{batch_i} \quad (75)$$

After defining the objective function, the next step is to select a suitable backpropagation optimization algorithm. Indeed, stochastic gradient descent (SGD) is the most used in neuro-fuzzy applications in previous studies. The goal of this study is to try more advanced optimization algorithms that could potentially boost the training performance and reduce the required number of training epochs to minimize the objective function. The algorithms that will be considered in this study are summarized in **Table. 9**. Finally, recommendations about the best algorithm will be given based on the number of epochs required for E_{epoch} to reach a specific error threshold, which is assumed to be 0.0005. This threshold has been chosen after conducting such training

experiments after which it is found the error would stabilize around it making further reduction very slow.

Table 9. Summary of optimization algorithms used in training the model.

Optimization algorithm	Description	Reference
Adam	It stands for adaptive moment estimation; it updates the first moment (mean) and the second moment (uncentered variance) of the gradients exponentially using the decaying moving average of the first and second moments. It is best suited when having sparse, noisy gradients, or large parameters.	(Kingma & Ba 2014)
Gradient descent with momentum (momentum)	This algorithm uses the concept of momentum to expedite the convergence. The amount of parameter change depends on the current gradient, the most recent change, and the momentum coefficient. 0.9 is the typical momentum coefficient value.	(Qian 1999)
Nesterov accelerated gradient. (NAG)	It has a similar concept to the Gradient descent with momentum, but instead of evaluating the gradient using the previous step parameters, it evaluates the gradients using the look-ahead value. This will minimize the overshooting pitfall in the Gradient descent with momentum.	(Nesterov 1983)
Adagrad	This algorithm updates the parameters based on the summation of the squared gradients for all previous steps and works perfectly with sparse gradients. The step size for each parameter is the learning rate divided by the square root of the summation of the gradients added to an error tolerance. One major drawback of this algorithm is that the step size for each parameter is continuously decreasing over time.	(Duchi et al 2011)
Adelta	This algorithm is an enhancement of Adagrad. It was developed mainly to reduce the aggressive reduction in the step size in the Adagrade algorithm by taking the decaying average of all past gradients instead of their summation.	(Zeiler 2012)

3.4.3.2.2. Knowledge base learning stage

The purpose of this stage is to learn the corresponding weights $\boldsymbol{w_{43}}$, of rules in the knowledge base that truly reflect the data, which resemble decision-makers beliefs. To do so, the approach proposed by Wang and Mendel (1992) as displayed in **Fig. 17** will be adopted. This approach depends on other parameters of the FIS system including fuzzy sets numbers and interval and membership functions; therefore, this learning stage is applied after each parameter updates in the parameters learning stage and used in the subsequent iteration. In **Fig. 17**, the first step is to pass all training datasets of length m into the predefined J rules, evaluate the membership functions of the fuzzy sets in the antecedent and consequent parts within rules, and take their products. This should result in a matrix $\boldsymbol{w}$ of size $(m \times J)$, which will be filtered in the subsequent steps. In the next step, for each instant (i.e., each row of matrix $\boldsymbol{w}$), the highest weight and corresponding rule are selected and added to matrix $\boldsymbol{M}$ of size $(2 \times m)$. In this matrix, there is a potential for duplicated rules, but with different weights; therefore, similar rules are isolated in separate submatrices $\boldsymbol{K_r}$. Finally, the highest weight in each of the submatrices $\boldsymbol{K_r}$ is taken and added with its corresponding rule to matrix $\boldsymbol{L}$ of size $(2 \times R)$. R is the true number of rules in the knowledge base, which can be equal to or less than the default number of rules J. This process will inherit the rules that most reflect the pattern found in data along with their firing strengths or weights, which resemble the confidence level.

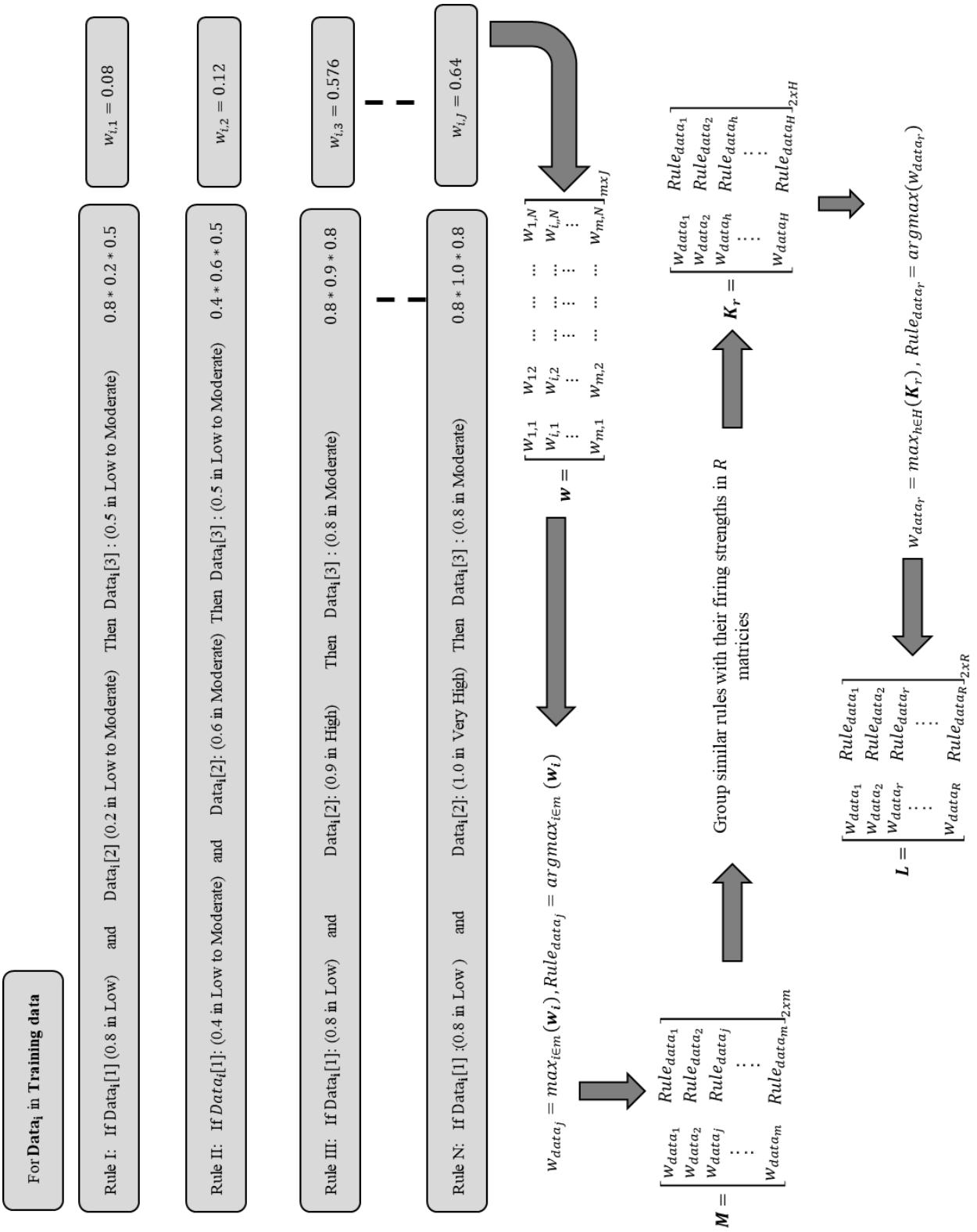

Fig. 17. Evaluation approach of rules firing strengths.

3.4.3.3. Application in Risk Assessment

This section aims to orient the scope of this model on risk assessment and suggest a framework to collect the training data, which will be used to obtain the knowledge base and the true parameters through the training process. In risk assessment practice, the first step is to define the potential threats and failure modes under certain hazards. For example, sewer main are exposed to sulfide (hazard), which potentially induce wall erosion (potential threats) and induce certain failure modes such as reinforcement exposure, flexural failure, etc… The second step is to find the likelihood of occurrence of failure mode and related consequences. As shown in **Section 3.4.2**, risk can be defined qualitatively (e.g., low, moderate, high, and very high) and used later to infer risk. Up to this point, this would be sufficient in the case of using a predefined risk matrix; however, training the neuro-fuzzy system would require a set of training data. **Fig. 18** suggests a framework to gather training data and use it in neuro-fuzzy. It starts by collecting a set of failure observations under certain threats for a particular hazard event, then these observations are passed to decision-makers or engineers who will assign a qualitative class to the risk according to their beliefs for every observation. At this point, the size of the training dataset would be the number of observations times the number of decision-makers. By defining other parameters such as the number of fuzzy sets and fuzzy intervals, the proposed model can be then trained to obtain the firing strengths and the parameter values that best describe the training data. The power of this model is not only in its ability to learn the optimal parameters but also in its ability to adopt future changes in FIS such as reducing the firing strengths or changing the fuzzy intervals. These changes might occur based on risk perception and the attitude of decision-makers.

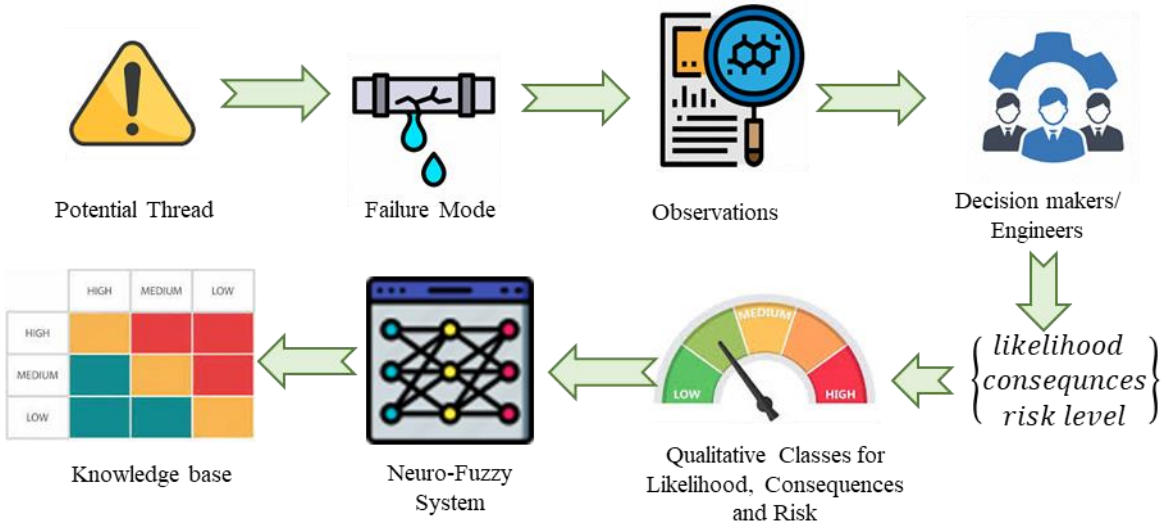

Fig. 18. Proposed application of neuro-fuzzy system for risk assessment.

3.5. Methodology Practice

In previous sections, the likelihood of failure and serviceability loss, consequences of failure, and risk evaluation approaches were introduced. The likelihood and consequence of failure approaches are only intended for RCSPs; however, the proposed risk model applies to any structure under specific threats. Therefore, to put the methodology into practice, the first step is to define hazard events and their potential threats. For both service and ultimate level, the hazard events are chloride and sulfide exposure. These events are going to induce threats on the structures such as wall erosion and reinforcement corrosion which under sustained loading will reduce the serviceability and increase the chance of failure from different perspectives. The next step is to define all sets of input parameters as either random variables or deterministic depending on their availability or ease of measurement. Afterward, a Monte-Carlo simulation is conducted to have an estimate of likelihood at both service and ultimate levels, which defines loss of serviceability or failure whenever exceeding their permissible values. When the interest of decision-makers is to evaluate the risk associated with serviceability, they can refer to the consequences of the failure

approach and mainly to the CIPP alternative and its associated indirect cost to have a probabilistic estimate of the total cost or the consequences; otherwise, they can refer to the replacement alternative as it is more suitable with failure. Finally, the likelihood at any time for a specific level can be integrated with its relevant consequences using either risk approach mentioned above. The entire process is summarised in **Fig. 19** and illustrated in the upcoming case study.

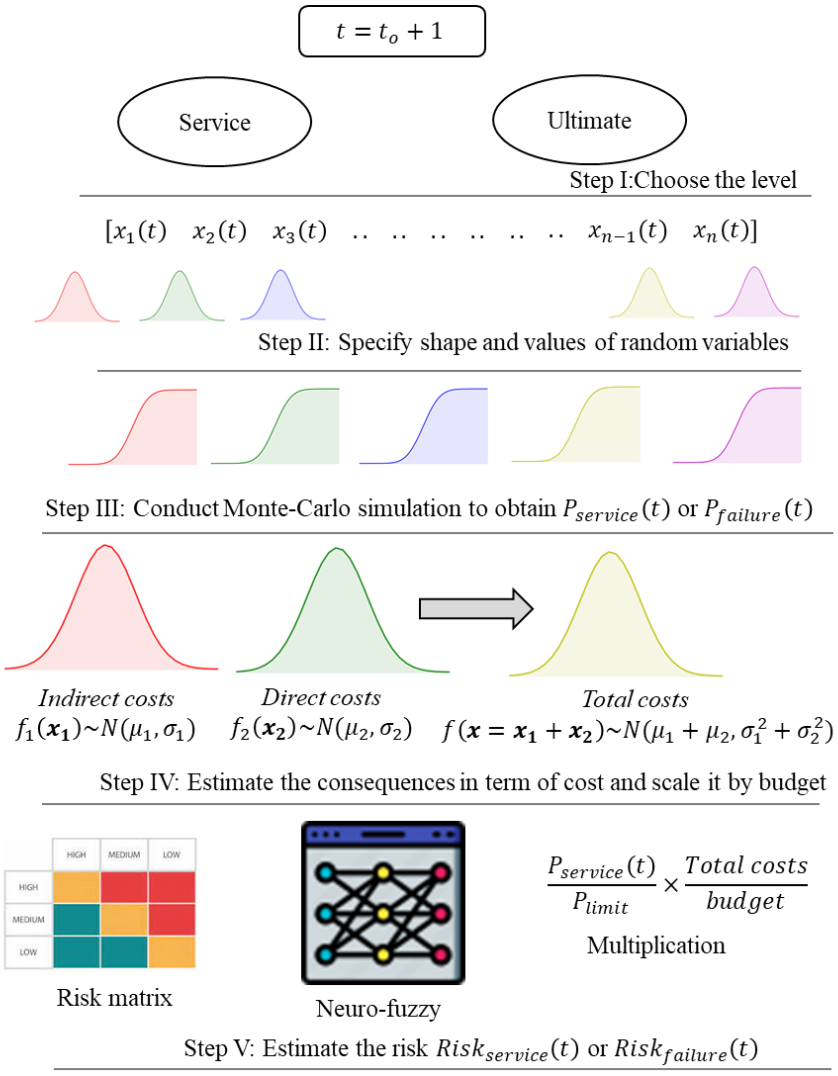

Fig. 19. Procedure to estimate the risk of failure or serviceability loss of RCSPs under sulfide and chloride hazards.

Chapter 4. Case Study

4.1. Overview

This chapter will demonstrate the application of all three risk approaches in addition to the likelihood of failure and serviceability loss and consequences of failure frameworks presented in **Chapter 3** through a case study. In the first section, the reliability of the 42 $inch$ RCSP located in Arlington, Texas at both service and ultimate level will be examined. The outcome of this section is profiles or cumulative probability density functions that show the variation of likelihood at any time during the lifetime of the RCSP. In the next section, a detailed calculation of direct and indirect costs in addition to the total cost of consequences predictive distribution will be obtained for both CIPP and replacement alternatives. In the last section, a detailed risk assessment using all three approaches in addition to the demonstration of training the neuro-fuzzy model including recommendations on the best optimization algorithm, and presenting model adaptability will be provided.

4.2. Reliability Analysis

A 42 $inch$ RCSP located in Arlington, Texas, and installed in 1984 will be investigated for 120 years from the date of installation. This pipe has been under service since then, after inspection, it was found that this pipe exhibits significant deterioration under the effect of sulfide and chloride attack. Therefore, the goal of this section is to investigate the reliability of this pipe considering all limit states or failure modes defined in the **Chapter. 3**. According to **Fig. 19**, to investigate the reliability at both service and ultimate levels, the first step is to define the set of input parameters. Values of these parameters are provided in **Table 10**. These values can be obtained from inventory records, specifications, standards, and previous studies and can

interpreted as either deterministic or random variables. This depends on different factors related to data availability, ease of measurement, and error levels. These parameters can be classified as either weather, environmental, mechanical, or geometrical parameters, which are designated in different colors in **Fig. 9**.

Table 10. Deterministic and stochastic input variable of limit state functions.

Variable	Distribution	Value	References
Class	Deterministic	III	(ASTM C76 2022)
C	Normal	$\mu = 25.4mm, \sigma = 0.1\mu$	
C_r	Deterministic	0.8	(Coronelli 2002)
Cl_{su}	Lognormal	$\mu = 0.65$ %, $\sigma =$ 0.078% of concrete unit weight	(Sulikowski &Kozubal 2016)
Cl_{th}	Lognormal	$\mu = 0.40$ %, $\sigma = 0.09\%$ of concrete unit weight	
D_{cl}	Lognormal	$\mu = 50\, mm^2/year$, $\sigma = 16\ mm^2/year$	
D_{in}	Deterministic	$1219.2\ mm$	(ASTM C76 2022)
EW	Deterministic	$18.62\ g$	
H	Uniform	$Lower\ bound = 1.83m$, $Upper\ bound = 7.1m$,	(ASTM G102 2015) (ACPA 2017)
R	Extreme value	$\mu = 5.41$, $\sigma = 1.16$	(Hingorani et al. 2013)
H_2S	Uniform	$Lower\ bound = 0\ ppm$, $Upper\ bound = 50\ ppm$	(Li et al. 2019)
RH	Normal	$\mu = 80\%$, $\sigma = 8\%$	assumed
R_s	Deterministic	$609.6\ mm$	(ASTM C76 2022)
b_1	Deterministic	$1\ m$	(ASCE 15 2017)
h	Uniform	$Lower\ bound = 10.16\ cm$, $Upper\ bound = 14.1\ cm$	(ASTM C76 2022)
w/c	Uniform	$Lower\ bound = 0.48$, $Upper\ bound = 0.53$	

Table 11. Deterministic and stochastic input variable of limit state functions (continued).

Variable	Distribution	Value	References
w/c	Uniform	$Lower\ bound = 0.48,$ $Upper\ bound = 0.53$	
f_{c0}	Normal	$\mu = 27.6$ Mpa , $\sigma = 2.76$ Mpa	
f_{y0}	uniform	$Lower\ bound = 483\ Mpa,$ $Upper\ bound = 552\ Mpa$	
f_{ct0}	Deterministic	3.3 Mpa	(Den & Uijl 1996)
k_1	Deterministic	$3.27 * 10^{-3} \frac{mm}{g\ \mu A\ cm\ year}$	(ASTM G102 2015)
n	Deterministic	3	(Den & Uijl 1996)
n_{ribs}	Deterministic	1	Assumed
n_{bars}	Deterministic	1	Assumed
r_s	Deterministic	$8mm, 7mm,$ & $5.73mm$	(ASTM C76 2022)
w_{limit}	Deterministic	$0.254\ mm$	(ASTM C76 2022)
w_0	Deterministic	$0.254\ mm$	(Den & Uijl 1996)
α	Uniform	$Lower\ bound = 2.9,$ $Upper\ bound = 3.3$	(Zhou et al 2011)
α_1	Uniform	$Lower\ bound = 0.012,$ $Upper\ bound$ =0.0198	(Imperatore 2022)
α_y	Uniform	$Lower\ bound = 0.012,$ $Upper\ bound$ =0.0547	
ε_{cr}	Deterministic	0.003	(Den & Uijl 1996)
ε_{u0}	Uniform	$Lower\ bound = 0.08,$ $Upper\ bound$ =0.01	(ACI PRC 439.5 2018)
ε_y	Deterministic	0.005	(ASTM C76 2022)
ρ	Deterministic	$7.86\ \frac{g}{cm^3}$	(ASTM C76 2022)
$\beta_{service}, \beta_{ultimate}$	Deterministic	4.7, 2.9	(Holicky 2009)
θ_f	Deterministic	0.95	(ASCE15 2017)
θ_{vp}	Deterministic	0.9	θ_{vp}

Based on **Tables 10 & 11**, The pipe under investigation is a class III pipe designed using the D-Load test method according to ASTM C76 (2022) to sustain maximum load until 0.1 $inch$

(0.254 mm) is observed. The designated pipe class has three different wall types, with different reinforcement, wall thickness, and concrete cover requirements. Since the available inventory records did not specify the wall type, these parameters are assumed as random variables with uniform distribution ranging from the least permissible to the maximum one. Similarly, inventory records did not show any information about the buried depth H; therefore, it is assumed to follow a uniform distribution with limits recommended by ACPA (2017). This allows consideration of variabilities in earth and vehicular loading; hence, in the applied moment M_u, shear V_u, and thrust N_u. mechanical properties of concrete and wire reinforcement were selected based on recommendations found in ASTM C76 (2022), ASTM A1064 (2013), and ACI 439.5R (2018). Environmental factors such as chloride concentration threshold Cl_{th}, chloride concentration at surface Cl_{su}, and chloride diffusion coefficient D_{cl}, sulfide concentration H_2S, are also retrieved from relevant references. Finally, because the analysis depends on the temperature in both Kalvin and Celsius (T_k and T_c) and relative humidity RH, relevant data were retrieved from the (National Weather Service 2022) as shown in in **Fig. 20**. In the time-dependent analysis, the analysis will be conducted on month levels; therefore, the average monthly temperatures from the date of pipe installation until the end of year 2021 will be used. For the remaining 83 years, the average monthly temperatures are randomly predicted within the 25th and 75th quantiles of the previous monthly average data shown in **Fig.20**. RH data are assumed to follow uniform distribution ranging from 80% to 100% percent. Despite the results are provided monthly, they are present on a yearly scale for interpretability.

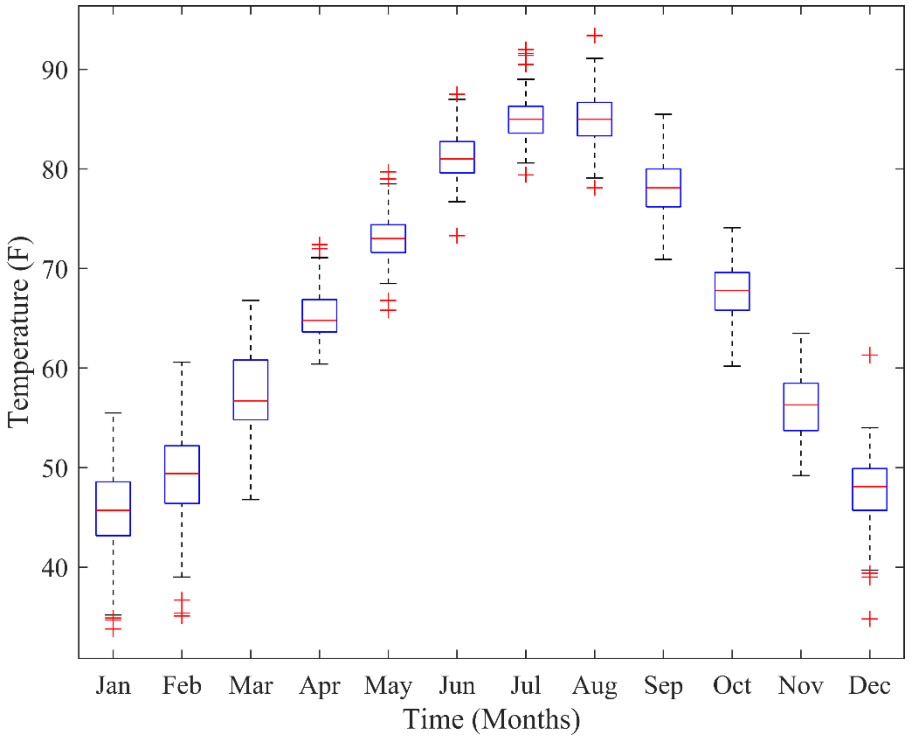

Fig. 20. Average monthly temperature variation from 1986 until 2021 in the Dallas Fort Worth metropolitan area.

The essence of this framework is the Monte-Carlo simulation. In this case study, Monte-Carlo simulation with Latin hypercube sampling technique will be used. The Latin hypercube sample is a very effective sampling technique compared to a random number generator as it ensures equal sampling across the entire domain of sampling. It starts by dividing the domains of random variables into k different intervals, which is, in this case, going to be ten, then n different samples are generated from each interval, which is, in this case, equal to 4000. This makes the total number of samples N equal to $k \times n$ or 40000. This process is conducted only at the beginning, then samples are used to evaluate the likelihood on a monthly base according to Eq. 44.

Before starting the simulation process, it is important to have an estimate of the permissible likelihood values that define serviceability loss $P_{limit_{ser}}$,or failure time $P_{limit_{ult}}$. To do so,

reliability index values for 1 year's investigation period $\beta_{service}$ and $\beta_{ultimate}$ and given in **Table 11** are converted to equivalent likelihoods for a 120-year investigation period according to Eqs. 76, 77, & 78, where F is the cumulative distribution of standard normal distribution. The values of $P_{limit\,ser}$ and $P_{limit_{ult}}$ are 0.1587 and 0.212, respectively.

$$. (\beta_{service})_{120} = F_{normal}((\beta_{service})_{1})^{120} \quad (76)$$

$$. (\beta_{ultimate})_{120} = F_{normal}((\beta_{ultimate})_{1})^{120} \quad (77)$$

$$(P_{limit})_{120} = F^{-1}{}_{normal}(-(B_{limit})_{120}) \quad (78)$$

After generating samples, the next step is to evaluate the initiation of environmental chloride and sulfide hazards following the procedure described in **Sections 3.2.1.1 and 3.2.1.2**. The $t_{in_{Cl}}$ is the time when the likelihood $P(CLS(t) \leq 0)$ exceeds the permissible values $P_{limit\,ser}$, which is in this case 1 year. The $t_{in_{H_2S}}$ is a predictive normal distribution shown in **Fig. 21** with a mean equal to 130 months (i.e., 11 years).

$t_{in_{Cl}}$ and $t_{in_{H_2S}}$ are used to evaluate reliability, hence the likelihood of each failure mode or limit state function at service and ultimate levels. The evaluation process starts at time t equals to $\min(t_{in_{Cl}}, t_{in_{H_2S}})$. **Fig. 22 & 23** show the likelihood variation of different limit states at both service and ultimate levels in addition to the combined likelihoods at both levels estimated using reliability block diagrams explained in **Section 3.2.3**. These likelihoods can be used to estimate the end of service life or the lifetime of RCSPs from different prospectives as shown in **Table 12**. For example, if decision-makers are only interested in observing cracks, then the likelihood of observing cracks can be compared with $P_{limit\,ser}$ to estimate the service life; however, if decision-makers are interested in all limit states, then they can use the combined likelihood.

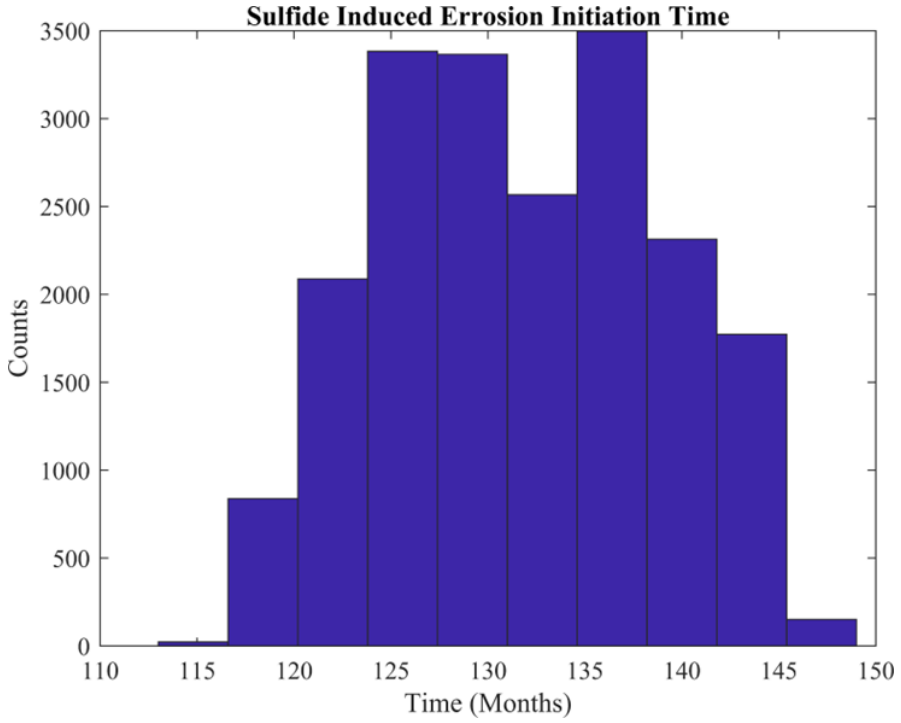

Fig. 21. Predictive distribution of sulfide attack initiation time.

Table 12. Expected time of serviceability loss and time of failure based on limit state functions or their combinations.

Limit state function	t_{ser} $(years)$	t_{fail} $(years)$	$P_{lim_{serv}} = 0.1587,$ $P_{lim_{ult}} = 0.2121,$
$CWLS$	16	-	
$BSLLS$	9	-	
$WTLLS$	31	-	
$system\ serviceability$	40	-	
$FLLS$	-	54	
$SLLS$	-	61	
$RTLLS$	-	107	
$DLLS$	-	66	
$system\ failure$	-	36	

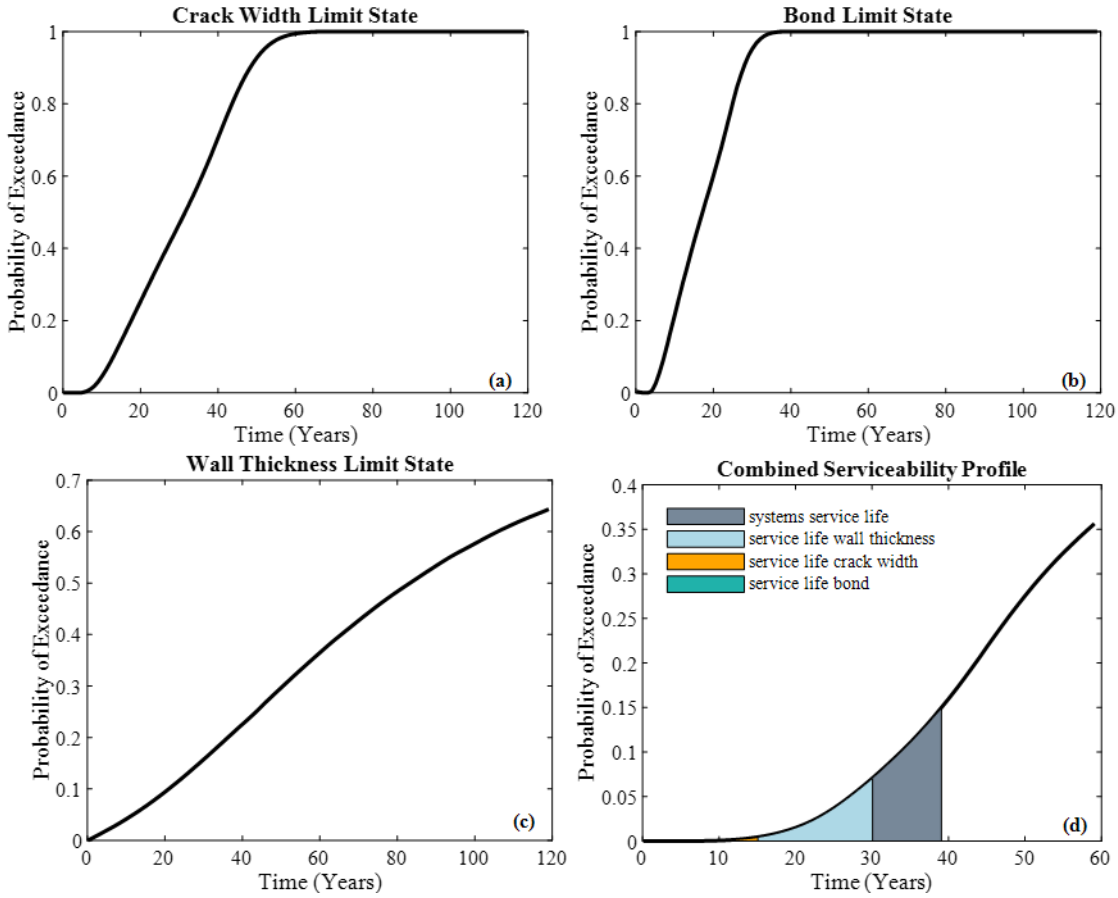

Fig. 22. **(a)** Likelihood of observing crack width more than 0.254 mm. **(b)** Likelihood of losing bond strength. **(c)** Likelihood of losing wall thickness cover. **(d)** System's likelihood profile at service.

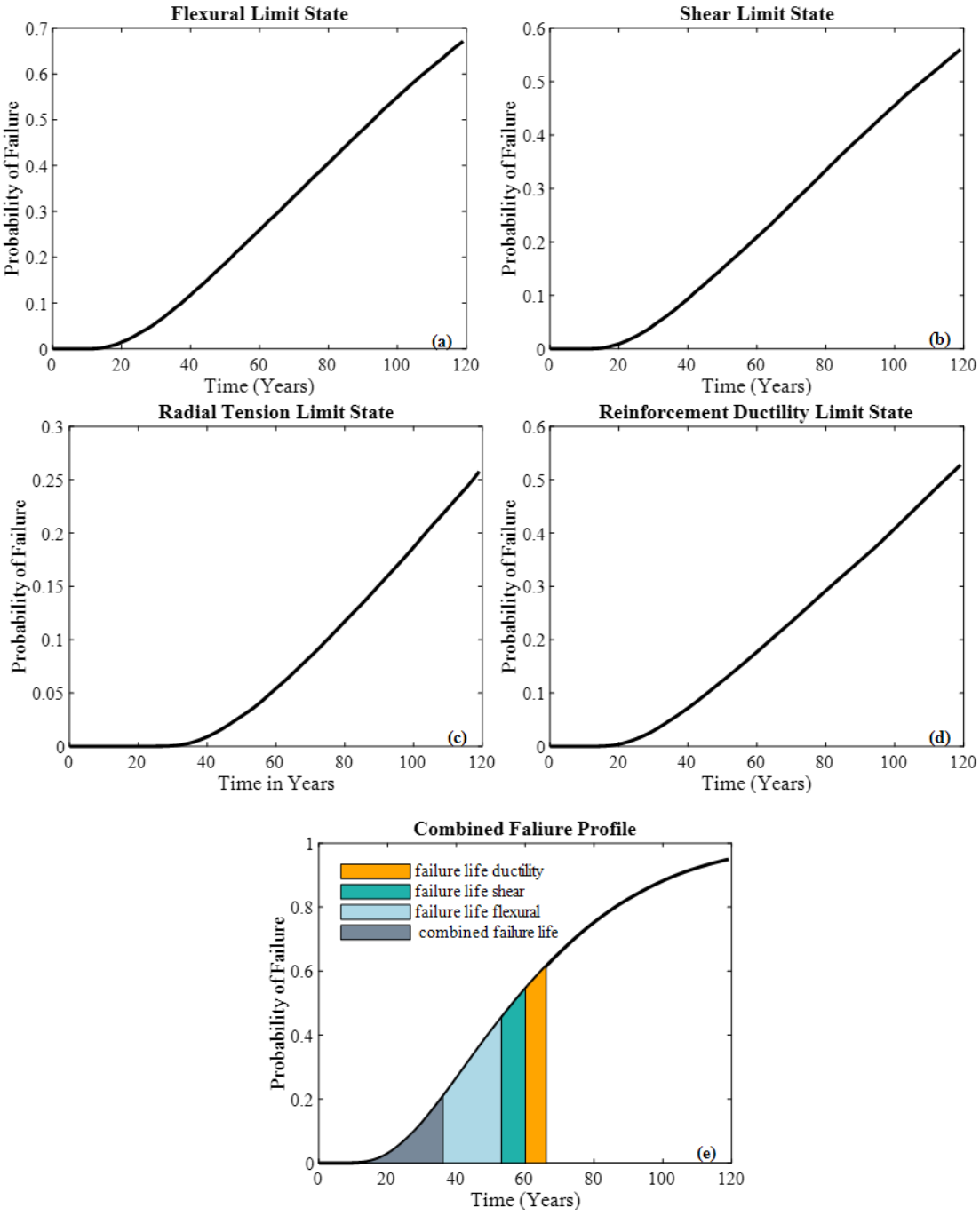

Fig. 23. (a) Likelihood of flexural failure at the crown; **(b)** Likelihood of shear failure at critical; **(c)** Likelihood of radial tension failure; **(d)** Likelihood of reinforcements ductility Loss **(e)** System Likelihood profile at ultimate.

4.3. Consequences of Failure

Whether evaluating reliability at service or ultimate levels, counteracting actions applied to mitigate failure or extend the service life of RCSPs are accompanied by consequences in other words cost. As discussed in **Section 3.3**, the cost is divided into two main categories, direct and indirect cost, and depends on different impact factors. These factors are site, material, and action specific. The 42 $inch$ RCSP with a total length of 0.5 $miles$ (i.e., 2640 ft) is located under one of the main roads in Arlington, Texas. To investigate the direct cost associated with either replacement or rehabilitation using CIPP, it is essential to evaluate associated activities, which are the impact factors. **Table 13** gives values of impact factors for the two alternatives to be used in this case study. Regression models defined in **Section 3.3.1** along with Eq. 47 can be used to obtain the predictive distributions for both alternatives, which are displayed in **Fig. 24.**

Table 13. Set of construction activities to be conducted on either alternative.

Impact Factor	Open-Cut Replacement (ultimate level)	Cured in Place Liner (CIPP) (service level)
Diameter	42-inch	42-inch
Material	PVC pipe	-
Surface Reinstatement	1	-
Manhole Replacement	1	-
Inspection & Cleaning	1	1
Traffic Control	1	1
Lateral Connection	1	1
Manhole Rehabilitation	-	1
Bypass pumping	-	1

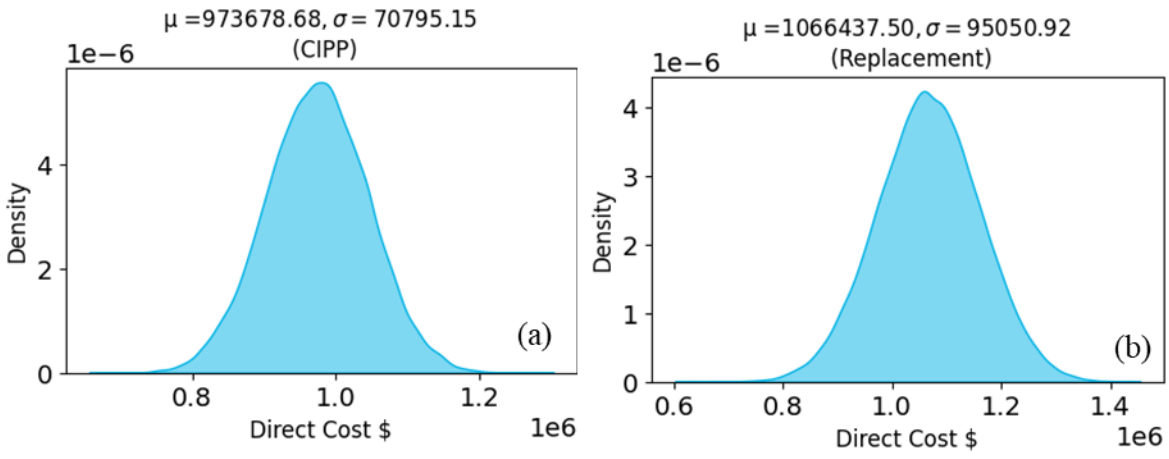

Fig. 24. Direct cost predictive distribution: **(a)** Cured-in-place liner CIPP; **(b)** Replacement.

After estimating the direct cost predictive distribution, the next step is to estimate the predictive distribution of the indirect costs. According to **Section 3.3.2**, the indirect cost in this study includes costs related to reduction in the service life of pavement, noise pollution, traffic delay cost, and vehicle operating costs. Because of the high uncertainties associated with these costs, a Monte-Carlo simulation will be conducted to generate predictive distribution. A summary of input deterministic and stochastic random variables with their references is provided in **Table 14**.

For any activities to be conducted on this pipe, there are three main scenarios for traffic control as shown in **Fig. 25**. The first one is closing one lane and controlling the second one by traffic control. The second one is to divert the traffic flow to the shoulder. The third scenario includes the complete closure of the road and the detour of the traffic to a different road. For simplicity, the first scenario will be used in this study. Additionally, construction activities induce different levels of noise depending on the type of equipment used to conduct them. A typical set of equipment used in both CIPP and replacement with their associated noise level measured in dB is shown in **Table 15.**

Table 14. List of input parameters to be used in indirect cost evaluation.

Parameters	Distribution	Values	Reference
$pavement\ age$	Deterministic	36 $years$	Assumed to have same ages as the pipe.
$service\ life$	Normal	$\mu = 12\ years$, $\sigma = 2\ years$	(TXDOT 2023)[1]
$intial\ cost$	Normal	$\mu = 468{,}620\ \$/lane.mile$, $\sigma = 50{,}000\ \$/lane.mile$	(Andrew et al. 2009) Assuming rigid pavements
$C_{maintenance}$	Normal	$\mu = 2{,}189\ \$/lane.mile$, $\sigma = 218.9\ \$/lane.mile$	(Andrew et al. 2009) Assuming rigid pavements
C_{rehab}	lognormal	$\mu = 29.85\ \$/ft$, $\sigma = 2.98\ \$/ft$	Estimated from the direct cost bidding tabs of replacement project
Population Density	Uniform	$Lower\ bound = 100\ capita/mile^2$, $Upper\ bound = 14{,}000\ capita/mile^2$	(staticatlas.com)
Speed	Discrete	$[35,40,45,50,55]mph$	Typically founded in local and arterial roads
$AADT$	lognormal	$\mu = 4542.61\ veh/day$, $\sigma = 454.3\ veh/day$	(gis-txdot.opendata.arcgis.com)
HV	Uniform	$Lower\ bound = 2\%$, $Upper\ bound = 25\%$	Valid values found in (HCM. 2000)
Replacement duration	Normal	$\mu = 60\ days$, $\sigma = 5$ days	Assumed
CIPP duration	Normal	$\mu = 30\ days$, $\sigma = 5$ days	Assumed
PV	Normal	$\mu = 250{,}000\ \$$, $\sigma = 50{,}000\ \$$	Assumed
The average population per household	Deterministic	5	Assumed
$V_{user\ Truck}$	lognormal	$\mu = 47.94\ \$/hr$, $\sigma = 4.8\ \$/hr$	(TXDOT. 2023)[2]
$V_{user\ Car}$	lognormal	$\mu = 34.93\ \$/hr$, $\sigma = 3.5\ \$/hr$	(TXDOT. 2023)[2]
AOV_{Cars}	Discrete	$[1,2,3]\ passenger$	(TXDOT. 2023)[3]
AOV_{Truck}	Deterministic	$1\ passenger$	(TXDOT. 2023)[3]
Detour ratio	Uniform	$Lower\ bound = 1$, $Upper\ bound = 2$	Assumed

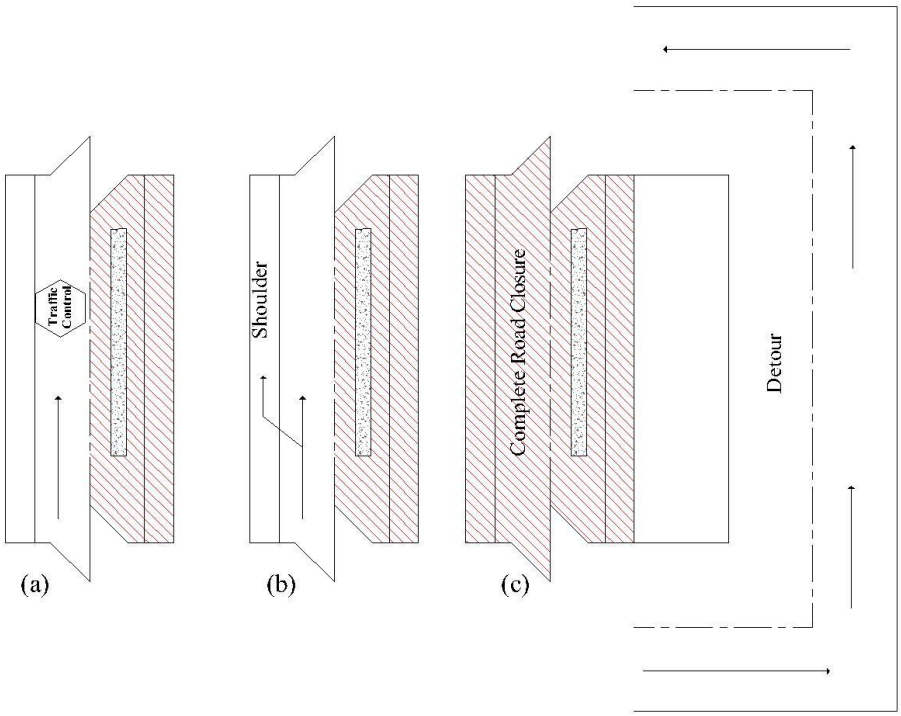

Fig. 25. Traffic control scenarios; **(a)** One lane closure with traffic control; **(b)** One lane closure with diverting traffic to shoulder; **(c)** Complete road closure.

Table 15. Noise level of construction equipment used in CIPP and replacement alternatives.

Alternative	Equipment	Noise Level (dB)
Cured in Place Liner (CIPP)	Air compressor	80
	Generator	80
	Pump	77
	Utility Truck	84
	TV Truck	84
	Jeter Truck	84
	Refrigerator Unit	82
Replacement	Air compressor	80
	Backhoe	80
	Pump	77
	Crane Mobility	85
	Dump Truck	84
	Utility Truck	84
	Grader	85
	Roller	85
	Jack Hammer	85
	Paver	85

Some indirect cost categories might be irrelevant to some construction alternatives; for example, CIPP does not necessarily require excavation unless, in certain circumstances, access to the pipe is available. Therefore, in this case study, the pavement reduction value and maintenance are excluded from this alternative. For the replacement alternative, all categories will be included in the analysis. Since the age of the adjacent pavement exceeds the service life at the time of failure, the pavement reduction value will simply be the cost of rehabilitation or reinstatement of the pavement adjacent to the pipe along the working zone and not the reduced value added to the increase in maintenance cost. The outcome of Monte-Carlo simulation is a predictive distribution for each alternative, which can be assumed to follow normal distribution according to the central limit theorem.

Finally, the predictive distributions of direct and indirect cost can be combined according to Eq. 62. **Fig. 26** presents the total cost or consequences distribution.

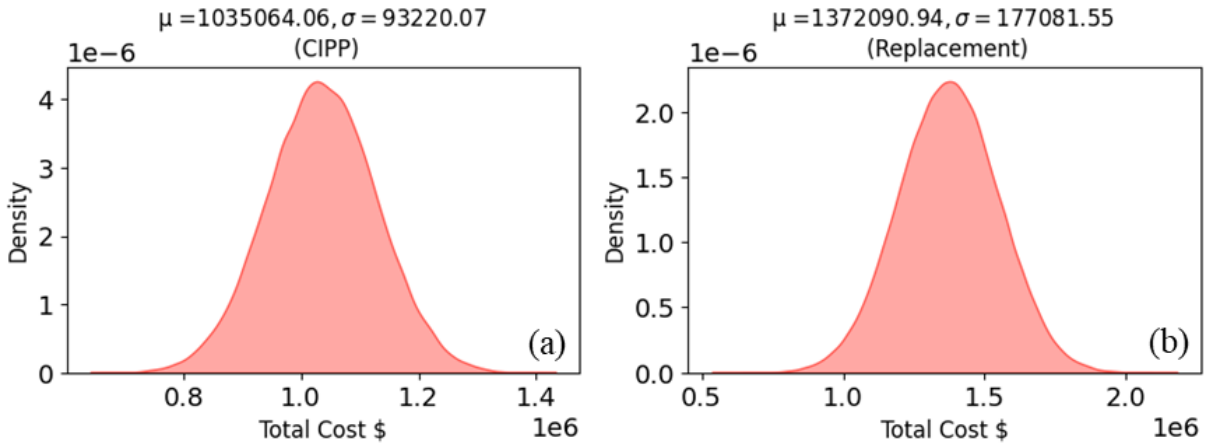

Fig. 26. Total cost predictive distribution: **(a)** cured in place liner (CIPP); **(b)** Replacement.

4.4. Risk Assessment

4.4.1. Parameters Multiplications

To conduct this approach, the likelihood $P(t)$, at both levels must be scaled by its permissible value P_{limit}. On each level, the risk can be evaluated on either failure mode or multiple failure modes. In this case study, the crack width failure mode will be used at the service level, while the combined effect of all failure modes will be used at the ultimate level. The reason behind selecting the crack width as the main failure mode to address serviceability is that under the effect of chloride-induced corrosion, crack propagation is more detrimental than wall erosion as reflected by the service life shown in **Table 12**, while at the ultimate level, most failure modes have consistent effect. The expected outcome of this approach is a risk random process shown in **Fig. 27**, which is a finite set of random variables over time steps [0, 120].

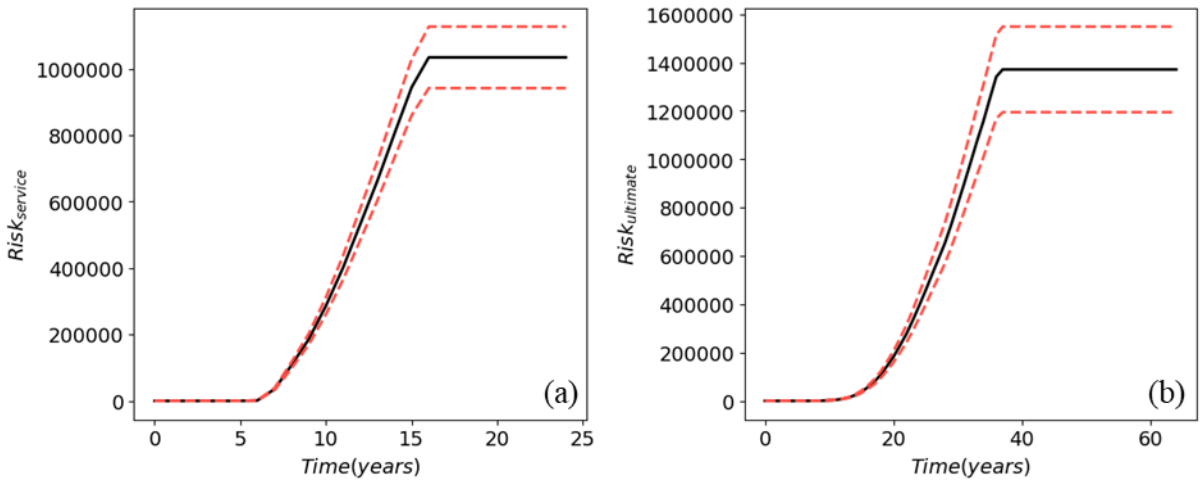

Fig. 27. Risk random process at: **(a)** Service level; **(b)** Ultimate level.

Risk interpreted monetarily can be expressed on an ordinal scale by scaling risk values by allowable budgets as shown in **Fig.27**. For this case study, it is assumed that the budget is a constant value over the study period since no information was available about the annual allocation for rehabilitation or replacement. The total budget will be $1,000,000 and $2,000,000 for a typical rehabilitation and replacement, respectively. However, in future studies, a time series forecasting model can be used to estimate the budget at a certain year based on available datasets of prior years and the rate of inflations.

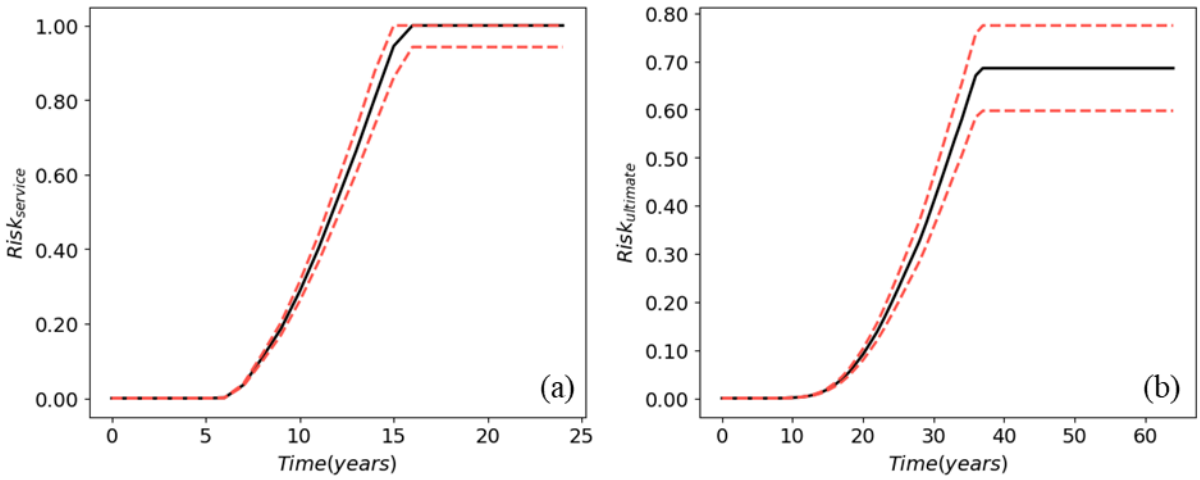

Fig. 28. Risk random process scaled by allowable budget: **(a)** Service level; **(b)** Ultimate level.

4.4.2. Risk matrix

The risk matrix is a qualitative approach to risk assessment described in **Section 3.4.2**. It consists of a set of rules that combine maps of the interactions between the likelihoods and consequences of qualitative classes to risk classes. Therefore, to make this approach available, likelihoods and consequences must be converted to qualitative classes. As shown in **Table 16**, likelihoods and consequences must be scaled by the permissible likelihood values and available budget, respectively. **Fig 29** shows the consequences of class distribution based on budget. The designated class of consequences for each alternative is the class that occupies the largest area under the distribution. This can be found by finding the largest cumulative density function value among class intervals as illustrated in **Section 3.4.2.** Finally, risk classes over RCSP's lifetime at both levels can be obtained as shown in **Fig 30** using a set of rules defined in the risk matrix in **Fig 13**.

Table 16. Qualitative class definitions for both likelihood and consequences.

	Likelihood	Consequences
Low	$0 \leq \frac{P(t)}{P_{limit}} < 0.2$	$0 \leq \frac{Consequnces}{Budget} < 0.2$
Low to Moderate	$0.2 \leq \frac{P(t)}{P_{limit}} < 0.4$	$0.2 \leq \frac{Consequnces}{Budget} < 0.4$
Moderate	$0.4 \leq \frac{P(t)}{P_{limit}} < 0.6$	$0.4 \leq \frac{Consequnces}{Budget} < 0.6$
High	$0.6 \leq \frac{P(t)}{P_{limit}} < 0.8$	$0.6 \leq \frac{Consequnces}{Budget} < 0.8$
Very High	$0.8 \leq \frac{P(t)}{P_{limit}} < 1$	$0.8 \leq \frac{Consequnces}{Budget}$

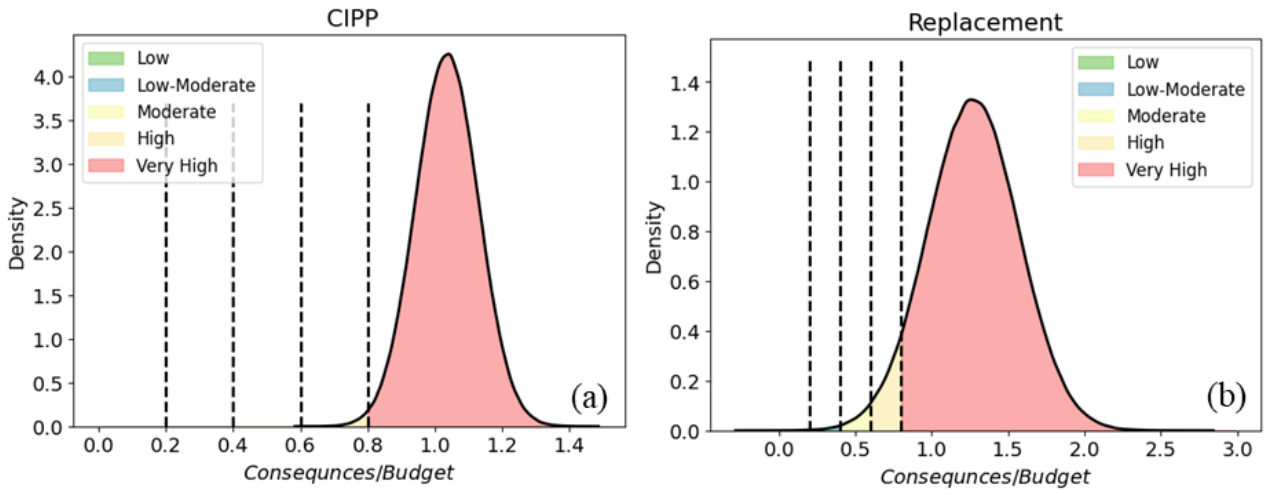

Fig. 28. Consequences to the budget ratio: **(a)** Cured-in-place liner (CIPP); **(b)** Replacement with PVC pipe.

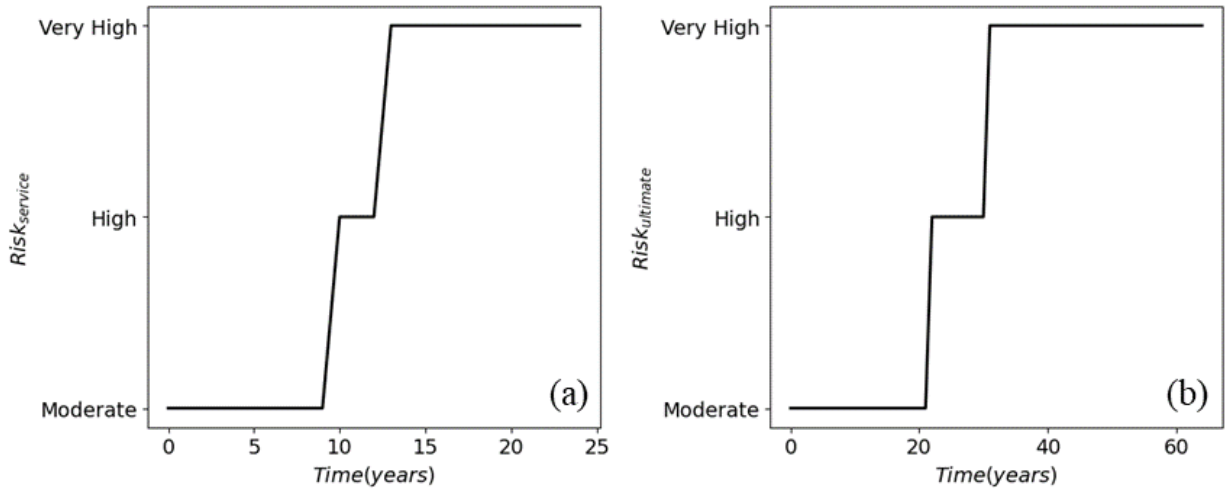

Fig. 29. Risk qualitative classes over time: **(a)** Service level; **(b)** Ultimate level.

4.4.3 Neuro-Fuzzy system

The neuro-fuzzy system is the integration of the FIS with the neural network as described in **Section 3.4.3.** Before using this system in risk assessment applications, it must be trained on a desired dataset to have the optimal parameters of the FIS system interpreted in the activation functions and weights of the neural network. It has two learning phases: structural and supervised learning phases.

4.4.3.1. Structural Learning Phase

The first step in the training process is the structural learning phase described in **Section 3.4.3.1**, which includes setting up the number of fuzzy sets for each input and output parameter and their membership functions. The neuro-fuzzy system defined in **Fig. 16** will be adopted in this study. It consists of two inputs, likelihood, and consequences ratio CR; five fuzzy sets for each input and output, which reflects five classes (i.e., low, low to moderate, moderate, high, and very high) used in the risk matrix shown in **Fig. 13**; and gaussian membership function type for all

fuzzy sets except the last fuzzy set for CR. After evaluating the CR, it is found to be unbounded from the left side, which means that when assuming a Gaussian membership function for the last fuzzy set (i.e., Very High), this membership function will give zero membership value similar to other membership functions of other fuzzy sets within the universe of discourse, especially for large CR . Therefore, a sigmoid membership function shown in Eq. 79 is assigned to the last fuzzy set of CR, wherein a_{25} & b_{25} are the inflection point and factor controlling the transition width, respectively. Ranges of fuzzy sets in addition to initial parameter values of membership functions are shown in **Table 17**.

$$y_{25}{}^{2} = \frac{1}{1+e^{-b_{25}(y_2{}^{1}-a_{25})}} \tag{79}$$

Compared to prior risk assessment approaches, this approach presents a risk on an ordinal scale from zero to one with the risk fuzzy sets ranges defined on that scale. For the inference mechanism, Mamadani-based approaches will be used with the default number of rules equal to 25 based on the number of inputs fuzzy sets combination as explained in **Section 3.4.3.1.**

Table 17. Initial input and output parameter values.

	Fuzzy set	Range	Parameters
likelihood (input)			
	Low	$p\{p \in \mathbb{R} \mid 0 \leq p < 0.2\}$	$a_{11} = 0.1, b_{11} = 0.1$
	Low to Moderate	$p\{p \in \mathbb{R} \mid 0.2 \leq p < 0.4\}$	$a_{12} = 0.25, b_{12} = 0.1$
	Moderate	$p\{p \in \mathbb{R} \mid 0.4 \leq p < 0.6\}$	$a_{13} = 0.52, b_{13} = 0.1$
	High	$p\{p \in \mathbb{R} \mid 0.6 \leq p < 0.8\}$	$a_{14} = 0.78, b_{14} = 0.1$
	Very High	$p\{p \in \mathbb{R} \mid 0.8 \leq p \leq 1.0\}$	$a_{15} = 0.95, b_{15} = 0.1$
Consequences Ratio (input)			
	Low	$c\{c \in \mathbb{R} \mid 0 \leq c < 0.2\}$	$a_{21} = 0.1, b_{21} = 0.1$
	Low to Moderate	$c\{c \in \mathbb{R} \mid 0.2 \leq c < 0.4\}$	$a_{22} = 0.34, b_{22} = 0.1$
	Moderate	$c\{c \in \mathbb{R} \mid 0.4 \leq c < 0.6\}$	$a_{23} = 0.6, b_{23} = 0.1$
	High	$c\{c \in \mathbb{R} \mid 0.6 \leq c < 0.8\}$	$a_{24} = 0.74, b_{24} = 0.1$
	Very High	$c\{c \in \mathbb{R} \mid 0.8 \leq c\}$	$a_{25} = 0.95, b_{25} = 5$
Risk (output)			
	Low	$R_1\{R \in \mathbb{R} \mid 0 \leq R < 0.2\}$	$c_{11} = 0.05, d_{11} = 0.1$
	Low to Moderate	$R_2\{R \in \mathbb{R} \mid 0.2 \leq R < 0.4\}$	$c_{12} = 0.25, d_{12} = 0.1$
	Moderate	$R_3\{R \in \mathbb{R} \mid 0.4 \leq R < 0.6\}$	$c_{13} = 0.55, d_{13} = 0.1$
	High	$R_4\{R \in \mathbb{R} \mid 0.6 \leq R < 0.8\}$	$c_{14} = 0.8, d_{14} = 0.1$
	Very High	$R_5\{Risk \in \mathbb{R} \mid 0.8 \leq R \leq 1\}$	$c_{15} = 0.95, d_{15} = 0.1$

4.4.3.2. Supervised Learning Phase

After setting up the structure of the neuro-fuzzy system and initial parameter values, the next step is to train and validate the model on datasets to obtain the optimal parameter values. The dataset can be obtained using the proposed framework shown in **Section 3.4.3.1**, which requires a set of pipe observations; evaluation of corresponding likelihood and consequences; and classification of likelihood, consequences, and associated risk by experts. Since these observations are not available in hand and because the purpose of this study is to demonstrate the power of the

neuro-fuzzy system in learning the optimal parameters and the knowledge base, this model will be trained on randomly generated data from the risk matrix shown in **Fig.13**. a sample of the dataset are shown in **Table 18**. For training purposes, the risk output in the dataset is taken as the median of fuzzy set intervals, which ensures faster convergence.

Table 18. Sample training data set used for training the model.

No. sample	Failure likelihood	Consequences of failure	Risk	Risk interval
1	0.81	0.58	3.5 (High)	$R_4\{R \in \mathbb{R} \mid 0.6 \leq R < 0.8\}$
2	0.96	0.63	4.5 (Very High)	$R_5\{R \in \mathbb{R} \mid 0.8 \leq R < 1.0\}$
3	0.15	0.54	1.5 (Low to Moderate)	$R_2\{R \in \mathbb{R} \mid 0.2 \leq R < 0.4\}$
4	0.14	0.99	2.5 (Moderate)	$R_3\{R \in \mathbb{R} \mid 0.4 \leq R < 0.6\}$
m	0.09	0.11	0.5 (Low)	$R_1\{R \in \mathbb{R} \mid 0 \leq R < 0.2\}$

The size of the generated dataset is 1,000 samples, which is equivalent to 100 observations evaluated by ten experts. 80% of this data will be used to train the model, while the rest will be used for validation.

In the following sections, the analysis will be conducted as follows: Firstly, a stochastic gradient descent optimization algorithm will be used to train and obtain the optimal parameters. Secondly, the model will be retrained on different optimization algorithms seeking to enhance the training process, and finally, an illustration of model adaptability will be shown by training the model after inducing different changing scenarios either in the fuzzy sets or the knowledge base.

4.4.3.2.1. parameter learning

In this section, stochastic gradient descent (SGD) will be used to train the model (i.e., obtain trainable parameters shown in **Table 8** and the knowledge base). This algorithm is applied using the backpropagation process illustrated in **Appendix II** to minimize the objective function shown in Eq.74. The training process will be conducted in mini batches of size 40 samples and with a learning rate of 0.005. The training process is halted whenever the error on the epoch level E_{epoch} reaches 0.0005. After running the training process the total number of epochs required to reach the desired error level is 811 epochs; the values of trainable parameters and knowledge base rules weights are displayed in **Table 19** and **Fig. 31.** Finally, the trained membership function shapes for likelihood, consequences, and risk are displayed in **Fig. 32**, where the trained membership functions are displayed in colored solid lines.

Table 19. Final inputs and outputs membership functions parameters.

	Fuzzy set	Parameters
likelihood (input)		
	Low	$a_{11} = 0.042, b_{11} = 0.096$
	Low to Moderate	$a_{12} = 0.273, b_{12} = 0.095$
	Moderate	$a_{13} = 0.502\ b_{13} = 0.092$
	High	$a_{14} = 0.722, b_{14} = 0.089$
	Very High	$a_{15} = 0.944, b_{15} = 0.098$
Consequences (input)		
	Low	$a_{21} = 0.035, b_{21} = 0.094$
	Low to Moderate	$a_{22} = 0.271, b_{22} = 0.098$
	Moderate	$a_{23} = 0.527, b_{23} = 0.108$
	High	$a_{24} = 0.867, b_{24} = 0.16$
	Very High	$a_{25} = 1.08, b_{25} = 9.99$
Risk (output)		
	Low	$c_{11} = 0.029, d_{11} = 0.087$
	Low to Moderate	$c_{12} = 0.268, d_{12} = 0.103$
	Moderate	$c_{13} = 0.526, d_{13} = 0.108$
	High	$c_{14} = 0.771, d_{14} = 0.093$
	Very High	$c_{15} = 0.975, d_{15} = 0.073$
Lagrange multipliers	likelihood	$\lambda_1 = 0.0158$
	Consequences	$\lambda_2 = 0.0403$
	Risk	$\lambda_3 = 0.001$

Probability of Failure	Consequences of Failure: Low (0-0.2)	Low-moderate (0.2-0.4)	Moderate (0.4-0.6)	High (0.6-0.8)	Very High (>0.8)
Low (0-0.2)	$w = 0.717$	$w = 0.928$	$w = 0.919$	$w = 0.972$	$w = 0.968$
Low-Moderate (0.2-0.4)	$w = 0.711$	$w = 0.937$	$w = 0.973$	$w = 0.942$	$w = 0.790$
Moderate (0.4-0.6)	$w = 0.914$	$w = 0.915$	$w = 0.966$	$w = 0.728$	$w = 0.742$
High (0.6-0.8)	$w = 0.936$	$w = 0.977$	$w = 0.953$	$w = 0.8$	$w = 0.678$
Very-high (0.8-1)	$w = 0.971$	$w = 0.965$	$w = 0.824$	$w = 0.820$	$w = 0.695$

Fig. 30. Rules firing strength (i.e., layer IV weights) after training using the modified method in this study.

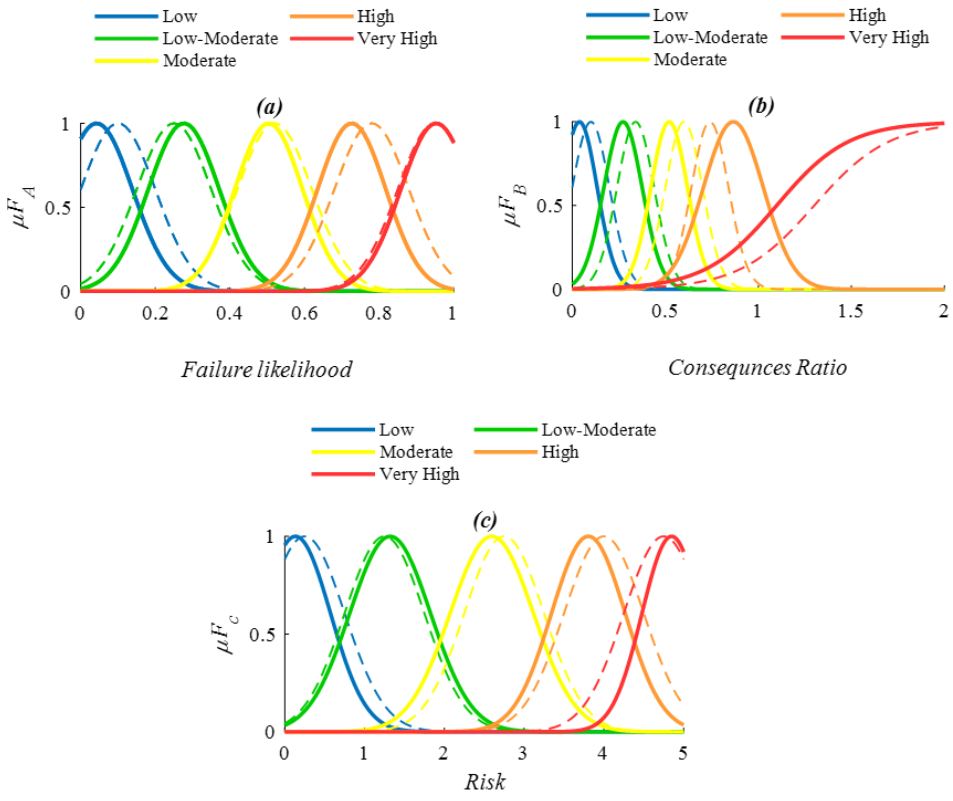

Fig. 31. Initial and updated membership functions for **(a)** likelihood of failure, **(b)** Consequence ratio, and **(c)** Risk.

4.4.3.3. Outperforming Optimization Algorithm

In this section, a set of optimization algorithms with different learning rates are investigated. Suggested optimization algorithms are discussed in **Table 9**. The best optimization algorithm is the one that provides the least number of epochs to reach the desired error threshold (i.e., 0.005). Based on **Table 20**, Adam's optimizer with a learning rate of 0.001 shows the best performance.

Table 20. Optimization algorithms performance in training the neuro-fuzzy system.

Optimiser	Adam[a]	Adelta[a]	Adagrad[a]	NAG[a]	NAG[b]	Momentum[a]	Momentum[b]	SGD[b]
Number of epochs	19	31	2263	392	69	395	73	811
Training error	0.0005	0.0005	0.0005	0.0005	0.0005	0.0005	0.0005	0.0005
Validation error	0.0041	0.0041	0.0040	0.0042	0.0043	0.0043	0.0042	0.0047
Validation error-Training error	0.0036	0.0036	0.0035	0.0037	0.0038	0.0038	0.0037	0.00042

Note:
[a] Optimisation algorithm with γ of 0.001.
[b] Optimisation algorithm with γ of 0.005.

4.4.3.4. Model's adaptability

One of the advantages of the neuro-fuzzy model is its ability to accommodate changes in the fuzzy intervals and rule weights. These changes are commonly induced by decision-makers to match their perspectives and desires. In this case study, three potential scenarios will be induced as displayed in **Fig. 33**. In the first scenario, part of the rules presented in grey color are restrained to a firing strength of 0.5, which reflects incomplete or vague knowledge, or high uncertainty about

these decisions; therefore, limiting their contribution in the inference process. The other two scenarios are related to changes in the fuzzy intervals of consequences ratio and risk as presented in green and yellow labels in **Fig. 33**. The last two scenarios are all about reducing the impact of "Low" and "Very High" fuzzy sets of consequences ratio and risk in the decision-making process due to insignificant impact or mandating immediate interventions. For example, from a decision-maker point of view, "Low" and "Very High" linguistic expressions in consequences relate to either structures in abandoned areas that have negligible impacts, or to structures that can have massive economic or social impacts. Similarly, "Low" and "Very High" linguistic expressions in risk relate to either structures in inventory conditions (insignificant failure likelihood) with negligible failure impacts, or to structures with forthcoming failure (high failure likelihood) that have high impact and demand immediate intervention. In both cases, decision makers would prefer to eliminate these structures from the decision process to some extent by reducing the size of intervals, which they affiliate to as they are not critical, or decisions have already been made about them.

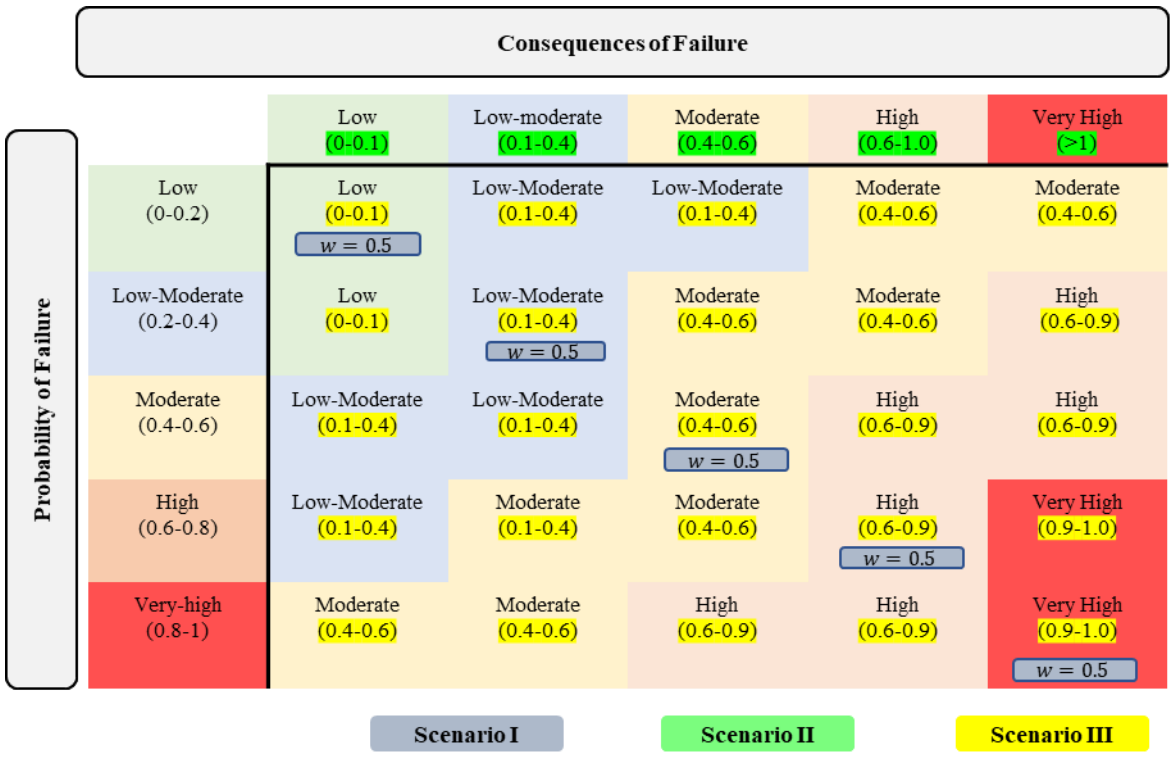

Fig. 32. Illustration of different changes to the original risk matrix based on three different scenarios.

The model will be retained using the outperforming optimization algorithm, which is the Adam optimizer with a learning rate of 0.001 as shown in the previous section. Results including trainable parameters are displayed in **Table 21** and **Table 22**.

Table 21. Final inputs and outputs membership functions parameters for scenarios I & II.

	Fuzzy set	Scenario I	Scenario II
likelihood (input)			
	Low	$a_{11} = 0.044\ b_{11} = 0.098$	$a_{11} = 0.055, b_{11} = 0.109$
	Low to Moderate	$a_{12} = 0.280\ b_{12} = 0.095$	$a_{12} = 0.290, b_{12} = 0.093$
	Moderate	$a_{13} = 0.506, b_{13} = 0.090$	$a_{13} = 0.506, b_{13} = 0.083$
	High	$a_{14} = 0.729, b_{14} = 0.092$	$a_{14} = 0.723, b_{14} = 0.082$
	Very High	$a_{15} = 0.954, b_{15} = 0.094$	$a_{15} = 0.942, b_{15} = 0.104$
Consequences Ratio (input)			
	Low	$a_{21} = 0.041, b_{21} = 0.095$	$a_{21} = 0.016, b_{21} = 0.092$
	Low to Moderate	$a_{22} = 0.270\ b_{22} = 0.098$	$a_{22} = 0.251, b_{22} = 0.168$
	Moderate	$a_{23} = 0.502, b_{23} = 0.088$	$a_{23} = 0.577, b_{23} = 0.137$
	High	$a_{24} = 0.798, b_{24} = 0.140$	$a_{24} = 0.973, b_{24} = 0.159$
	Very High	$a_{25} = 1.082, b_{25} = 5.164$	$a_{25} = 1.213, b_{25} = 4.98$
Risk (output)			
	Low	$c_{11} = 0.026, d_{11} = 0.089$	$c_{11} = 0.022, d_{11} = 0.061$
	Low to Moderate	$c_{12} = 0.265, d_{12} = 0.100$	$c_{12} = 0.290, d_{12} = 0.105$
	Moderate	$c_{13} = 0.517, d_{13} = 0.102$	$c_{13} = 0.541, d_{13} = 0.096$
	High	$c_{14} = 0.755, d_{14} = 0.090$	$c_{14} = 0.759, d_{14} = 0.073$
	Very High	$c_{15} = 0.96, d_{15} = 0.073$	$c_{15} = 0.954, d_{15} = 0.069$
Lagrange multipliers	likelihood	$\lambda_1 = 0.099$	$\lambda_1 = 0.000$
	Consequences	$\lambda_2 = 0.000$	$\lambda_2 = 0.000$
	Risk	$\lambda_3 = 0.000$	$\lambda_3 = 0.000$

Table 22. Final inputs and outputs membership functions parameters for scenarios III.

	Fuzzy set	Scenario III
likelihood (input)		
	Low	$a_{11} = 0.046, b_{11} = 0.098$
	Low to Moderate	$a_{12} = 0.280, b_{12} = 0.092$
	Moderate	$a_{13} = 0.498, b_{13} = 0.086$
	High	$a_{14} = 0.717, b_{14} = 0.093$
	Very High	$a_{15} = 0.949, b_{15} = 0.098$
Consequences Ratio (input)		
	Low	$a_{21} = 0.039, b_{21} = 0.102$
	Low to Moderate	$a_{22} = 0.269, b_{22} = 0.119$
	Moderate	$a_{23} = 0.503, b_{23} = 0.090$
	High	$a_{24} = 0.800, b_{24} = 0.117$
	Very High	$a_{25} = 1.09, b_{25} = 5.10$
Risk (output)		
	Low	$c_{11} = 0.018, d_{11} = 0.094$
	Low to Moderate	$c_{12} = 0.263, d_{12} = 0.103$
	Moderate	$c_{13} = 0.516, d_{13} = 0.102$
	High	$c_{14} = 0.752, d_{14} = 0.087$
	Very High	$c_{15} = 0.962, d_{15} = 0.076$
Lagrange multipliers	likelihood	$\lambda_1 = 0.095$
	Consequences	$\lambda_2 = 0.000$
	Risk	$\lambda_3 = 0.000$

4.4.3.5. Risk Assessment Results Using Neuro-Fuzzy System

After training the model and obtaining the best parameters, it can be used for risk assessment. Similar to the application of previous approaches, the likelihood at the service and ultimate level in addition to the predicted consequences ratio will be used for risk assessment. **Fig. 34** show the variation of risk expressed on an ordinal scale [0,1] at both level over the lifetime of the RCSP under investigation.

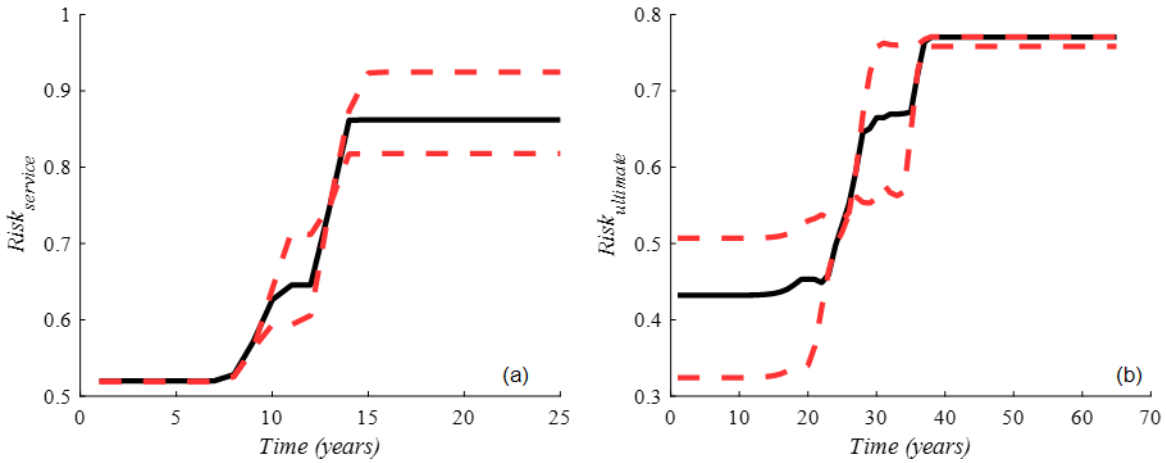

Fig. 33. Risk assessment results using neuro-fuzzy approach at **(a)** Service level; and **(b)** Ultimate level.

Chapter 5. Discussion

5.1. Overview

This chapter provides a discussion about the outcomes of both reliability and risk assessment methodologies after the case study application. The first section will discuss the outcomes of reliability analysis including the impact of different factors on the reliability. The second section will discuss the outcomes of the consequences evaluation and the impact of each of the cost categories impact factors on the consequences. The final section will present a discussion about the results of the three risk assessment approaches, the outperforming optimization algorithm, neuro-fuzzy model adaptability, and finally comparison among risk assessment approaches and their best state-of-practice.

5.2. Reliability Analysis and Likelihoods

After conducting the Monte-Carlo simulation to estimate the initiation time of environmental condition $t_{in_{Cl}}$ and $t_{in_{H_2S}}$, which are 1 and 11 years, respectively, subsequent time-dependent simulations were conducted at both service and ultimate levels to examine the service life and failure time of RCSP under investigation. The outcomes of these simulations are profiles that show the variation of likelihoods for different failure modes and their combinations at both levels as shown in **Fig. 22 & 23**. Starting at the serviceability level, compared to crack width and bond strength loss limit states, the wall thickness loss limit state under the impact of sulfide-induced erosion provides the highest reliability and service life for almost two to three times higher than other limit states. This is attributed to the early commencement of chloride-induced corrosion, which primarily affects crack width propagation and bond strength loss. Another reason for the

high reliability of RCSP against wall erosion is the rate of failure, as shown in **Fig. 22**, the wall thickness loss shows the lowest rate of failure compared to other limit states.

Based on **Fig. 22**, the rate of bond strength loss is higher than crack width propagation. During the uncracked and partially cracked stage shown in **Fig. 6**, the radial compressive stresses σ_{r,r_s} from concrete causing confinement increases and reach its maximum values when cracks extend through 94% of the cover thickness on average as shown in **Fig. 35a**. Higher or lower values depend on the corrosion current density i_{corr} ; as i_{corr} increases, the average amount of corrosion p_{avg} increases, which results in higher hoop stresses and faster crack propagation, hence earlier strength loss. At a full cracked stage, the confinement provided by concrete diminishes significantly due to the softening effect. Similarly, the confinement provided by corrosion products reduces, too, and depends on the crack width w. As the w increases, the radial displacement U_{rs} increases causing dissipation of corrosion product, hence reduction in σ_{r,r_s}as shown in **Fig. 35b**. The residual bond strength shown in **Fig. 35b** is retained by the friction and the adhesion between reinforcement and concrete.

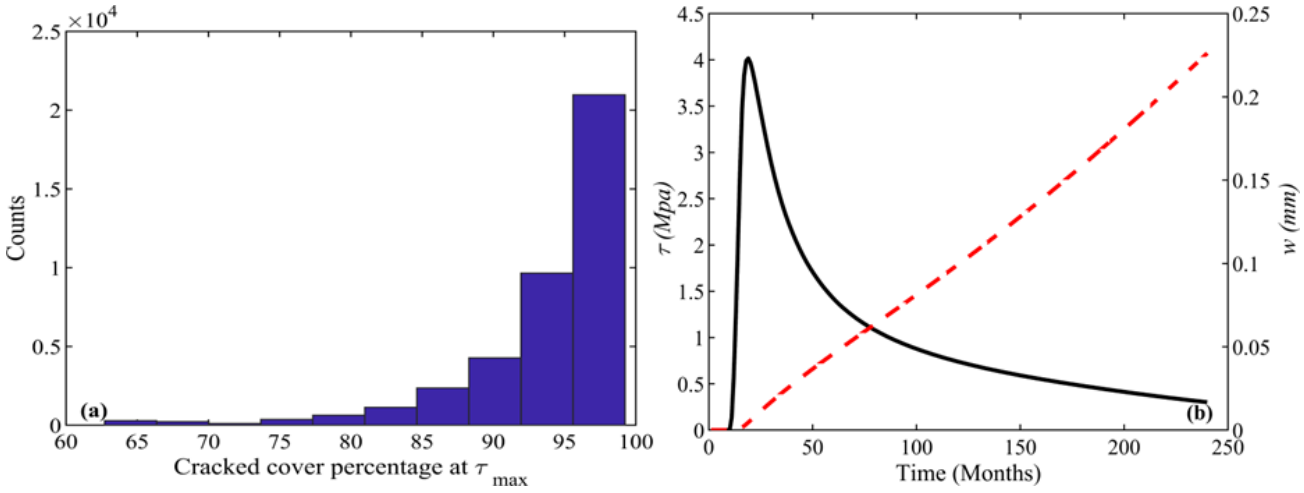

Fig. 35. (a) Cracked cover percentage at τ_{max}; **(b)** The change of $\sigma_{r,r_s}$with w.

Following the reduction in bond strength, crack width propagation at the surface occurs at a fast rate. The rate of propagation depends on a set of factors including the corrosion product expansion ratio α, concrete cover, and reinforcement sizes. The α ratio is basically, the density ratio of corrosion products relative to reinforcement and it ranges from 2.9 up to 6 depending on the environment. In the sewer environment, this ratio varies from 2.9 to 3.3 according to Zhao et al (2011) and its effect on the rate of crack propagation is explained in **Fig. 36a,** which shows a 1.67% increase in the rate of crack development for each 1% increase in the α. **Fig. 36b & c** show the variation in the rate of crack width propagation based on the rebar size and concrete cover. It is obvious that the rate of crack propagation increases with the increase in the rebar diameter and the decrease in the cover due to a reduction in σ_{r,r_s}, which provides confinement action from surrounding concrete as shown in **Fig. 36d**.

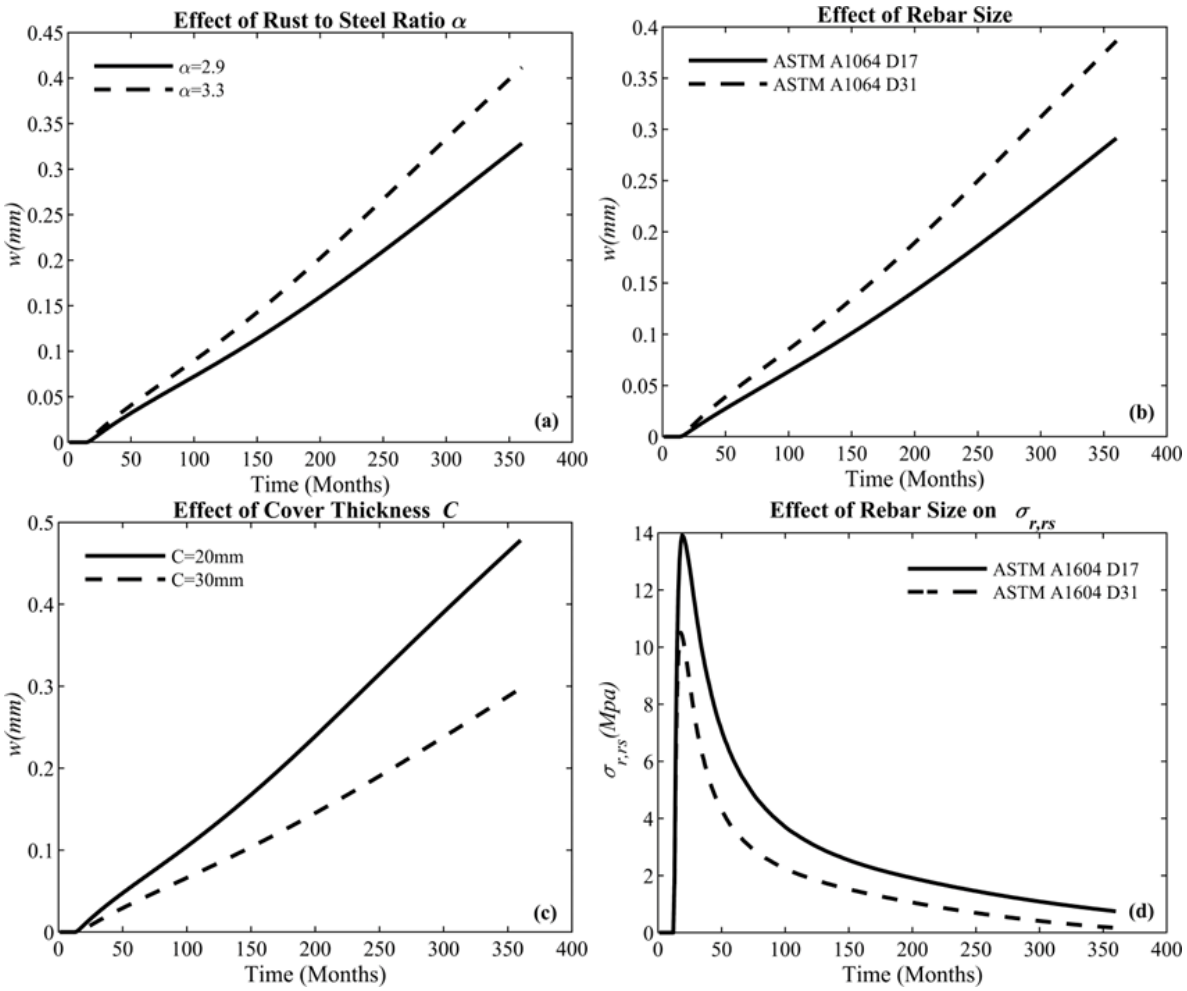

Fig. 34. (a) The effect of rust to steel volume ratio α on the cracking process; **(b)** The effect of rebar size r_s of the cracking process; **(c)** The effect of cover thickness C on the cracking process; **(d)** The effect of rebar size on σ_{r,r_s}.

At the ultimate level, all limit state functions expect the radial tension loss have a consistent failure rate. All these functions reflect the reduction in the resistance or the capacity because of geometrical and mechanical properties changes in both concrete and reinforcement. **Fig. 37** shows the time-dependent reduction in the concrete compressive strength, reinforcement yield strength, and ultimate strain. Although the rate of reduction in the ultimate strain is higher than the reduction of other properties, the brittle failure rate displayed in **Fig. 23b** is lower than in flexural and shear,

which depend mainly on the compressive strength and yield strength, respectively. This is expected since for ASTM A1064 deformed wires used in RCSP, the ultimate strain ε_u, is 20 times larger than the yield strain ε_y, according to (ACI PRC 439.5 2018), additionally, the flexural and shear strength depends on other factors that also deteriorate under environmental conditions such as wall thickness and reinforcement area, which expedite their rate of failure.

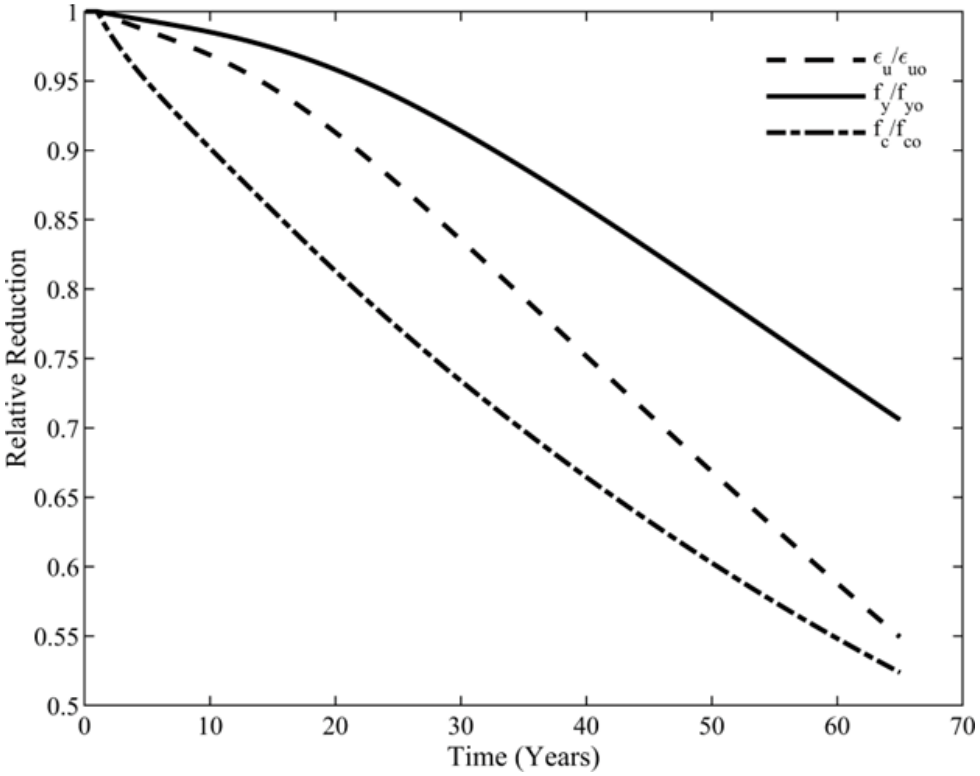

Fig. 35. Reduction rates of compressive strength f_c', yield strength f_y, and ultimate strain ε_u.

The rate of flexural failure is the highest among the rest of the limit states because of its significant dependencies on such parameters including the yield strength f_y, the residual reinforcement A_{sr}, and the remaining wall thickness h_r, that deteriorate under environmental conditions. The first two factors cause a reduction in the wire reinforcement in carrying tensile stresses, while the last factor, h_r reduces the thrust loading contribution in resisting the

compressive strength. Additionally, since the rate of reduction of the compressive strength f_c', is higher than the yield strength f_y, the depth of the compressive zone a_1, obtained from Eq. 38 increases, which leads to a reduction in the lever arm between the tensile forces $A_{sr}f_y$, and thrust load N_{ult}; therefore, reducing the flexural capacity.

The shear stresses exerted on the pipe are assumed to be resisted sufficiently by concrete thickness according to ASTM C76 (2022). The resistance part is the basic shear formula, which reflects the lowest possible shear strength that a pipe can sustain at the critical section, which is located at $M/Vd = 3$ from the pipe crown. As shown in Eq. 39, the residual shear strength capacity depends on the compressive strength f_c', the residual reinforcement A_{sr}, which are responsible for strength reduction.

The lowest observed rate of failure was found in the radial tension limit state function. Due to the pipe's circular shape, tensile forces in rebar $A_{sr}f_y$ has a radial component that is expected to cause splitting cracks along the wall thickness and should be resisted by the concrete. Because the rate of reduction of the compressive strength f_c' is higher than the rate of reduction of the residual reinforcement A_{sr} and the yield strength f_y, there will be a chance for a radial tension failure, but at a very low rate as demonstrated in **Fig. 23c**.

This study adds a contribution to the field of service life and failure predictions of RCSPs. A Previous study such as Alani and Faramarzi (2015) considered only the effect of sulfide erosion in the reliability evaluation of similar structures; Mahmoodian and Alani (2013) and Fu and Kodikara (2022) considered the same limit states functions suggested by ASCE 15 (2017). However, the first study considered the effect of sulfide-induced erosion only, which is an unconservative evaluation, since it was proved in this study that chloride-induced corrosion plays a vital role in

diminishing the mechanical and geometrical properties of concrete and reinforcement. The second study assumed uniform corrosion and evaluated crack width likelihood using crack control factor limit state function, which does not consider the impact of the corrosion process on the cracking rate, and it is more about specifying the least amount of flexural reinforcement to maintain a 50 % likelihood of observing cracks of $0.254\ mm$ due to flexural loading. Other studies such as Phan et al. (2018), Wu and Wang (2022); Tang et al. (2022), and Marquez-Pe˜naranda et al. (2022) have considered the impact of chloride-induced corrosion on the reliability of RCSPs; however, it was assumed to occur uniformly in a constant rate based on random assumptions and without any consideration of the reduction in the mechanical properties of both concrete and reinforcement.

5.3. Consequences of Failure

Risk assessment of a structure under an anticipated hazard event responsible for a single or a combination failure mode requires two main components. The first component is the likelihood of failure modes to occur, which has been discussed previously, while the second component is the consequences associated with the occurrence of failure modes. Previous studies discussed in **Section 2.3** discussed different methods for evaluating the consequences, most of which are qualitative due to the high level of uncertainty in the impact factors. In this study, the consequences are evaluated monetarily while considering uncertainties in impact factors and they have been divided into two main parts depending on the impact factors and the entities that are liable for them. The first part is the direct cost, which is the cost liable by the authorities that own the structure and includes the cost of activities directly associated with retaining the structural integrity or extending the service life of the RCSPs. The second part is the indirect cost, which is the cost that affects surrounding communities indirectly because of service interruption and maintenance activities on the defective structure.

The direct cost was estimated using an alternative-based stepwise multilinear regression model. A pipe replacement alternative is associated with failure time or the ultimate level, while the cured-in-place liner (CIPP) is associated with service life or the serviceability level. Based on the acquired processed dataset explained in **Section 3.3.1**, regression analysis conducted on both alternatives shows a high coefficient of determination R^2 and high F_stat indicating good fitness and ability of the model in describing the variation in the response (cost in $\$/LF$) based on input impact factors, respectively after training and validation using 10-Fold cross-validation. Using estimated standard error σ, the predictive distributions of the direct cost of both alternatives at service and ultimate level were successfully estimated as shown in **Fig. 24** using Eq. 47. It is important to note that the direct cost of either alternative is not only specific to the diameter of the designated pipe as has been proposed by such studies such as Brown & Caldwell (1999) and Kaushal et al (2020); however, it is more controlled by the project conditions and associated cost on-site as manifested by Zhao & Rajani (2002). For example, excluding manhole repair from the direct cost of the CIPP alternative will reduce it by 22%, similarly, eliminating manhole replacement in the replacement alternative will reduce the direct cost by 2%. The variation in the reduction depends on the individual cost burden induced by the sole activity. The cost $\$/LF$ at service level is 8.7% less than the cost at ultimate, which is lower than what is expected by Kaushal et al. (2020). This is attributed to the selected diameter and pipe material used in the replacement alternative. For example, if the pipe under investigation is 32 $inch$ in diameter, the difference will increase to 12.4%. This makes the CIPP alternative more cost-effective for small diameters compared to large ones as accredited by Kaushal et al. (2020). Similarly, if the decision-makers opt to use HDPE pipe or RCP pipe instead of PVC pipe, the cost difference will rise by 25.6% approximately. Other factors such as inspection cost, manhole replacement, and traffic control,

positively add to the cost at different levels. Compared to previous studies by Brown & Caldwell (1999) Jung & Sinha (2007), and Kaushal et al. (2020), these models provide a better explanation of the variability of the direct cost, which makes it suitable in risk assessment practice.

In the indirect cost, four different categories were considered including traffic delay, vehicle operating, noise pollution, and pavement reduction value were analyzed using Monte-Carlo simulation considering uncertainties in controlling variables. The Pavement reduction value was excluded from the CIPP alternative since it doesn't require excavation. The outcomes of the Monte-Carlo simulation are normal predictive distributions of the combination of indirect cost categories. These distributions were added to the predictive distribution of direct costs to obtain the total cost or consequences. Based on the simulation results, the mean and standard deviation of indirect costs for CIPP alternatives are $61,718. 54 and $21,992.41 respectively, while they are $305,477.67 and $82,354 for replacement alternatives. The Average cost breakdown is shown in **Table 23**. The first thing to observe is that the average ratio of the indirect costs to the total cost of both CIPP and replacement is 5.96% and 22.23%, respectively. Pavement reduction value has the highest contribution to the indirect cost of the replacement alternative since the age of the pavement exceeds the mean service life of pavement shown in **Table 14**, which means that pavement adjacent to the trench requires a complete reinstatement. The noise pollution cost has the least contribution to the indirect cost of the CIPP alternative, while has the highest contribution to the indirect cost of the replacement alternative because of the difference in the noise levels induced by construction equipment and the project duration. The vehicle operating cost is 1.88 higher than the traffic delay cost for both alternatives, which is attributable to the significant increase in the operational cost when the speed drops from the it is normal values [35,40,45,50,55] mph to the speed at the working zone, which is assumed to be 20 mph.

Table 23. The average costs breakdown of the indirect costs.

	Cured In Place Liner (CIPP)	Replacement	$Indir\_Cost/Total\_Cost$
Pavement reduction value	0	$119,544.82	0%, 8.7%
Traffic delay cost	$17,749.73	$35,512.08	1.71%, 2.58%
Vehicle operating cost	$33,615.20	$67,266.90	3.24%,4.9%
Noise pollution cost	$10,353.6	$83,153.85	1.00%, 6.1%

All previous studies on indirect costs such as Ormsby (2009), Matthew & Allouche (2010), Matthew et al (2014), and Kaushal et al. (2020) proved that the indirect cost of trenchless technology is significantly lower than the traditional replacement method and agree with results acquired by this study. However, variation in the indirect cost contribution is observed among all studies also with results obtained in this study. This variation is related to the categories of indirect costs adopted by each study and the input parameters ranges. This study tried to overcome the limitations in data availability and overcome bias evaluations by considering uncertainties and conducting simulations.

5.4. Risk Assessment

In this study, three different risk assessment approaches are suggested. The first approach is simply the multiplication of both likelihood and consequences, which allows risk monetary interpretation as shown in **Fig. 27**. It is observable that the average risk increases linearly from the point where the likelihoods become nonzero, which are 6 and 6.5 years up to the point where they reach their threshold values, which are 15 and 37 years for service and ultimate levels, respectively. Also, the variation of risk value at a certain age depends on the likelihood at that age and the

consequences, too; for example, at early ages, the risk values at both levels have the least variations since the likelihoods are close to zero, while at higher ages such as 20 and 60 years, the corresponding risk values exhibit the largest variation at service and ultimate level, respectively since the likelihoods reach their highest value leaving the variation to be explained by the consequences.

The second approach defines risk in classes based on a set of rules in a decision matrix. Risk classification at either level was done based on five different classes (Low, Low to Moderate, Moderate, High, and Very High). Risk classification at both levels over time is shown in **Fig. 30**. For service and ultimate levels, the risk classification remains in the Moderate class for a period up to 9 and 22 years before it abruptly rises to the High class, which is sustained until 13 and 30 years, respectively. At the end of service life and failure time, the risk class is "Very High". As mentioned in **Chapter 3**, the risk classification depends on both likelihoods and consequences ratio classes. Since the likelihood changes from zero to one over time, risk classification at early ages and at ages close to the service life or failure time is more controlled by the consequences ratio. According to **Fig. 30**, both levels produce a "Very High" consequences class, which entails "Moderate", "High", and "Very High" risk classes. Despite the first approach gives more appealing representation of risk in terms of dollar values, it doesn't reflect any useful meaning when it comes to decision-making practices. For example, saying that the risk is $500,000 in 30 years is not informative enough compared to saying that the risk is "Very High". Additionally, the first approach might be misleading at some point; for example, at a certain year, a pipe might have a likelihood of failure of 0.1 and consequences of failure of $500,000, while another pipe is approaching failure with a likelihood close to 0.9, but with consequences of failure of only $50,000. Both cases provide approximately the same risk value; however, a possible decision-

maker perspective is to give higher priority to the second pipe; therefore, using the first approach may not be sufficient to support decisions.

As discussed in **Chapter. 2**, fuzzy principles are widely used in engineering practices including risk assessment as they allow partial knowledge interpretation and mimic human thinking. The proposed model moves one step further and allows continuous updating of the fuzzy inference parameters to match decision-makers needs. The training process starts with a structural learning process, in which the number of fuzzy sets and intervals for likelihood, consequences, and risk are defined based on decision-makers preferences, which are adopted from the risk matrix used in the second approach. The second step is supervised learning, which includes the integration of both knowledge-based learning and parameter learning processes. It starts with initial parameter values and then consecutive forward and backpropagation processes over batches of training data until the training error reaches a threshold value. The model was trained using stochastic gradient descent (SGD) algorithms with a total number of epochs of 811. Results include optimized membership function parameters and rule weights that give the least possible training error as shown in **Table 19** and **Fig. 31**. It is obvious that the changes in the membership functions (i.e., represented by solid lines in **Fig. 32**) are at different levels; for example, the "Low" membership functions of the likelihood, consequences ratio, and risk moved significantly to the right, while the "Moderate" and "Very High" membership functions of the likelihood didn't change significantly. This is mainly controlled by the initial parameters' values and how close they are to the true values and the added Lagrange constraints that maintain proper interactions among membership functions.

Finally, the neuro-fuzzy model was able to learn the true rules of the risk matrix and their corresponding weights as shown in **Fig. 32**. These weights vary approximately from 0.7 to 0.97,

which are significantly affected by the learned membership functions parameters and by the training data. It is recognized that the rules leading to "Low" and "Very High" risk classes have the lowest weights compared to other rules, which is attributable to interaction among fuzzy sets membership functions in all domains; for example, in the first rule, the Low membership functions in all domains shifted significantly to the left side and have a reduced standard deviation; therefore, the membership values are expected to drop significantly beyond the means of these fuzzy sets, which leads to reduction in the estimated weights related to this rule according to the procedure explained in **Fig. 17**.

Additional effort in this study is to enhance the performance of the model during the training process. Originally, the model was trained using the SGD algorithm with the total number of epochs equal to 811; therefore, to reduce the computational cost, other optimization algorithms have been tested as exemplified in **Section 4.4.3.3**. In general, all tested algorithms were able to reach the desired training error value, which is 0.0005, but with significant differences in the training epochs. According to **Table 18**, Adam optimizer gives a tremendous improvement to the training process among other optimizers as only requires 19 epochs to reach the desired error level. Adam optimizer estimates the $\boldsymbol{stepsize}$ in Eq. 70 using the moving average $\widehat{\boldsymbol{m}}_t$ and its square (i.e., uncentered variance) $\widehat{\boldsymbol{v}}_t$ as shown in Eqs. A47 & A48 in Appendix II. During the initial stages, $\widehat{\boldsymbol{m}}_t$ increases exponentially at a higher rate than $\widehat{\boldsymbol{v}}_t$ which causes an increase in the $\boldsymbol{stepsize}$ until reaching close to the global minima of the objective function in the parameters' space where the $\widehat{\boldsymbol{m}}_t$ reduces, while the $\widehat{\boldsymbol{v}}_t$ remains constant and results in a reduction in the $\boldsymbol{stepsize}$. Adagrad has the lowest performance among adaptive optimization algorithms (i.e., Adam, Adagrad, and Adelta) since it scales the learning rate by the square root of the gradient summation (see Eq. A51 in **Appendix II**), which causes a continuous reduction in the $\boldsymbol{stepsize}$. Replacing the square root

with only gradient summation mitigates the reduction in $\boldsymbol{stepsize}$ and improves the performance as suggested in Adelta optimizer. The momentum optimizer is an extension of the SGD algorithm that allows the $\boldsymbol{stepsize}$ to increase every training batch by inducing momentum term ρ as shown in Eq. A51 in **Appendix II** if the gradient maintains the same direction. Despite that the momentum optimizer expedites the training process as shown in **Table 20**, it can result in oscillation near the global minimum. This can be avoided by using the NAG optimizer, which evaluates the gradient based on the overlooked value of the parameter, $\boldsymbol{w_{overlooked}}$ as shown in Eqs. A52 & A53 in **Appendix II.** However, according to **Table 20**, there is no difference between NAG and momentum, which indicates that there is no oscillation near the global minima.

After showing the ability of the neuro-fuzzy system to learn the parameters of the FIS, in addition to training on different optimization algorithms to enhance the performance, the model's ability to accommodate future scenarios related to changes in the FIS to accommodate decision-makers needs was evaluated and their results are shown in **Table. 21 & 22**. The first scenario is related to adjusting the weights of part of the learned rules to 0.5, which results in insignificant changes in the parameters from the control state. Based on **Fig. 31**, all learned rules that have the same consequent (i.e., risk level) have almost identical weights; therefore, when applying Eq. 69 to the modified rule weights, the outcome will be the same as the control state since it is mainly controlled by the rule that exhibits the highest weight (not the adjust one). As a result, the same error will propagate backward, leading to the same parameter obtained in the control state. In the second scenario, the fuzzy sets of domains of consequences have changed. This has led to changes in the parameters of membership functions and the consequences. The "Low" fuzzy sets membership function has a lower mean and standard deviation to accommodate the narrowing in the domain; however, the "Low-Moderate" and "High" membership functions have higher mean

and standard deviation to accommodate the expansion in their domains. The "Very High" membership function showed a higher inflection point as the lower bound of this fuzzy set increased from 0.8 to 1.0. A similar trend to the second scenario was observed in the third one but with a lower impact. The reason behind this is that the amount of error propagates to the second layer node where the consequences membership functions are defined is higher than the error in the fifth layer, which means that for similar changes in the domains of fuzzy sets of the inputs and outputs, the degree of parameter changes will be higher in the input's membership functions relate to the output's membership functions. This indicates that the membership functions of the likelihood and consequences ratio are more sensitive in the decision-making process compared to the risk. Additionally, it is observed that whether the changes are taking place at either the input or output levels, the changes will only affect the corresponding fuzzy sets membership functions, which reflects independence among inputs and outputs.

Using the trained model, risk at both levels through time was estimated through the feedforward process of the neuro-fuzzy model. The feedforward process is simply the set of fuzzy operations used in the FIS system, which map crisp inputs (i.e., likelihood and consequences) to defuzzied crisp output (risk). **Fig. 34** shows the variation in risk at both levels over time and it is expressed in a continuous variable from zero to one, which represents different risk classes as explained in **Table 18**. At the service level, the risk is close to 0.5 and maintains this value for 10 years, beyond which it starts to increase linearly at different rates until reaching a mean value of 0.86. The behaviour is the same at the ultimate level but with different values. First, risk maintains a value of 0.43 for 16 years, before it starts to increase linearly at different rates until reaching a mean value of 0.77 at year 37. At both levels, the predicted risk values over all time steps belong to the same risk classes presented in **Fig. 30** and obtained from the risk matrix approach, which

reflects the efficiency and the accuracy of the neuro-fuzzy model in learning the true parameters and rules when trained on a dataset generated from the same matrix used in the risk matrix approach. It is also observed that the variation of risk values at a specific time is not uniform, which can be best described by the outputs of the fourth layer (i.e., the output of the implication and aggregation FIS operations) as shown in **Fig. 38**.

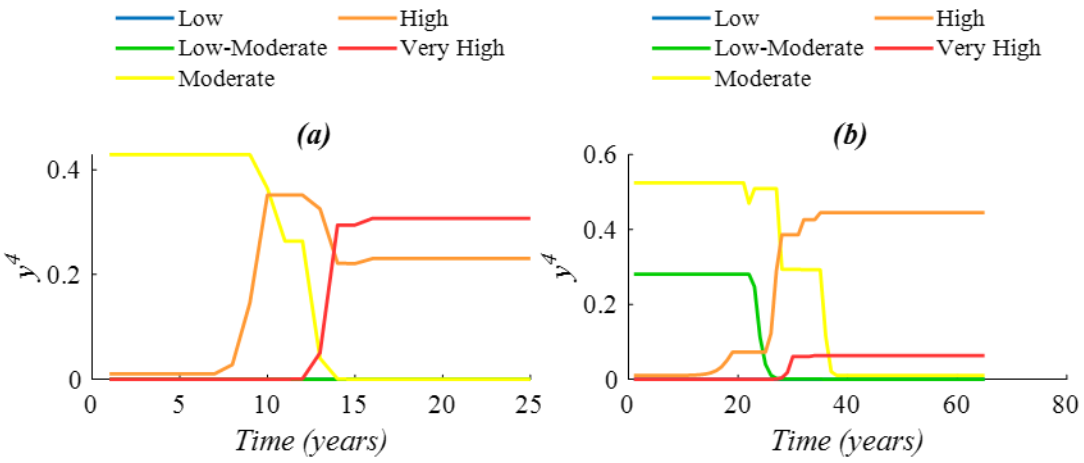

Fig. 36. Outputs of the fourth layer over time; **(a)** Service level; **(b)** Ultimate level.

The mean outputs of the fourth layer y^4 at service level show a dominance of the "Moderate" risk class relative to other classes within the first 10 year while they show almost a mutual contribution of both "High" and "Very High" risk classes beyond the year 15. On contrary, y^4 at ultimate level give a close contribution of "Low-Moderate" and "Moderate" classes during the first 16 years and a dominance of the "High" class beyond the year 37. This reflects a significant correlation between the variation in inputs (i.e., variation in the consequence ratio) and y^4. Whenever a certain fuzzy set dominates the contribution, the defuzzification result will always be within its domain; therefore, there will be insignificant variation in risk values. This would justify

insignificant variation in risk values within initial and final time interval of service and ultimate level, respectively, despite the variation in the consequence ratio.

Major differences among the three approaches are observed in **Fig. 28**, **Fig. 30**, and **Fig. 34**. At early ages the multiplication approach gives risk equal to zero while both the risk matrix approach and the neuro-fuzzy model give risk equal to "Moderate" and some random values, respectively. Similarly at ages beyond the service life and the failure time, the multiplication approach gives risk equal to one while both the risk matrix approach and the neuro-fuzzy model give risk values of "Very High" and some random values, respectively. This is attributed to the dependency of the risk matrix approach and the neuro-fuzzy model on the knowledge base or decision rules rather than mathematical operation. Additionally, the output of the neuro-fuzzy model does not only depend on the decision rules or always be zero or one at the early age or beyond the lifetime, respectively, but also on the values of the consequence ratio. For example, because the mean of the consequences ratio of the replacement alternative is higher than the CIPP, the risk output is higher at the failure time than at the end of service life although both risk values belong to "Very High" class due to soft transitions among classes. This conclude that the simple multiplication approach is suitable to use when there are not any decision rules; likelihood and consequences are accurately predicted; or for comparison between rehabilitation and replacement alternatives. Both the risk matrix approach and the neuro-fuzzy system are suitable for decision making such as prioritization of rehabilitation or replacement; however, the neuro-fuzzy system gives a better performance as it allows prioritization among pipes belong to the same risk class, which makes resource allocation more efficient and practical. A summary of different properties of the three risk approaches are provided in **Table. 24.** `

Table 24. Comparison among proposed risk models based on different criteria.

Criteria	Simple Multiplication	Risk Matrix	Neuro-Fuzzy
Decision-making	Not recommended	Recommended	Recommended
Interpretability	Monetary/scale	Qualitative	Scale
Alternative comparison	Recommended	Not recommended	Not recommended

Conclusion

In this research, three different topics were discussed and combined for risk assessment of the sewer main. The first topic is related to the reliability analysis of sewer main against service loss or failure, while the second and third topics are related to the evaluation of consequences of failure and proposing a novel risk assessment model. All these topics were demonstrated through a case study.

The conclusion related to the reliability analysis is:

- At the service level, wall thickness loss represents the least detrimental limit state functions compared to crack width and bond strength loss limit states. This suggests that the serviceability of RCSPs is more affected by chloride-induced corrosion rather than sulphide-induced corrosion.
- At the ultimate level, the rates of failure given by all limit states except the radial tension are consistent. The rates of failure are highly affected by the residual geometrical and mechanical properties of reinforcement and concrete.
- The chloride-induced corrosion has the highest impact on the compressive strength; therefore, causing a significant drop in the flexural, shear, and radial tension capacities.
- Based on the parametric study, the expansion coefficient of the corrosion product, wire diameter, and cover thickness play a vital role in controlling the propagation of crack width. In addition to the bond strength.
- A reliability block diagram (RBD) has been used to obtain the overall reliability at both service and ultimate levels assuming parallel and series configurations of limit states, respectively. The parallel configuration used at the service level exaggerates the service

life; therefore, for best practice, it is recommended to use the most detrimental limit state function to find the service life.

Possible future research directions encompass conducting extended experiments to explore sulfide erosion and chloride corrosion in settings resembling sewer environments. Additionally, conducting further experiments to investigate the progression of chloride corrosion during the late cracking stage and its susceptibility to weather conditions is imperative. Moreover, in-depth investigations into pitting corrosion, including its distribution during the initial and later stages of cracking, as well as its impact on the mechanical and microstructural properties of reinforcements, could help address numerous uncertainties within this framework.

The conclusion related to the consequences evaluation model is:

- Direct cost models related to cured-in-place liners and pipe replacement showed high R^2 and F_stat indicating good fitness and ability of the model in describing the variation in the direct cost based on impact factors.
- The proposed models show a high dependency on the diameter and material. The difference between both alternatives reduces as the diameter of the defective pipe increases or the material of the new pipe matches the old one (i.e., RCSP). Other impact factors have been included in the analysis and proved their contribution to the direct cost at different levels.
- For indirect costs, the results of the Monte-Carlo simulation show that the mean of indirect costs associated with cured-in-place liner is significantly lower than the mean associated with replacement alternatives.

- The pavement reduction value as a result of replacement is mainly controlled by the age of the pavement at the time of restoration; the noise-associated cost provides the main contribution to the indirect cost of the replacement alternative, while the least contribution is the cured-in-place liner. Finally, the difference between the speed at the working zone and the off-working zone is what significantly impacts the vehicle operating cost.

Possible improvement in predicting the consequences of failure includes developing a Bayesian regression model similar to the stepwise regression model developed in this study that allows decision-makers to interpret their belief in the model.

The conclusion related to the risk evaluation model is:

- By integrating the previous topics, both risk at service and ultimate level can be evaluated qualitatively or quantitatively. The first risk assessment approach allows the risk to be interpreted monetarily or on a scale measure, while the second risk assessment allows qualitative risk assessment. The proposed fuzzy system presents risk on a scale from zero to one, which reflects the qualitative classes of risk.
- Through a training simulation, the neuro-fuzzy system showed high ability in learning decision rules, their weights, and membership functions parameters, which could not be learned in the ordinary FIS system while satisfying the fuzzy logic through Lagrange constraints, in addition to accommodating changes in the FIS system as explained through potential scenarios.

- Compared to many optimization algorithms, the Adam optimizer gives the highest training performance to the neuro-fuzzy system even with a small learning rate by reducing the number of training epochs.
- Based on the acquired results, the simple multiplication model is more suitable in cases such as missing the decision rules or for comparison between rehabilitation and replacement alternatives. However, since the risk matrix and the neuro-fuzzy approaches depend mainly on the decision rules and less on the exact values of likelihood and consequences, they are more suitable for decision-making and prioritizing actions.
- Compared to the risk matrix approach with the neuro-fuzzy system, the latter shows higher interpretability than the risk matrix approach through soft transitions among classes, which allows better decision-making practice and prioritization of action on pipes that belong to the same risk class.

A future work related to risk assessment is to demonstrate the application of the neuro-fuzzy system through training on a genuine dataset related to different sewer pipe threats and failure modes collected using the suggested framework described earlier.

The validation of reliability analysis results and the consequences of failure models can be achieved by verifying the accuracy of input data to accurately represent the characteristics of the real-world system or through comparisons with similar case studies. The validation of the neuro-fuzzy system can be conducted after training the model on a genuine dataset. The model can then be tested on various potential case studies and validated based on feedback from experts to ensure alignment with their knowledge and expertise.

Appendix

Appendix I. Complementary Equations for Reliability Analysis

Corrosion Current Density i_{corr} Parameters

$$\left.\begin{aligned} i_{o,a} &= 3 * 10^{-2}\, e^{9500\left(\frac{1}{298}-\frac{1}{T}\right)} \\ i_{o,c} &= 1 * 10^{-2}\, e^{2612\left(\frac{1}{T}-\frac{1}{298}\right)} \\ \Delta E_e(T) &= 525 + 1.44\, T \end{aligned}\right\} \tag{A1}$$

$$\left.\begin{aligned} \beta(t) &= 143.79 - 54\ {}^{w}/_{c} + 0.018\, R && t = t_{in} \\ \beta(t) &= \beta_1 + (0.78 - 0.92\ {}^{w}/_{c} + 0.00012R)t && t_{in} < t \le t_1 \\ \beta(t) &= \beta(t_1) && t_1 < t \le t_2 \end{aligned}\right\} \tag{A2}$$

$$R_e = (75605\ {}^{w}/_{c} - 106{,}228)e^{\left(-0.441\ Cl - 7.7213\ St + 2889\left(\frac{1}{T}-\frac{1}{303}\right)\right)} \tag{A3}$$

$$St\,\frac{\gamma_1\ RH}{\gamma_2\ RH + \gamma_3\ RH} \tag{A4}$$

$$\gamma_1 = (2.914\ {}^{w}/_{c} - 2.584)\ 10^{-3}\, T_c - 0.20\, {}^{w}/_{c} + 0.165 \tag{A5}$$

$$\gamma_2 = (2.907\ {}^{w}/_{c} - 0.001145\ T_c + 1.5594 * 10^{-5}\, T_c^3 + 4.45) * 10^{-3} \tag{A6}$$

$$\gamma_3 = (2.158\ {}^{w}/_{c} - 3.28) * 10^{-3}\, T_c - 0.33\ {}^{w}/_{c} + 0.32 \tag{A7}$$

Radial Stress at The Interface at the Uncracked Stage

$$U_{rs} = \frac{-2r_s \pm \sqrt{4{r_s}^2 - 4(\alpha-1)(2r_s\, p_{avg}(t) - p_{avg}(t)^2)}}{2} \tag{A8}$$

$$\varepsilon_{rs} = U_{rs} r_s \tag{A9}$$

$$\sigma_{r,rs} = E_C \varepsilon_{rs} \left(\frac{c^2 - {r_s}^2}{c^2 + {r_s}^2}\right) \tag{A10}$$

$$\sigma_{t,rs} = \frac{{r_s}^2}{c^2 - {r_s}^2}\sigma_{r,rs}\left(1 - \frac{c^2}{r_s^2}\right) \quad \text{(A11)}$$

Radial Stress at The Interface at the Partially Cracked Stage

$${\sigma_{r,rs}}^{EL} = \frac{r_{cr}}{r_s} f_{ct} c_1 \quad \text{(A12)}$$

$${\sigma_{r,rs}}^{NL} = f_{ct}\left[\frac{a\, C_2 r_s}{2}\left(\frac{r_{cr}}{r_s} - 1\right)^2 + b\left(\frac{r_{cr}}{r_s} - 1\right)\right] \quad \text{(A13)}$$

$$C_2 = \frac{2\pi\varepsilon_{t,cr}}{n w_0} \quad \text{(A14)}$$

$$\sigma_{r,rs} = {\sigma_{r,rs}}^{EL} + {\sigma_{r,rs}}^{NL} \quad \text{(A15)}$$

Radial Stress at The Interface at the Fully Cracked Stage

$$\sigma_{r,rs} = f_{ct}\left[(aC_3 + b)\left(\frac{c_1}{r_s} - 1\right) - \frac{aC_2 r_s}{2}\left(\left(\frac{c_1}{r_s}\right)^2 - 1\right)\right] \quad \text{(A16)}$$

$$C_3 = \frac{2\pi\varepsilon_{t,cr} r}{n w_0} \quad \text{(A17)}$$

Tension Softening Model Parameters

The bilinear soft tension model consists of two parts; the two parts coincide when the ratio of total crack width w to the crack width at zero tensile strength w_0 equals to α and the percentage of residual tensile strength equals to β.

First branch tension softening

$$a = -\frac{1-\beta}{\alpha},\ b = 1 \quad \text{(A18)}$$

Second branch tension softening

$$a = -\frac{1-\beta}{\alpha},\ b = \frac{1-\beta}{\alpha} \tag{A19}$$

$$\begin{Bmatrix} \beta = 0.25 & f_{c0} = 30\ Mpa \\ \beta = 0.25 - 0.15(f_{c0} - 30) & f_{c0} > 30\ Mpa \end{Bmatrix} \tag{A20}$$

Moment, Shear, and Thrust Load

$$M_u = (1.3\ C_{mp} W_p + 1.3 C_{me}\ W_e + 1.3\ C_{mf}\ W_f + 2.17\ C_{mL1}\ W_{LL1} + +2.17\ C_{mL2}\ W_{LL2}) \frac{D_m}{2} \tag{A21}$$

$$N_u = 1.0\ C_{np} W_p + 1.0\ C_{ne}\ W_e + 1.5\ C_{nf}\ W_f + 1.3\ C_{nL1}\ W_{LL1} + 1.3\ C_{nL2}\ W_{LL2} \tag{A22}$$

$$V_u = 1.3\ C_{vp}\ W_p + 1.3\ C_{ve}\ W_e + 1.3\ C_{vf}\ W_f + 2.17\ C_{vL1}\ W_{LL1} + +2.17\ C_{vL2}\ W_{LL2} \tag{A23}$$

Reinforcement Ductility Loss Limits State Function

$$\begin{bmatrix} A_1 + A_2 & P_{max}(t) \le \frac{2r_s}{\sqrt{2}} \\ A_O - A_1 + A_2 & \frac{2r_s}{\sqrt{2}} < P_{max}(t) \le 2r_s \\ A_O & P_{max}(t) > 2r_s \end{bmatrix} \tag{A24}$$

$$A_0 = \pi r_s^2 \tag{A25}$$

$$b = 2\ P_{max}(t) \sqrt{1 - \left(\frac{P_{max}(t)}{2r_s}\right)^2} \tag{A26}$$

$$A_1 = 0.5 \left[\theta_1 (r_s)^2 - b \left| r_s - \frac{P_{max}(t)^2}{2r_s} \right|\right] \tag{A27}$$

$$A_2 = 0.5 \left[\theta_2 P_{max}(t)^2 - b \frac{P_{max}(t)^2}{2r_s}\right] \tag{A28}$$

$$\theta_1 = 2 \arcsin\left(\frac{b}{r_s}\right) \tag{A29}$$

$$\theta_2 = 2 \arccos\left(\frac{b}{2\ P_{max}(t)}\right) \tag{A30}$$

$$F_d = 0.8 + \frac{1.6}{d} \tag{A31}$$

$$F_c = 1 + \frac{2d}{D_{in}} \tag{A32}$$

$$F_{rt} = \frac{(3600 - D_{in})^2}{16.8 * 10^6} + 0.8 \tag{A33}$$

Appendix II. Back Propagation Algorithm

The goal of the back propagation algorithm is to find model parameters that minimize the objective function. For better presentation, the objective function in Eq.74 is divided into four different parts as shown in Eqs. A34, A35, A36, & A37; each part triggers a different purpose. For example, Eq. A34 is concerned with model predictions to be closer to the true values; Eqs. A35, A36, & A37 are concerned with satisfying the equality constraints related to membership functions for inputs and outputs. The subscriptions i and t denote the i^{th} instance in the t^{th} batch of training data.

$$E_{1_i} = \begin{Bmatrix} 0 & {y^5}_{l_i} \in R_j \wedge \hat{y}_i \in R_k, j = k \\ \left(upper\ bound_{R_j} - {y^5}_{l_i}\right)^2 & {y^5}_{l_i} \in R_j \wedge \hat{y}_i \in R_k, j > k \\ 2\left(upper\ bound_{R_k} - {y^5}_{l_i}\right)^2 & {y^5}_{l_i} \in R_j \wedge \hat{y}_i \in R_k, j < k \end{Bmatrix} \tag{A34}$$

$$E_{2_i} = \lambda_1 \left(1 - \sum_{k=1}^{S} \mu_k \left({y^5}_{l_i}\right)\right)^2 \tag{A35}$$

$$E_{3_i} = \lambda_2 \left(1 - \sum_{k=1}^{S} \mu_k \left({x^2}_1\right)\right)^2 \tag{A36}$$

$$E_{4_i} = \lambda_3 \left(1 - \sum_{k=1}^{S} \mu_k \left({x^2}_2\right)\right)^2 \tag{A37}$$

Layer V

The error at layer five δ^5.

$$\delta^5{}_i = \left(\frac{\partial E_{1_i}}{\partial {y^5}_{l_i}} + \frac{\partial E_{2_i}}{\partial {y^5}_{l_i}}\right) = \begin{cases} 0 & {y^5}_{l_{i_i}} \in R_j \wedge \hat{y}_i \in R_k, j = k \\ 2\left(upper\ bound_{R_k} - {y^5}_{l_i}\right) & {y^5}_{l_i} \in R_j \wedge \hat{y}_i \in R_k, j > k \\ 2\left(lower\ \ bound_{R_k} - {y^5}_{l_i}\right) & {y^5}_{l_i} \in R_j \wedge \hat{y}_i \in R_k, j < k \end{cases} + \lambda_1 \Big(1 -$$

$$\sum_{k=1}^{S} \mu_k\left({y^5}_{l_i}\right)\Big) \sum_{k=1}^{S} \frac{-1}{{d_{k_{t-1}}}^2}\left(c_{k_{t-1}} - {y^5}_{l_i}\right) e^{-\left(\frac{\left(c_{k_{t-1}} - {y^5}_{l_i}\right)^2}{2\,{d_{k_{t-1}}}^2}\right)} \quad \text{(A38)}$$

The parameters to be updated at this layer are the mean and standard deviation of output membership functions c_k and d_k, respectively. The error gradients with respect to both parameters are shown in Eqs. A39 & A40.

$$\frac{\partial E_i}{\partial c_k} = \delta^5 \frac{\partial y^5}{\partial c_k} = \begin{bmatrix} \frac{\partial E_{1_i}}{\partial {y^5}_{l_i}} & \frac{\partial E_{2_i}}{\partial {y^5}_{l_i}} \end{bmatrix} \begin{bmatrix} \frac{{y^4}_{k_i} d_{k_{t-1}}}{\sum_{k=1}^{K} {y^4}_{k_i} d_{k_{t-1}}} \\ \lambda_1\left(1 - \sum_{k=1}^{S} \mu_k\left({y^5}_{l_i}\right)\right) \frac{1}{{d_{k_{t-1}}}^2}\left(c_{k_{t-1}} - {y^5}_{l_i}\right) e^{-\left(\frac{\left(c_{k_{t-1}} - {y^5}_{l_i}\right)^2}{2\,{d_{k_{t-1}}}^2}\right)} \end{bmatrix} \quad \text{(A39)}$$

$$\frac{\partial E_i}{\partial d_k} = \delta^5 \frac{\partial y^5}{\partial d_k} = \begin{bmatrix} \frac{\partial E_{1_i}}{\partial {y^5}_{l_i}} & \frac{\partial E_{2_i}}{\partial {y^5}_{l_i}} \end{bmatrix} \begin{bmatrix} \frac{{y^4}_{k_i}\left(c_{k_{t-1}} \sum_{k=1}^{K} {y^4}_{k_i} d_{k_{t-1}} - \sum_{k=1}^{K} {y^4}_{k_i} c_{k_{t-1}} d_{k_{t-1}}\right)}{\left(\sum_{k=1}^{K} {y^4}_{k_i} d_{k_{t-1}}\right)^2} \\ \lambda_1\left(1 - \sum_{k=1}^{S} \mu_k\left({y^5}_{l_i}\right)\right) \sum_{k=1}^{S} \frac{-1}{{d_{k_{t-1}}}^3}\left(c_{k_{t-1}} - {y^5}_{l_i}\right)^2 e^{-\left(\frac{\left(c_{k_{t-1}} - {y^5}_{l_i}\right)^2}{2\,{d_{k_{t-1}}}^2}\right)} \end{bmatrix} \quad \text{(A40)}$$

Layer IV

The error at the fourth layer $\boldsymbol{\delta^4}$ is $[1\ x\ K]$ vector.

$$\boldsymbol{\delta^4}_i(k) = \frac{\partial E_{1_i}}{\partial {y^4}_{k_i}} = \frac{\partial E_{1_i}}{\partial {y^5}_{l_i}} \frac{\partial {y^5}_i}{\partial {y^4}_{k_i}} = \frac{\partial E_{1_i}}{\partial {y^5}_{l_i}} \frac{d_{k_{t-1}}\left(c_{k_{t-1}} \sum_{k=1}^{K} {y^4}_{k_i} d_{k_{t-1}} - \sum_{k=1}^{K} {y^4}_{k_i} c_{k_{t-1}} d_{k_{t-1}}\right)}{\left(\sum_{k=1}^{K} {y^4}_{k_i} d_{k_{t-1}}\right)^2} \quad \text{(A41)}$$

Layer III

. The error at the third layer $\boldsymbol{\delta^3}$ is $[1\ x\ J]$ matrix.

$$\boldsymbol{\delta^3}_i = \frac{\partial E_{1_i}}{\partial {y^3}_{j_i}} = \frac{\partial E_{1_i}}{\partial {y^5}_{l_i}} \frac{\partial {y^5}_i}{\partial {y^4}_i} \frac{\partial {y^4}_i}{\partial {y^3}_i} = \boldsymbol{\delta^4 w_{43}} \quad \text{(A42)}$$

The errors located in the consequent parts of the rules $\boldsymbol{\delta^4}$ are transferred to the corresponding antecedent parts by determining the amount of error allocated for each rule $\boldsymbol{\delta^3}(j)$ based on their firing strength. In this layer, there are no parameters to update.

Layer II

The first step is to define the controlling fuzzy set in the antecedent part of each rule in the third layer; there are two fuzzy sets per rule; one from each input. This can be determined using Eq. A43; the controlling fuzzy set is the fuzzy set that belongs to the group $\boldsymbol{l_j}$ and provides the least membership degree $min(\mu(x_1), \mu(x_2))$. $\boldsymbol{l_j}$ contains all fuzzy sets that constitute the antecedent part of the j^{th} and can be obtained from the third layer weights $\boldsymbol{w_{32}}$. Running Eq. A43 across all rules will result in a list of controlling fuzzy sets, one per each rule.

$$\boldsymbol{r}_i = Argmin_{n \in l_j}({y^2}_{n_i}) \tag{A43}$$

Since each fuzzy set contributes not just to one but multiple rules as shown in **Fig. 16**, a fuzzy set might control multiple rules. Therefore, the error propagated to an input fuzzy set is the summation of all errors from nodes in the third layer at which the fuzzy set is controlling as shown in Eq. A44. l_n is the set of rules that contains the n^{th} fuzzy set as one of its antecedents.

The error at the second layer $\boldsymbol{\delta^2}$ $[1\ x\ N]$ matrix.

$$\boldsymbol{\delta_i}^2(n) = \frac{\partial E_{1_i}}{\partial {y^2}_{n_i}} = \frac{\partial E_{1_i}}{\partial {y^5}_i} \frac{\partial {y^5}_i}{\partial {y^4}_i} \frac{\partial {y^4}_i}{\partial {y^3}_i} \frac{\partial {y^3}_i}{\partial {y^2}_{n_i}} = \begin{Bmatrix} \sum_{j \in l_n} \boldsymbol{\delta^3}_i(j) & n \in r_i \\ 0 & otherwise \end{Bmatrix} \tag{A44}$$

Finally, to update the mean and standard deviation a_n & b_n of membership functions, Eqs. A45 & A46 are used. Both equations consider the error transferred to the second layer $\boldsymbol{\delta_i}^2$ and the gradients of errors in Eq. A47 & A48 related to the constraint.

$$\frac{\partial E}{\partial a_n} = [\ \boldsymbol{\delta_i}^2(n) \quad 1] \begin{bmatrix} \frac{\partial {y^2}_{t_i}}{\partial a_n} \\ \left(\frac{\partial E_{3i}}{\partial a_n}\ or\ \frac{\partial E_{4i}}{\partial a_n}\right) \end{bmatrix} = [\ \boldsymbol{\delta_i}^2(n) \quad 1] \begin{bmatrix} e^{-\left(\frac{\left(x_i - a_{n_{t-1}}\right)^2}{{b_{n_{t-1}}}^2}\right)} \frac{2\left(x_i - a_{n_{t-1}}\right)^2}{{b_{n_{t-1}}}^2} \\ \lambda_2 (1 - \sum_{n=1}^{N/2} \mu_t(x_i)) \frac{1}{{b_{n_{t-1}}}^2} \left(a_{n_{t-1}} - x_i\right)^2 e^{-\left(\frac{\left(a_{n_{t-1}} - x_i\right)^2}{2\,{b_{n_{t-1}}}^2}\right)} \end{bmatrix} \tag{A45}$$

$$\frac{\partial E}{\partial b_n} = [\ \boldsymbol{\delta_i}^2(n) \quad 1] \begin{bmatrix} \frac{\partial {y^2}_{t_i}}{\partial a_n} \\ \left(\frac{\partial E_{3i}}{\partial a_n}\ or\ \frac{\partial E_{4i}}{\partial a_n}\right) \end{bmatrix} = [\ \boldsymbol{\delta_i}^2(n) \quad 1] \begin{bmatrix} e^{-\left(\frac{\left(x_i - a_{n_{t-1}}\right)^2}{{b_{n_{t-1}}}^2}\right)} \frac{2\left(x_i - a_{n_{t-1}}\right)^2}{{b_{n_{t-1}}}^2} \\ \lambda_2 (1 - \sum_{n=1}^{N/2} \mu_t(x_i)) \frac{-1}{{b_{n_{t-1}}}^3} \left(a_{n_{t-1}} - x_i\right)^2 e^{-\left(\frac{\left(a_{n_{t-1}} - x_i\right)^2}{2\,{b_{n_{t-1}}}^2}\right)} \end{bmatrix} \tag{A46}$$

$$\boldsymbol{stepsize}_t = alpha\ \frac{\widehat{\boldsymbol{m}_t}}{\sqrt[2]{\widehat{\boldsymbol{v}_t}}+\varepsilon} \tag{A47}$$

$$\widehat{\boldsymbol{m}}_t = \frac{\left(B_1\widehat{\boldsymbol{m}}_{t-1}+(1-B_1)\left(\frac{\partial \boldsymbol{E}}{\partial \boldsymbol{w}}\right)\right)}{1-B_1^t} \tag{A48}$$

$$\widehat{\boldsymbol{v}}_t = \frac{\left(B_2\widehat{\boldsymbol{v}}_{t-1}+(1-B_2)\left(\frac{\partial \boldsymbol{E}^2}{\partial \boldsymbol{w}}\right)\right)}{1-B_2^t} \tag{A49}$$

$$\boldsymbol{stepsize}_t = \gamma\frac{1}{\sqrt[2]{\sum_{t=1}^{t-1}\frac{\partial \boldsymbol{E}}{\partial \boldsymbol{w}}+\varepsilon}} \tag{A50}$$

$$\boldsymbol{stepsize}_t = \rho\boldsymbol{stepsize}_{t-1} + \gamma\frac{\partial \boldsymbol{E}}{\partial \boldsymbol{w}} \tag{A51}$$

$$\boldsymbol{w}_{\boldsymbol{overlooked}} = \boldsymbol{w}_{t-1} \mp \boldsymbol{stepsize}_{t-1} \tag{A52}$$

$$\boldsymbol{stepsize}_t = \gamma\boldsymbol{stepsize}_{t-1} + alpha\frac{\partial \boldsymbol{E}}{\partial \boldsymbol{w}_{\boldsymbol{overlooked}}} \tag{A53}$$

References

AASHTO (American Association of State Highway and Transportation Officials). 2019. "AASHTO LRFD bridge design specifications." Washington, DC: American Association of State Highway and Transportation Officials.

AASHTO CSDIM (American Association of State Highway and Transportation Officials). 2020. "Culvert and Storm Drain System Inspection Guide". AASHTO CSDIM. 555 12th Street NW, Suite 1000, Washington, DC. ISBN: 978-1-56051-720-7.

Abuhishmeh, K. S. 2019. "Service life prediction and risk analysis of reinforced concrete gravity flow pipes using reliability theory." Master's dissertation, Dept. of Civil Engineering, Univ. of Texas at Arlington. https://www.proquest.com/dissertations-theses/service-life-prediction-risk-analysis-reinforced/docview/2314065385/se-2

Abuhishmeh. K. S. & Hojat Jalali.H. 2023. "Reliability Assessment of Reinforced Concrete Sewer Pipes under Adverse Environmental Conditions: Case Study for the City of Arlington, Texas." Journal of Pipeline Systems Engineering and Practice. 14(2). https://doi.org/10.1061/JPSEA2.PSENG-1406

ACI PRC 439.5. 2018. Comprehensive Guide for the Specification, Manufacture and Construction Use of Welded Wire Reinforcement. ACI 439.5R-18. Farmington Hills, MI: ACI.

ACPA (American Concrete Pipe Association). 2017. "LRFD fill height tables for concrete pipes." ACPA, Irving, TX.

Ahmad, S. 2003. "Reinforcement corrosion in concrete structures, its monitoring and service life prediction—a review. Cement and concrete composites". 25(4-5): 459-471. https://doi.org/10.1016/S0958-9465(02)00086-0

Alani, A. M., and A. Faramarzi. 2015. "Predicting the probability of failure of cementitious sewer pipes using stochastic finite element method." Int.J. Environ. Res. Public Health 12 (6): 6641–6656. https://doi.org/10 .3390/ijerph120606641.

Almeida, M. D. C., Covas, D., & García Beceiro, P. M. 2015. Rehabilitation of sewers and manholes: technologies and operational practices. http://hdl.handle.net/10251/54141

Altarabsheh, A., Kandil, A., & Ventresca, M. 2018. New multiobjective optimisation approach to rehabilitate and maintain sewer networks based on whole lifecycle behavior. Journal of Computing in Civil Engineering, 32(1): 04017069. https://doi.org/10.1061/9780784479827.208

American Concrete Pipe Association ACPA. 2023. "Why Concrete Pipes?". https://www.concretepipe.org/why-concrete-pipe

Amin Soltanianfard. M., Abuhishmeh, K., & Hojat Jalali, H. 2023. "Sustainable Concrete Made with Wastewater at Different Stages of Filtration." Constr. Build. Mater. 409: 133894. https://doi.org/10.1016/j.conbuildmat.2023.133894.

Anbari, M. J., Tabesh, M., & Roozbahani, A. 2017. “Risk assessment model to prioritize sewer pipes inspection in wastewater collection networks.” Journal of environmental management, 190: 91-101. https://doi.org/10.1016/j.jenvman.2016.12.052

Andrew J. Wimsatt, Carlos M. Chang-Albitres, Paul E. Krugler,Tom Scullion, Tom J. Freeman, and Maria B.Valdovinos 2009. “Considerations for rigid vs. Flexible pavement designs when allowed as alternate bids: technical report (Report 0-6085-1)”. Texas Department of Transportation and the Federal Highway Administration.

ASCE. 1998. Standard practice for direct design of buried precast concrete pipe using standard installations (SIDD). Reston, VA: ASCE.

ASTM (American Society for Testing and Materials). 2013. "Standard Specification for Steel Wire and Welded Wire Reinforcement, Plain and Deformed, for Concrete." ASTM I A1064 / A1064M-10e1, 100 Barr Harbor Drive, PO Box C700, West Conshohocken, PA 19428-2959. United States, DOI: 10.1520/A1064_A1064M-10E01.

ASTM (American Society for Testing and Materials). 2015. "Standard Practice for Calculation of Corrosion Rates and Related Information from Electrochemical Measurements." ASTM G102-89 100 Barr Harbor Drive, PO Box C700, West Conshohocken, PA 19428-2959. United States, DOI: 10.1520/G0102-89R15E01

ASTM (American Society for Testing and Materials). 2016. "Rehabilitation of Existing Pipelines and Conduits by the Inversion and Curing of a Resin-Impregnated Tube" ASTM F1216 − 16, 100 Barr Harbor Drive, PO Box C700, West Conshohocken, PA 19428-2959. United States, DOI: 10.1520/F1216-22

ASTM (American Society for Testing and Materials). 2022. "Standard Practice for Inspection and Acceptance of Installed Reinforced Concrete Culvert, Storm Drain, and Storm Sewer Pipe ". ASTM C1840/C1840M. , 100 Barr Harbor Drive, PO Box C700, West Conshohocken, PA 19428-2959. United States. DOI: 10.1520/C1840_C1840M-22

ASTM (American Society for Testing and Materials). 2022. "Standard Specification for Reinforced Concrete Culvert, Storm Drain, and Sewer Pipe." ASTM C76, 100 Barr Harbor Drive, PO Box C700, West Conshohocken, PA 19428-2959. United States, DOI: 10.1520/C0076-22.

AWWA (American Water Work Association). 2010. Risk and Resilience Management Of Water And Wastewater Systems. AWWA J100. Denver, CO

AWWA (American Water Work Association). 2014. "Rehabilitation of Water Main: Manual of Water Practice" Denver, CO 80235 USA; AWWA

Beakley, J., DelloRusso, S. J., & Takou, M. 2020. "Indirect and Direct Design Methods for Design of Reinforced Concrete Pipe." Transportation Research Record, 2674(9), 575-585. https://doi.org/10.1177/0361198120930231

Benbachir, M., Chenaf, D., & Cherrared, M. 2022. "Fuzzy-FMECA Decision-Making Tool for Assessment and Analysis of Performance of Urban Sewerage Networks." Journal of Pipeline

Systems Engineering and Practice. 13(1): 04021078. https://doi.org/10.1061/(ASCE)PS.1949-1204.0000585

Bhargava, K., Ghosh, A. K., Mori, Y., & Ramanujam, S. 2007. "Corrosion-induced bond strength degradation in reinforced concrete—Analytical and empirical models. " Nuclear Engineering and Design. 237(11): 1140-1157. https://doi.org/10.1016/j.nucengdes.2007.01.010

Brown and Caldwell. 1999. Unlined concrete sewer assessment. Draft Task Memorandum 1/2, submitted to the City of Phoenix. (with permission). Phoenix, AR, U.S.A.

Canon. G. 2022. "Broken sewer line spills millions of gallons of waste into streets of California city". THEGURDIAN.COM. January/03/2022.

City of Mesquite. 2022. "South Mesquite sewer main failure". https://www.cityofmesquite.com/CivicAlerts.aspx?AID=2076

Coccia, S., Imperatore, S., & Rinaldi, Z. 2016. "Influence of corrosion on the bond strength of steel rebars in concrete." Materials and structures. 49(1): 537-551. https://doi.org/10.1617/s11527-014-0518-x

Corbisier. C. 2003. "Public Roads". 67(1).US. Department of Transportation, Federal Highway Administration. https://highways.dot.gov/public-roads/julyaugust-2003/living-noise.

Coronelli, D. 2002. "Corrosion cracking and bond strength modeling for corroded bars in reinforced concrete." Structural Journal. 99(3): 267-276. https://doi.org/10.14359/11910

Cuglietta. M. 2023. "45,000 gallons of wastewater leaked into a SC neighborhood after structural failure". POSTANDCOURIER.COM. February/14/2023.

Davis, P., and D. Marlow. 2008. "Asset management: Quantifying economic lifetime of large-diameter pipelines." J. Am. Water Works Assoc. 100 (7): 110–119. https://doi.org/10.1002/j.1551-8833.2008.tb09680.x.

Den Uijl, J. A., & Bigaj, A. J. 1996. "A bond model for ribbed bars based on concrete confinement. " HERON-ENGLISH EDITION. 41(3): 201-226. http://resolver.tudelft.nl/uuid:909c3422-9e78-4648-9a5a-566a4473f069

Du, Y. G., Clark, L. A., & Chan, A. H. C. 2005. "Residual capacity of corroded reinforcing bars." Magazine of Concrete Research. 57(3): 135-147. https://doi.org/10.1680/macr.2005.57.3.135

Duc, D. M., Hoang, N. D., & Nguyen, L. H. 2006. "Lagrange multipliers theorem and saddle point optimality criteria in mathematical programming." Journal of mathematical analysis and applications, 323(1), 441-455. https://doi.org/10.1016/j.jmaa.2005.10.038

Duchi, J., Hazan, E., & Singer, Y. 2011. "Adaptive subgradient methods for online learning and stochastic optimization. Journal of machine learning research". 12(7). 2121-2159. http://jmlr.org/papers/v12/duchi11a.html

Ebrahimi, M., and H. Hojat Jalali. 2022a. “Automated condition assessment of sanitary sewer pipes using LiDAR inspection data.” In Proc., UESI/ ASCE Pipelines 2022 Conf. Reston, VA: ASCE.

Ebrahimi, M., and H. Hojat Jalali. 2022b. “The spatial variability in condition assessment of reinforced concrete sanitary sewer pipes (RCSSPs).” In Proc., 2022 Tran-SET Conf. Reston, VA: ASCE.

Ebrahimi, M., Jalali, H. H., & Sabatino, S. 2023. “Probabilistic condition assessment of reinforced concrete sanitary sewer pipelines using LiDAR inspection data.” Automation in Construction, 150: 104857. https://doi.org/10.1016/j.autcon.2023.104857.Elmasry, M., Hawari, A., & Zayed, T. 2017. Cost benefit analysis for failure of sewer pipelines. http://dx.doi.org/10.1051/matecconf/201712008006

Elsawah, H., Guerrero, M., & Moselhi, O. 2014. "Decision support model for integrated intervention plans of municipal infrastructure." In proceeding of International Conference on Sustainable Infrastructure, California, United States..

Federal Highway Administration (FHWA). 2000. “Highway Economic Requirements System: Technical Report”. URL : https://rosap.ntl.bts.gov/view/dot/58541

Federal Highway Administration (FHWA). 2011. “Work Zone Road User Costs - Concepts and Applications”. Work Zone and Traffic Analysis Technical Resources (Report No. FHWA-HOP-12-005).

Federal Highway Agency. FHWA 2015. Pavement Comparative Analysis Technical Report.

Fernandez, I., & Berrocal, C. G. 2019. "Mechanical properties of 30 year-old naturally corroded steel reinforcing bars." International Journal of Concrete Structures and Materials, 13(1), 1-19. https://doi.org/10.1186/s40069-018-0308-x

Fu, G., & Kodikara, J. 2022. “Physical Model–Based Failure Prediction of Concrete Stormwater Pipes Subjected to Rebar Corrosion.” Journal of Pipeline Systems Engineering and Practice, 13(4). https://doi.org/10.1061/(ASCE)PS.1949-1204.0000685

Halfawy, M. R., Dridi, L., & Baker, S. 2008. "Integrated decision support system for optimal renewal planning of sewer networks." Journal of Computing in Civil Engineering. 22(6): 360. https://doi.org/10.1061/(ASCE)0887-3801(2008)22:6(360)

Heger, F. J. 1962. A theory for the structural behavior of reinforced concrete pipe. Doctoral dissertation, Massachusetts Institute of Technology.

Heger, F. J., & McGrath, T. J. 1982. Shear Strength of Pipe, Box Sections, and Other One-Way Flexural Members. In Journal Proceedings 79(6):470-483. 10.14359/10921

Hingorani, R., Pérez, F., Sánchez-Montero, J., Fullea, J., Andrade Perdrix, C., & Tanner, P. 2013. "Loss of ductility and strength of reinforcing steel due to pitting corrosion." 8th International Conference on Fracture Mechanics of Concrete and Concrete Structures. http://hdl.handle.net/10261/240459

Hojat Jalali, H., and M. Ebrahimi. 2021. “Residual life and reliabilityassessment of underground RC sanitary sewer pipelines under uncertainty.” https://digitalcommons.lsu.edu/transet_pubs/126.

Holicky, M. 2009. Reliability analysis for structural design. Stellenbosch, South Africa: SUN MeDIA Stellenbosch

Imperatore, S., Rinaldi, Z., & Drago, C. 2017. "Degradation relationships for the mechanical properties of corroded steel rebars." Construction and Building Materials, 148: 219-230. https://doi.org/10.1016/j.conbuildmat.2017.04.209

Inanloo.B, Tansel.B,l Shams.K, Jin.X, Gan.A 2016. "A decision aid GIS-based risk assessment and vulnerability analysis approach for transportation and pipeline networks". Safety Science. 84: 57-66. https://doi.org/10.1016/j.ssci.2015.11.018.

Infrastructure Technical Report ASCE. 2017.Demand on treatment plants will grow more than 23% by 2032. Reston, VA: ASCE.

Infrastructure Technical Report ASCE. 2019.Demand on treatment plants will grow more than 23% by 2032. Reston, VA: ASCE.

Ishizaka, A., & Labib, A. 2009. "Analytic hierarchy process and expert choice: Benefits and limitations." OR insight, 22(4), 201-220. doi: 10.1057/ori.2009.10

Jiang, J. H., & Yuan, Y. S. 2013. "Development and prediction strategy of steel corrosion rate in concrete under natural climate." Construction and Building Materials, 44: 287-292. https://doi.org/10.1016/j.conbuildmat.2013.03.033

Jiang, J., & Yuan, Y. 2012. "Prediction model for the time-varying corrosion rate of rebar based on micro-environment in concrete." Construction and Building Materials,35: 625-632. https://doi.org/10.1016/j.conbuildmat.2012.04.077

Jung, Y. J., & Sinha, S. K. 2007. "Evaluation of trenchless technology methods for municipal infrastructure system." Journal of infrastructure systems, 13(2): 144-156. https://doi.org/10.1061/(ASCE)1076-0342(2007)13:2(144)

Kaur, A., & Kaur, A. 2012. "Comparison of mamdani-type and sugeno-type fuzzy inference systems for air conditioning system." International Journal of Soft Computing and Engineering, 2(2): 323-325.

Kaushal, V., & Najafi, M. 2020. "Comparative analysis of environmental and social costs of trenchless cured-in-place pipe renewal method with open-cut pipeline replacement for sanitary sewers. "Journal of Pipeline Systems Engineering and Practice, 11(4), 04020037.

Kaushal, V., Najafi, M, Serajiantehrani, R, Vacanas, Y., Danezis, C., Singh, A., & Yazdani, S. 2020. Sanitary sewer construction cost comparison between trenchless cipp renewal and open-cut replacement. In Proc., International Structural Engineering and Construction, 7(1).

Kim, J., & Kasabov, N. 1999. "HyFIS: adaptive neuro-fuzzy inference systems and their application to nonlinear dynamical systems." Neural networks, 12(9): 1301-1319. https://doi.org/10.1016/S0893-6080(99)00067-2

Kingma, D. P., & Ba, J. 2014. Adam: A method for stochastic optimization. arXiv preprint arXiv:1412.6980. https://doi.org/10.48550/arXiv.1412.6980

Knauer, Harvey, Pedersen, Soren, Reherman, Clay N., Rochat, Judith L., Thalheimer, Erich S., Lau,Michael C, Fleming, Gregg G., Ferroni, Mark, Corbisier, Christopher (2006). "FHWA Highway Construction Noise Handbook (DOT-VNTSC-FHWA-06-02)". U.S. Department of Transportation and the Federal Highway Administration.

Kothamasu, R., & Huang, S. H. 2007. "Adaptive Mamdani fuzzy model for condition-based maintenance." Fuzzy sets and Systems, 158(24): 2715-2733. https://doi.org/10.1016/j.fss.2007.07.004

Lau, I., Fu, G., Li, C. Q., De Silva, S., & Guo, Y. 2018. "Critical Crack Depth in Corrosion-Induced Concrete Cracking". ACI Structural Journal. 115(4): 1175-1184. https://doi.org/10.14359/51702261.

Li, J., & Zou, P. X. 2011. "Fuzzy AHP-based risk assessment methodology for PPP projects." Journal of Construction Engineering and Management, 137(12): 1205-1209. https://doi.org/10.1061/(ASCE)CO.1943-7862.0000362

Li, X., Khademi, F., Liu, Y., Akbari, M., Wang, C., Bond, P. L., & Jiang, G. 2019. "Evaluation of data-driven models for predicting the service life of concrete sewer pipes subjected to corrosion.". Journal of environmental management, 234: 431-439. https://doi.org/10.1016/j.jenvman.2018.12.098.

Mahmoodian, M., and A. M. Alani. 2013. "Multi-failure mode assessment of buried concrete pipes subjected to time-dependent deterioration, using system reliability analysis." J. Fail. Anal. Prev. 13 (5): 634–642. https://doi.org/10.1007/s11668-013-9727-9.

Mahmoodian, M., and A. Alani. 2014. "Modeling deterioration in concrete pipes as a stochastic gamma process for time-dependent reliability analysis." J. Pipeline Syst. Eng. Pract. 5 (1): 04013008. https://doi.org /10.1061/(ASCE)PS.1949-1204.0000145.

Mamdani, E. H., & Assilian, S. 1975. "An experiment in linguistic synthesis with a fuzzy logic controller." International journal of man-machine studies.7(1): 1-13. https://doi.org/10.1016/S0020-7373(75)80002-2

Marques, P. F., Costa, A., & Lanata, F. 2012. "Service life of RC structures: chloride induced corrosion: prescriptive versus performance-based methodologies." Materials and structures, 45, 277-296.

Marquez-Peñaranda, J. F., Sanchez-Silva, M., & Bastidas-Arteaga, E. 2022. Probabilistic Assessment of Biodeterioration Effects on Reinforced Concrete Sewers. Corrosion and Materials Degradation, 3(3): 333-348. https://doi.org/10.3390/cmd3030020.

Matthews, J. C., & Allouche, E. N. 2010. A social cost calculator for utility construction projects. North American Society for Trenchless Technology .

Matthews, J. C., Allouche, E. N., & Sterling, R. L. 2015. Social cost impact assessment of pipeline infrastructure projects. Environmental Impact Assessment Review, 50: 196-202. https://doi.org/10.1016/j.eiar.2014.10.001.

Miller & Hanson., Bowlby & Associates, Environmental Acoustics, Anderson. G, Barrett. D (2014). "Supplemental Guidance on the Application of FHWA's Traffic Noise Model (TNM) (Report No. 791)". National cooperative highway research program. DOI: 10.17226/22284.

National Weather Service. 2022. "DFW—Monthly and annual average temperatures." Accessed September 18, 2022. https://www.weather.gov/fwd/dmotemp.

Navarro-Almanza, R., Sanchez, M. A., Castro, J. R., Mendoza, O., & Licea, G. 2022. "Interpretable Mamdani neuro-fuzzy model through context awareness and linguistic adaptation." Expert Systems with Applications. 189. https://doi.org/10.1016/j.eswa.2021.116098

Nesterov, Y. 1983. A method for unconstrained convex minimization problem with the rate of convergence O (1/k^ 2). 269: 543-547.

Olsson, A., Sandberg, G., & Dahlblom, O. 2003. On Latin hypercube sampling for structural reliability analysis. Structural safety, 25(1), 47-68.. https://doi.org/10.1016/S0167-4730(02)00039-5

Ormsby, C. M. 2009. "A framework for estimating the total cost of buried municipal infrastructure renewal projects."(Masters Thesis). Mcgill University. Canada.

Parker. C. D. 1951. "Mechanics of Corrosion of Concrete Sewers by Hydrogen Sulfide." Sewage and Industrial Wastes . 23(12): 1477-1485. https://www.jstor.org/stable/25031769

Petre-Lazar, I., G. Heinfling, J. Marchand, and B. Gerard. 2000. "Application of probabilistic methods to analysis of behavior of reinforced concrete structures affected by steel corrosion." In Vol. 192 of Proc., of CANMET Conf. "Concrete Durability", 557–572. Farmington Hills, MI: American Concrete Institute. https://doi.org/10.14359/5771.

Phan, H. C., Dhar, A. S., & Sadiq, R. 2018. "Prioritizing water mains for inspection and maintenance considering system reliability and risk". Journal of Pipeline Systems Engineering and Practice, 9(3), 04018009.

PHMSA (Pipeline and Hazardous Materials Safety Administration). 2020. "Pipeline Risk Modeling Overview of Methods and Tools for Improved Implementation". 1200 NEW JERSEY AVENUE, SE WASHINGTON, DC 20590. https://www.phmsa.dot.gov/

Pomeroy, D. E. 1976. "Some effects of mound-building termites on soils inUganda." J. Soil Sci. 27 (3): 377–394. https://doi.org/10.1111/j.1365-2389.1976.tb02009.x.

Pomeroy, Richard D. 1974. "Process Design Manual for Sulfide Control in Sanitary Sewerage Systems." U.S. Environmental Protection Agency, Technology Transfer

Qian, N. 1999. "On the momentum term in gradient descent learning algorithms." Neural networks, 12(1): 145-151. https://doi.org/10.1016/S0893-6080(98)00116-6

Rajani, B., and J. Makar. 2000. “A methodology to estimate remaining service life of grey cast iron water mains.” Can. J. Civ. Eng. 27 (6): 1259–1272. https://doi.org/10.1139/l00-073.

Robles-Velasco, A., P. Cortés, J. Mu˜nuzuri, and L. Onieva. 2021. “Estimation of a logistic regression model by a genetic algorithm to predict pipe failures in sewer networks.” OR Spectrum. 43 (Jan): 759–776. https:// doi.org/10.1007/s00291-020-00614-9.

Roelfstra, P. E & Wittmann. F.H. 1986. "Fracture Toughness and Fracture Energy of Concrete: Numerical method to link strain softening with failure of concrete." 163-175. Amsterdam, Netherlands: Elsevier Science Publisher B.V

Salman, B., & Salem, O. 2012. "Risk assessment of wastewater collection lines using failure models and criticality ratings." Journal of pipeline systems engineering and practice. 3(3): 68-76. https://doi.org/10.1061/(ASCE)PS.1949-1204.0000100

Schlick, W. J. 1940. Supporting strengths of cast-iron pipe for water and gas service. Ames, IA: Iowa State College of Agriculture and MechanicArts.

Schoefs, F., Aduriz, X., Bernard, O., & Capra, B. 2009. "Comparison of additional costs for several replacement strategies of randomly ageing reinforced concrete pipes." Computer-Aided Civil and Infrastructure Engineering, 24(7): 492-508. https://doi.org/10.1111/j.1467-8667.2009.00603.x

Shahata, K., & Zayed, T. 2016. "Integrated risk-assessment framework for municipal infrastructure." Journal of Construction Engineering and Management.142(1): 04015052. https://doi.org/10.1061/(ASCE)CO.1943-7862.0001028

Shoaib, M., Shamseldin, A. Y., Melville, B. W., & Khan, M. M. 2016. "Hybrid wavelet neuro-fuzzy approach for rainfall-runoff modeling." Journal of Computing in Civil Engineering, 30(1).https://doi.org/10.1061/(ASCE)CP.1943-5487.0000457

Siddique, N. 2013. Intelligent control: a hybrid approach based on fuzzy logic, neural networks and genetic algorithms.

Song, Y., Wightman, E., Tian, Y., Jack, K., Li, X., Zhong, H., ... & Jiang, G. 2019. "Corrosion of reinforcing steel in concrete sewers." Science of the Total Environment, 649, 739-748. https://doi.org/10.1016/j.scitotenv.2018.08.362

Stewart, M. G., & Al-Harthy, A. 2008. "Pitting corrosion and structural reliability of corroding RC structures: Experimental data and probabilistic analysis." Reliability engineering & system safety. 93(3): 373-382. https://doi.org/10.1016/j.ress.2006.12.013

Stewart, M. G., & Suo, Q. 2009. "Extent of spatially variable corrosion damage as an indicator of strength and time-dependent reliability of RC beams." Engineering Structures. 31(1):198-207. https://doi.org/10.1016/j.engstruct.2008.08.011

Sugeno, M. 1985. Industrial applications of fuzzy control. Elsevier Science Inc.

Sulikowski, J., and J. Kozubal. 2016. “The durability of a concretesewer pipeline under deterioration by sulphate and chloride corrosion.”Procedia Eng. 153 (6): 698–705. https://doi.org/10.1016/j.proeng.2016.08.229.

Tabesh, M., Roozbahani, A., Roghani, B., Faghihi, N. R., & Heydarzadeh, R. 2018. Risk assessment of factors influencing non-revenue water using Bayesian networks and fuzzy logic. Water Resources Management, 32(11): 3647-3670. https://doi.org/10.1007/s11269-018-2011-8

Tabuchi. H. 2017 “$300 Billion War Beneath the Street: Fighting to Replace America’s Water Pipes”. New York Times. November/10/2017.

Tang, Y., Y. Bao, Z. Zheng, J. Zhang, and Y. Cai. 2022. “Performance assessment of deteriorating reinforced concrete drainage culverts: A case study.” Eng. Fail. Anal. 131 (Jan): 105845. https://doi.org/10.1016 /j.engfailanal.2021.105845.

Texas Department of Transportation, TXDOT 2023. “Pavements Life Cycle Cost Analysis Guide”.

Tighe, S., Knight, M., Papoutsis, D., Rodriguez, D., and Walker, C. 2002. “User Cost Savings in Eliminating Pavement Excavations through Employing Trenchless Technologies,” Canadian Journal of Civil Engineering, 29: 751-761. https://www.proquest.com/scholarly-journals/user-cost-savings-eliminating-pavement/docview/213394742/se-2.

Tighe, S., Lee, T., McKim, R., & Haas, R. 1999. “Traffic delay cost savings associated with trenchless technology”. Journal of infrastructure systems, 5(2): 45-51. https://doi.org/10.1061/(ASCE)1076-0342(1999)5:2(45

Tran, D., Mashford, J., May, R., & Marlow, D. 2012." Development of a fuzzy risk ranking model for prioritising manhole inspection." Journal of computing in civil engineering. 26(4): 550-557. https://doi.org/10.1061/(ASCE)CP.1943-5487.0000162

Tran, H., W. Lokuge, S. Setunge, and W. Karunasena. 2022. “Network deterioration prediction for reinforced concrete pipe and box culverts using Markov model: Case study.” J. Perform. Constr. Facil. 36 (6): 04022047. https://doi.org/10.1061/(ASCE)CF.1943-5509.0001766.

Tuutti, K. 1982. "Corrosion of steel in concrete." Swedish Cement and Concrete Research Institute. Stockholm, Sweden

U.S. Department of Transportation (USDOT), Bureau of Transportation Statistics (BTS) “Transportation Economic Trends” https://data.bts.gov/stories/s/Transportation-Economic-Trends-Transportation-Cost/5h3f-jnbe (Washington, DC: 2022).

United States Environmental Protection Agency USEPA. 2000. Wastewater Technology Fact Sheet: Pipe Construction and Materials. Washington, DC: USEPA

Vanama, R. K., & Ramakrishnan, B. 2020. "Improved degradation relations for the tensile properties of naturally and artificially corroded steel rebars." Construction and Building Materials, 249, 118706. https://doi.org/10.1016/j.conbuildmat.2020.118706

Vecchio, F. J., & Collins, M. P. 1986. "The modified compression-field theory for reinforced concrete elements subjected to shear." ACI Journal proceeding, 83(2): 219-231. https://doi.org/10.14359/10416

Wang, L. X., & Mendel, J. M. 1992. "Generating fuzzy rules by learning from examples." IEEE Transactions on System, Man and Cybernetics. 22 (6): 1414–1427. doi: 10.1109/21.199466

Washington Department of Transportation. WSDOT 2012. "Advanced Training Manual. Chapter 7: Construction Noise Impact Assessment". https://www.nrc.gov/docs/ML1225/ML12250A723.pdf

Wu, M., & Wang, T.2022. "A probabilistic model framework for microbiologically induced corrosion of concrete sewers." International Conference on Regeneration and Conservation of Structures (ICRCS)

Xi, X., & Yang, S. 2017. "Time to surface cracking and crack width of reinforced concrete structures under corrosion of multiple rebars." Construction and Building Materials, 155: 114-125. https://doi.org/10.1016/j.conbuildmat.2017.08.051

Yuan, Y., Jiang, J., & Peng, T. 2010. Corrosion Process of Steel Bar in Concrete in Full Lifetime. ACI Materials Journal, 107: 563-568. https://doi.org/10.14359/51664042

Zadeh, L. A. 1968. "On fuzzy algorithms." Information and Control. 12(2): 94-102. https://doi.org/10.1016/S0019-9958(68)90211-8.

Zhang, Wenjun, Taotao Lai, and Yao Li 2022. "Risk assessment of water supply network operation based on ANP-Fuzzy comprehensive evaluation method." Journal of Pipeline Systems Engineering and Practice. 13(1). https://doi.org/10.1061/(ASCE)PS.1949-1204.0000602 04021068.

Zhao, J. Q., & Rajani, B. 2002. Construction and rehabilitation costs for buried pipe with a focus on trenchless technologies. Ottawa: NRC, Institute for Research in Construction.

Zhao, Y., H. Ren, H. Dai, and W. Jin. 2011a. "Composition and expansioncoefficient of rust based on X-ray diffraction and thermal analysis."Corros. Sci. 53 (5): 1646–1658. https://doi.org/10.1016/j.corsci.2011 .01.007.

Zhao, Y., J. Yu, and W. Jin. 2011b. "Damage analysis and cracking modelof reinforced concrete structures with rebar corrosion." Corros. Sci.53 (10): 3388–3397. https://doi.org/10.1016/j.corsci.2011.06.018.

Zhao, Y., J. Dong, Y. Wu, and W. Jin. 2016. "Corrosion-induced concrete cracking model considering corrosion product-filled paste at the concrete/steel interface." Constr. Build. Mater. 116 (Jul): 273–280. https://doi.org/10.1016/j.conbuildmat.2016.04.097.

Zeng, C., & Ma, B. 2009. "Analytic Mode for Predicting the Failure risk of pipeline System". In ICPTT 2009: Advances and Experiences with Pipelines and Trenchless Technology for Water, Sewer, Gas, and Oil Applications. https://doi.org/10.1061/41073(361)2